Theses and Dissertations

2012

Nanoparticles for Nonaqueous-phase liquids (NAPLs) Remediation

Pijit Jiemvarangkul
Lehigh University

Follow this and additional works at: http://preserve.lehigh.edu/etd

Nanoparticles for Nonaqueous-phase liquids (NAPLs) Remediation

By

Pijit Jiemvarangkul

A Dissertation

Presented to the Graduate and Research Committee

Of Lehigh University

In Candidacy for the Degree of

Doctor of Philosophy

in

Environmental Engineering

Lehigh University

January 2012

Certificate of Approval

Approved and recommended for acceptance as a dissertation in partial fulfillment of the requirements for the degree of Doctor of Philosophy

_____
Date

_____
Dr. Derick G. Brown
Dissertation Supervisor
And Committee Chair

_____
Dr. Wei-xian Zhang
Dissertation Supervisor

_____
Accepted Date

Committee Members:

_____
Dr. Jaavad Tavakoli
Committee Member

_____
Dr. Arup SenGupta
Committee Member

_____
Dr. Kristen Jellison
Committee Member

Acknowledgements

First of all, I would like to extend special thanks to my research advisor, Dr. Wei-xian Zhang, for all of his support, time, guidance and understanding throughout my doctorate study at Lehigh University. I have been very fortunate to have him as my advisor. Thank you very much for what you have done for me.

I would like to extend my thanks to members of my dissertation committee: Dr. Derick G. Brown, Dr. Arup K. SenGupta, Dr. Jaavad Tavakoli, and Dr. Kristen Jellison for their time and valuable suggestions and questions on my research.

Best regards to my colleagues and friends Dr. Jiasheng Cao, Dr. Hsing-Lung Lien, Dr. Xiao-qui Li, Dr. Weile Yan, Dr. Sao-lin Li, Sisheng Zhang, Dr. Pisist Kumnorkaew, Surapol Padungthon, Tanyakorn Muangnapoh and Ranjan Kumar Saho. Thank you all for your assistances in experiments and friendship. Thank you to Paul Osimo from Lehigh Nanotech LLC for his information. In addition, I would like to give my special thanks to my special friends, Kamonrat Phopin and Wutigri Nimlamoon. With the help from all of you, I have been enjoying this work.

I have to give special thanks to the Royal Thai Government and King Mongkut's University of Technology North Bangkok for their supports and the scholarship to study at Lehigh University.

Finally, I would like to share this honor with my families in Thailand, especially my mother, Skawrat Jiemvarangkul, my father, Chitchai Jiemvarangkul and my two younger brothers, Vachira Jiemvarangkul and Jrakkapong Jiemvarangkul. I will always be grateful for all of your love, trust, support, and patience.

TABLE OF CONTENTS

iv

LIST OF TABLE

LIST OF FIGURE

x

xi

ABSTRACT

Nanotechnology has gained attention in various fields of science and engineering for more than decades. Many nanotechnologies using nanosorbents, nanosensors, and nanoparticles have been developed, studied, and used to solve environmental problems. This dissertation contributes to the applications of two types of nanoparticles: 1) using zero valent iron nanoparticle technology (nZVI) for treatment of groundwater contaminated by chlorinated hydrocarbons and study effect of polyelectrolyte polymers on enhancing the mobility of nZVI in porous media and 2) testing a new type of nanoparticle, nano-scale calcium peroxide (CaO_2) particles (nano-peroxide); particles have been synthesized and preliminarily tests on their chemical properties and oxidizing reactions with petroleum hydrocarbons investigated.

Trichloroethylene (TCE) is one of the high toxic, dense, non-aqueous phase liquids (DNAPLs) and it is one of the major problems of groundwater contamination. The direct reaction of nano-scale zerovalent iron (nZVI) particles and TCE liquid phase batch experiments shows that nZVI has capability to remove pure phase TCE and there is the reduction reaction occurred with reaction byproduct. Mass balance of nZVI-TCE reaction demonstrates that 7 – 9 % TCE mass was trapped in 1 g of nZVI sludge indicating that absorption occurred during the removal process confirming the absorption of TCE into nZVI sludge. The reaction and absorption abilities of nZVI are depended upon its surface areas. Increasing amount of nZVI reduces the space of batch experiment systems, so TCE removal efficiency of nZVI is decreased. These experiments show the

1

practicability of using nZVI to directly remove TCE from contaminated groundwater.

The transport of nanoscale zero-valent iron (nZVI) particles stabilized by three polyelectrolytes: polyvinyl alcohol-co-vinyl acetate-co-itaconic acid (PV3A), poly(acrylic acid) (PAA) and soy proteins were examined. The study shows the increase in nZVI mobility by reducing particle size and generating negatively charged surfaces of nZVI by those polyelectrolyte polymers. PV3A stabilized nZVI has the best transport performance among the three materials. It was found that approximately 100% of nZVI flowed through the column. Retardation of nZVI is observed in all tests. Due to the large surface area of nZVI, large amounts of polyelectrolytes are often needed. For example, soy proteins exhibited an excellent stabilization capability only at the dose over 30% of nZVI mass. Approximately 57% of nZVI remained in the column when nZVI was stabilized with PAA at the dosage of 50%. Results suggest that nZVI may be prepared with tunable travel distance to form an iron reactive zone for the in situ remediation.

The new nano size particles of calcium peroxide (nano-peroxide) were synthesized by the mechanical milling method. The particle size diameter (d_{50}) is around 120 nm with the enormous specific surface area at 30 m^2/g. The dissolution and reaction rate of nano-peroxide is faster than typical micro powder calcium peroxide around 1.5 times. With metal catalyzes (Fe^{2+}), nano-peroxide promoted modified Fenton's chemistry (MF) and showed an excellent performance for oxidizing hydrocarbon. Benzene solutions were completely oxidized as high as 800 mg/L of benzene and gasoline contaminated solution was significantly decreased within 24 hours. pH is a major factor to increase the oxidizing of nano-peroxide.

2

This research also reports the synthesis method, images and composition of nano-
peroxide.

CHAPTER 1

INTRODUCTION

1.1 Introduction

Nonaqueous-phase liquids (NAPLs) refer to undissolved organic liquids in water that are present as a separate phase due to the difference in density and viscosity from water. NAPLs can migrate and spread under the flow of groundwater; they can form visible, separate oily phases (plumes) in the subsurface. The transport and fate of NAPL plume movement are governed by gravity, buoyancy, and capillary forces. In the environment, NAPLs typically compose complex mixtures of hydrocarbons such as petroleum products, aromatic hydrocarbons, chlorinated solvents etc. NAPLs are vexing problems in environmental contamination because it is often very difficult or impossible to clean up the residual NAPL trapped in subsurface. According to US EPA, 2009, there are approximately 617,000 underground storage tanks (USTs) nationwide that store petroleum or hazardous substances. Over 482,000 UST releases had been confirmed as of March, 2009. Steady cleanup work has progressed for over a decade and over 380,000 contaminated sites have been cleaned up. While much good work has been and continues to be done, there are about 101,000 UST sites remaining to be cleaned up (EPA 2009). The Department of Energy (DOE) has reported about 6.4 billion cubic meters of contaminated soil, groundwater, and other environmental media at the DOE sites with a wide variety of contaminants including radionuclide to metals and dense nonaqueous phase liquids (DNAPL) (DOE 2002). Based upon EPA and DOE information, only in US, there are a ton of NAPL contaminated sites waiting for cleaning processes.

4

In the last decade, nanotechnology has gained attention in various fields of science and engineering. Many nanotechnologies such as nanosorbents, nanosensors, and nanoparticles have been created, studied, and used to solve environmental problems. For example, Ferrihydrite, a nano-sized iron oxyhydroxide is one of several nanosorbents the most widely use for removal of metals and anionic species from metallurgical and chemical process solutions and wastewater (Jang et al. 2008, Richmond et al. 2004, Jia and Demopoulos 2005, Strongin et al. 2010, Kang et al. 2003). Nanoscale particles have been produced and widely used in many industries, especially in material science and engineering. At the nanoscale, the properties of many substances change. For example, the reduction power of zero valent iron is substantially increased when its size is reduced to nanoscale (< 100 nm) (Zhang 2003, Wang and Zhang 1997, Cheng et al. 2006). For environmental applications, nano-scale zero-valent iron particles (nZVI) have been studied since 1996. nZVI have been shown to be effective for the transformation of virtually all chlorinated hydrocarbon.

The discovery of nano-scale zerovalent iron (nZVI) enhances the ability to treat chlorinated hydrocarcon with less production of chlorinated intermediates and by products. The reduction power of nZVI is substantially increased when its size is reduced to nanoscale (< 100 nm) (Zhang 2003, Wang and Zhang 1997, Cheng et al. 2006). Numerous studies have found that nZVI can effectively degrade chlorinated solvents, organochlorine pesticides, PCBs, organic dyes, and inorganic pollutants such as perchlorate, nitrate, and heavy metal ions (Elliott et al. 2009, Xiong et al. 2007, Lien and Zhang 2007, Song and Carraway 2005, Kanel et al. 2005, Ponder et al. 2000, Li and Zhang 2006, Lowry and Johnson 2004, Su and Puls 2004). Several field tests have also conducted the promising prospects for in

5

situ remediation (Elliott and Zhang 2001, Glazier et al. 2003). For more than a decade, ZVI and nZVI have been used to treat chloinated hydrocarbon contaminated groundwater plumes from several source areas. While many remediation techniques such as permeable reactive barriers and direct injections have focused on the treatment of contaminants dissolved in groundwater, but no research has tried to directly remove DNAPL pure phase contaminated sources. By this point, directly removing pure DNAPL contaminated sources may speed up the contaminated site remediation processes.

Because of the relatively high ionic strength of groundwater favorable for colloidal aggregation and the high density of iron, bare nZVI without proper surface modification has very limited mobility in the subsurface. Laboratory studies have shown that nZVI typically exists as micron sized aggregates in water (Sun et al. 2006, Sun et al. 2007, Phenrat et al. 2007). To create and maintain stable suspension of nZVI particles, a common strategy is to increase the repulsive electrostatic forces. Several studies have reported that the certain polymeric materials are able to stabilize nZVI in water. A wide array of polymers has been investigated including poly acrylic acid (PAA), polyvinyl alcohol-co-vinyl acetate-co-itaconic acid (PV3A), polyaspartate (PAP), Tween 20 and biopolymers such as soy proteins, starch, and carboxymethyl cellulose (CMC) (Schrick et al. 2004, He and Zhao 2005, Phenrat et al. 2008, Tiraferri et al. 2008, Kim et al. 2009, Saleh et al. 2007, Saleh et al. 2008). Among them, PAA is the first polymer used to disperse nZVI for the field remediation while CMC has recently been tested in the field (He et al. 2010). However, the effect of polymer modified surface nZVI particles is still needed to be researched.

6

While nZVI has been extensively investigated and applied to reduce several contaminants for more than a decade, there is no report on nano-scale particles that enhance the oxidation. More recently, calcium peroxide (CaO_2) has been used as an excellent oxidant and a reliable oxygen release material (Northup and Cassidy 2007, Ndjou'ou and Cassidy 2006). This chemical has potential possibility to be produced in nano size. At the nanoscale, the oxidizing power is expected to be much higher. Therefore, nanoscale calcium peroxide may be useful in the treatment of hydrocarbon pollutants that can be degraded by chemical oxidation. Because of their excellent properties, nanoparticles are considered to be potential agents for NAPL remediation.

1.2 Objectives of this research

The overall goal of this research is to study the reaction of nanoparticles to remediate pure phase organic liquids, often termed Nonaqueous Phase Liquid (NAPL), in environmental engineering literature. Common NAPLs include gasoline, jet fuels, diesel, heating oil, and various organic solvents (e.g., TCE). Specific research objectives include:

1. To investigate the feasibility of nano-scale zero valent iron particles (nZVI) for direct elimination of nonaqueous-phase liquids (NAPLs) such as TCE.

2. Understanding the mechanisms of nZVI reactions with pure phase TCE (DNAPLs) to improve the TCE remediation by nZVI particles.

3. Examining the effects of polyelectrolyte polymers such as PV3A and PAA on dispersion and mobility of nZVI through porous media.

4. Preliminary characterization and study the chemical properties of the new type of nano-scale particles of calcium peroxide (CaO_2) or nano-peroxide.

7

5. Preliminary tests on the ability of nano-peroxide to oxidize the petroleum contaminated solution from benzene and gasoline.

1.3 Dissertation Overview

Four chapters (chapter 2, 4 to 6) are presented in the format of journal publication. Chapter 5 has been published. Chapter 2 reports the review of nano-scale zero valent iron particles and chapter 3 serves as the experimental procedure introduction. The final chapter, Chapter 7, is a summary of all the information and insights gained from the previous chapters. The brief outlines of each chapter (except for chapter 1) are presented as follows:

- Chapter 2 is a review of nZVI technology, especially focused on chlorinated hydrocarbon contaminated groundwater remediation and other current engineering aspects.

- Chapter 3 presents the experimental instruments, materials, analytical and synthetic methods.

- Chapter 4 is the study of feasibility and mechanisms of nZVI directly reacting with pure phase trichloroethylene (TCE).

- Chapter 5 presents the effect of polyelectrolyte polymers such as PV3A and PAA to improve the dispersion of nZVI and enhance the mobility of nZVI through porous media.

- Chapter 6 shows the new type of nano-scale particles of calcium peroxide including characterization of nano calcium peroxide (nano-peroxide). Moreover, the oxidization of petroleum contaminated solution such as benzene and gasoline by nano-peroxide is examined.

8

- Chapter 7 summarizes the entire research project and outlines major conclusions.

CHAPTER 2

Iron Nanoparticles for Chlorinated Hydrocarbon Contaminated Groundwater: A Review

---

2.0 Abstract

Iron nanoparticle technology is perhaps one of the first generation nanoscale environmental technologies. Over the last decade, many laboratory studies have shown the ability of iron nanoparticles in transformation of a wide variety of common environmental contaminants such as chlorinated organic solvents, organochlorine pesticides, PCBs, and various metal ions. Various synthetic and modified methods have been developed to produce high reactive iron nanoparticles. Due to its high reductive power (electron donor) and easy to be directly injected to contaminated sources, iron nanoparticles are the new effective way for groundwater remediation. This chapter provides an in-depth report on the synthesis and characterizations of iron nanoparticles. The degradation of chlorinated aliphatic compounds in groundwater or subsurface environment by iron nanoparticles is included. Other topics such as cost, mobility, and impact of iron nanoparticles are also addressed.

2.1 Introduction

Nanotechnology is the engineering and art of manipulating matter at the nanoscale ($<10^{-7}$ m). For environmental applications, nanotechnology offers the potential of novel materials, processes and devices with potentially unique activity toward targeted contaminants and desired application flexibility. Many nano-based environmental technologies (e.g., sensors, sorbents, and reactants) are under active research and development, and are expected to emerge soon as the next generation environmental technologies, with the potential to improve or replace various conventional environmental technologies in the near future.

Many nanotechnologies such as nanosorbents, nanosensors, and nanoparticles have been created, studied, and used to solve environmental problems. For example, Ferrihydrite, a nano-sized iron oxyhydroxide is one of several nanosorbents most widely used for the removal of metals and anionic species from metallurgical and chemical process solutions and wastewater (Strongin et al. 2010). Ferrihydrite nonosorbent can also be used to remove arsenic (Jang et al. 2008, Richmond et al. 2004, Jia and Demopoulos 2005) and phosphorous containing anions (Kang et al. 2003) owing to its high sorption capacity combined with very large surface area.

A hybrid ion exchanger or polymer-supported hydrated metal oxide nanoparticles is a new class of nanotechnology for environment that merges the ion exchange technology with nanotechnology. A hybrid ion exchanger is mainly an ion exchanger as functionalized polymeric host that contains metal or metal oxide nanoparticles inside its polymer phase. These hybrid nanosorbents integrate the advantageous properties of several heavy metal removal technologies (Cumbal and Sengupta 2005, Pan et al. 2010). While conventional ion exchange offers excellent

11

hydraulic properties, but poorly in the contaminant selectivity, especially in the presence of competing ion; conversely, metal oxides such as ferrihydrite offer excellent heavy metal, but perform poorly in terms of hydraulic properties and mechanical strength. By combining metal oxide nanoparticles and ion exchange, excellent hydraulic properties and heavy metal selectivity can be effectively integrated.

While the development of nanotechnology for environmental applications is growing, the studies on their fundamental are still needed to be investigated. The first generation of nanoscale materials such as nanoparticles is remained to be examined for their properties, structures, etc. For environmental treatment or remidiation research, nanoscale iron particles are considered to be top of interest for their potential as a remedial reagent for a wide variety of common environmental contaminants for more than a decade. Iron nanoparticles have small sizes for in situ injection and dispersion, large surface areas and high surface reactivity for contaminant transformation.

Iron is the fourth (~5.1%) most abundant element in the earth's crust. The core of the earth is thought to be predominantly in an iron nickel alloy from its known density. Iron exists universally in the combined state as oxides and carbonates (e.g., magnetite, hematite, limonite, and siderite). Pure iron is very much a laboratory and man-made material. Chemically pure iron can be produced by hydrogen reduction of iron oxides or hydroxides. The iron oxide is typically prepared by thermal decomposition of a ferrous complex such as oxalate, carbonate or nitrate. For example, in one method precipitated iron (III) hydroxide is heated in a stream of pure hydrogen while the temperature is raised to and maintained at 700°C until the reduction is complete. The iron obtained by

12

hydrogen reduction of oxides at relatively low temperature (360-530°C) is typically in powdered form.

Iron nanoparticle technology represents perhaps one of the first generation nanoscale environmental technologies. Over the last few years, various synthetic methods have been developed to produce iron nanoparticles, modify the nanoparticle surface properites, and enhance the efficiency of field delivery and reactions. Extensive laboratory studies have shown that nanoscale iron particles are effective for the transformation of a wide variety of common environmental contaminants such as chlorinated organic solvents, organochlorine pesticides, PCBs, and various metal ions. Recent field tests have further demonstrated promising prospective for in situ remediation.

Objective of this chapter is to provide an in-depth report on the synthesis and characterizations of iron nanoparticles. The degradation of chlorinated aliphatic compounds in groundwater or subsurface environment by iron nanoparticles is included. Other topics such as cost, fate and transport, and toxicity of iron nanoparticles are also addressed.

2.2 Iron nanoparticles for groundwater remediation

Zero-valent iron (ZVI) has been increasingly used as a groundwater remediation agent since early 2000s in the permeable reactive barrier (PRBs) systems (Gu et al. 1999, Reynolds et al. 1990). In 1996, iron nanoparticles (nZVI) with sizes less than 100 nm diameter were synthesized at Lehigh University (Wang and Zhang 1997). nZVI have much higher specific surface areas (35 m^2/g) than the conventional granular iron or microiron particles, which have specific surface areas less than 1 m^2/g (Wang and Zhang 1997). nZVI particle synthesis using the

13

borohydride (BH_4^-) reaction has been used in many laboratories (Sun et al. 2006, Masciangioli and Zhang 2003, Wang and Zhang 1997). It is also feasible to produce ultrafine iron particles using mechanical attrition. Recent laboratory research has largely focused on the degradation of common environmental contaminants including chlorinated organic compounds, organochlorine pesticide, polychlorinated biphenyles (PCBs), and organic dyes by nZVI.

2.2.1   Iron Nanoparticle Synthesis

There are two general approaches to prepare iron nanoparticles: top-down and bottom-up. The top down approach involves mechanical attrition of much larger iron particles, and has been widely used in the production of fine (e.g., micro and millimeter) metal particles and colloidal particles of numerous materials (e.g., coatings, inks, paints). The bottom up approach entails chemical synthesis and growth of crystals or clusters of metals. The size can be controlled by adjusting reaction time, reactant concentrations, mixing conditions, etc. The bottom up approach has been preferred for the preparation of nanoparticles such as quantum dots.

There are several complicated methods to produce iron nanoparticles. The simplest way is the "bottom-up" reduction of ferrous or ferric ion (Fe^{2+}, Fe^{3+}) to zero-valent iron [Fe(0)] by sodium borohydride as the following reaction (Wang and Zhang 1997):

$$4Fe^{3+} + 3BH_4^- + 9H_2O \rightarrow 4Fe^0\downarrow + 3H_2BO_3^- + 12H^+ + 6H_2 \qquad (2.1)$$
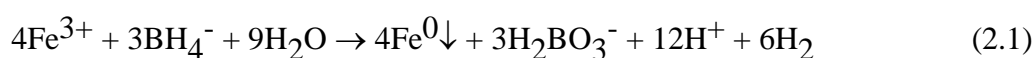
1:1 volume of $NaBH_4$ (0.2 M) and $FeCl_3.6H_2O$ (0.05 M) are mixed for 20-30 min to generate very fine iron particles. The particles are harvested with vacume filtration and washed with large volume of deionized water (>100 mL/g). Complete reduction of 0.05 mole Fe^{3+} requires only 0.0375 mole of BH_4^-. Excessive borohydride (0.2 M) is applied to accelerate the synthesis reaction and promote rapid and uniform growth of iron crystals. Synthesis at much lower concentrations of both Fe^{3+} and BH_4^- is also successfully performed. Other borohydride salts (e.g., potassium borohydride) can be used. Bulk price of potassium borohydride is actually much lower than sodium borohydride. Furthermore, ferrous iron (Fe^{2+}) can be used instead of ferric (Fe^{3+}) ion. Use of divalent iron can substantially reduce the consumption of borohydride as complete reduction of 1 mole Fe^{2+}requires only 0.5 mole of BH_4^- instead of 0.75 moles for the complete reduction of ferric ion. The beauty of the above method is that it requires no special equipment and facility and can be conducted in almost any chemical laboratory.

Moreover, iron nanoparticles can also be formed via heat treatment of iron carbonyl (e.g., $Fe(CO)_5$). For example, iron pentacarbonyl is decomposed at around 250°C to give iron as a fine powder free from most impurities. The largest use of iron pentacarbonyl is for the production of carbonyl iron powder. This is achieved by decomposition of $Fe(CO)_5$ in a cavity decomposer to give spherical iron particles of 1-10 µm. Pure iron particles can also be prepared by electrolysis of iron(II) salt (e.g., $FeCl_2$) (Elihn et al. 1999, Choi et al. 2001, Deppert et al. 2005).

The synthesized iron nanoparticles can be doped with various less reactive metals such as palladium, silver, copper etc. In general, reactive metals such as

15

iron and zinc have relatively low standard potentials (Table 2.1), and can serve as the reductants. In other words, iron can reduce the ions of Co, Ni, Pb, Cu, Ag, and Pd. The reduced metal precipitates on solid surfaces. For example, palladized Fe particles are prepared by soaking the freshly prepared nanoscale iron particles with an ethanol solution containing 1wt% of palladium acetate ($[Pd(C_2H_3O_2)_2]_3$). This caused the reduction and subsequent deposition of Pd on Fe surface (Wang and Zhang 1997):

$$Pd^{2+} + Fe^0 \rightarrow Pd^0 + Fe^{2+} \tag{2.2}$$

There are two important implications for the bimetallic particles: (1) many bimetallic particles have been shown with enhanced reactivity towards various contaminants (Zhang et al. 1998, Grittini et al. 1995, Korte et al. 1995, Muftikian et al. 1995). In other words, the surface metals may serve as catalysts for contaminant transformation; (2) the iron particles could be used to reduce and remove metal ions in water. For example, if iron nanoparticles are introduced to an aquifer contaminated with Ni(II), Ni(II) can be instatanously reduced and precipitated on the iron nanoparticles. Furthermore, bimetallic nanoparticles can form in situ if the groundwater contains heavy metals. The iron nanoparticles thus have the potential for rapid immobilization of various heavy metals in soil and groundwater.

Table 2.1. Standard electrode potentials at 25°C.

	E^0 (volts)
$Al^{3+} + 3\ e^- \Leftrightarrow Al$	-1.68
$Zn^{2+} + 2\ e^- \Leftrightarrow Zn$	-0.76
$Fe^{2+} + 2\ e^- \Leftrightarrow Fe$	-0.41
$Co^{2+} + 2\ e^- \Leftrightarrow Co$	-0.28
$Ni^{2+} + 2\ e^- \Leftrightarrow Ni$	-0.24
$Pb^{2+} + 2\ e^- \Leftrightarrow Pb$	-0.13
$Cu^{2+} + 2\ e^- \Leftrightarrow Cu$	0.34
$Ag^{+} + \ e^- \Leftrightarrow Ag$	0.80
$Pd^{2+} + 2\ e^- \Leftrightarrow Pd$	0.987

Moreover, to enhance the dispersion of iron nanoparticles, many polymers such as poly(acrylic acid) (PAA), poly(methacrylic acid)-block-poly(methyl methacrylate)-block-poly(styrensulfonate), water-soluble starch (Schrick et al. 2004, He and Zhao 2005, He et al. 2010, Sun et al. 2007), and (PV3A) (Sun and Zhang 2005, Sun et al. 2007, Li et al. 2006b) have been used for stabilizing and reducing the size of the particles.

2.2.2 Costs

A main concern is the cost of nanoparticles. It is a question being asked constantly. In the early phase of our work (prior to 2000), there was no commercial supply of iron nanoparticles. Small quantities (e.g., <10 kg) were prepared in laboratory for bench- and pilot-scale tests. The cost was rather high (e.g., >$500/kg). Several vendors have since started limited production of iron nanoparticles. The price is coming down rapidly (e.g., <<$50/kg).

Even with the increased supply and reduced price, the general perception is that the nanoparticles are still too expensive for real world applications. A careful analysis suggests the contrary, that iron nanoparticles actually offer a much better economics due to its large surface area. As shown in Table 2.2, iron nanoparticles have much lower cost per unit surface area and consequently can offer much higher return in term of performance. Moreover, research has demonstrated that the iron nanoparticles have much higher surface activity per unit of surface area. For example, the surface area normalized reaction rate for TCE and DCEs dechlorination for iron nanoparticles was 1-2 orders of magnitudes higher than bulk (~10µm) iron powders. The key hurdle for the application of iron nanoparticles is perhaps not the cost, but demonstrated field performance of the technology at large scale.

Table 2.2. Comparison of unit cost between iron powder and nano iron.

	Iron Filings	Nano Iron
Diameter (d)	0.5 mm	50 nm
Surface area (SSA)	1.5 m^2/kg	15,000 m^2/kg
Cost per kg	~$0.5/kg	<$50/kg
Iron surface/dollar	3 m^2/dollar	<300 m^2/dollar

Source of information: Lehigh Nanotech LLC

2.2.3 Particle Size Measurements

Images of the nanoparticles, prepared by sodium borohydride in our laboratory, were recorded with a Philips EM 400T Transmission Electron Microscopy (TEM) operated at 100 kV. Nanoparticle samples were prepared by depositing two to three droplets of diluted Fe nanoparticle containing ethanol

18

solution onto carbon films (Ernest Fullan Inc.). Measurement of over 420 particles was conducted and a sample picture of iron nanoparticles is presented in Figure 2.1. A size distribution of 420 particles counted is shown in Figure 2.2 with mean value of particle diameter at 62.66±39.6 nm and the median size at 60.2 nm. Most particles (83%) had diameters less than 100 nm and 35% less than 50 nm. As shown in Figure 2.3, the laboratory prepared iron particles were largely spherical.
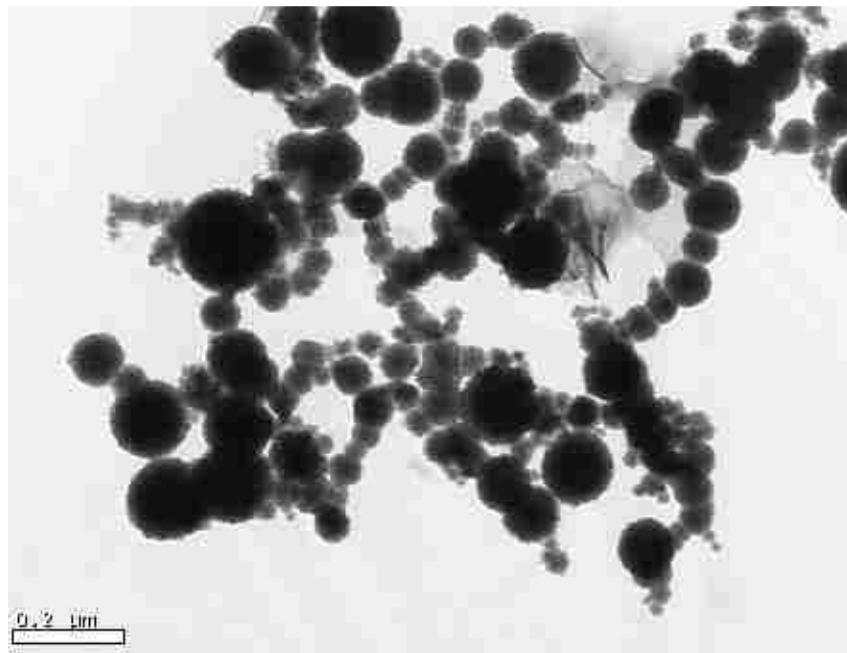
Figure 2.1. Micrographs of iron nanoparticles: (a) a single iron particles, (b) multiple iron particles.

19
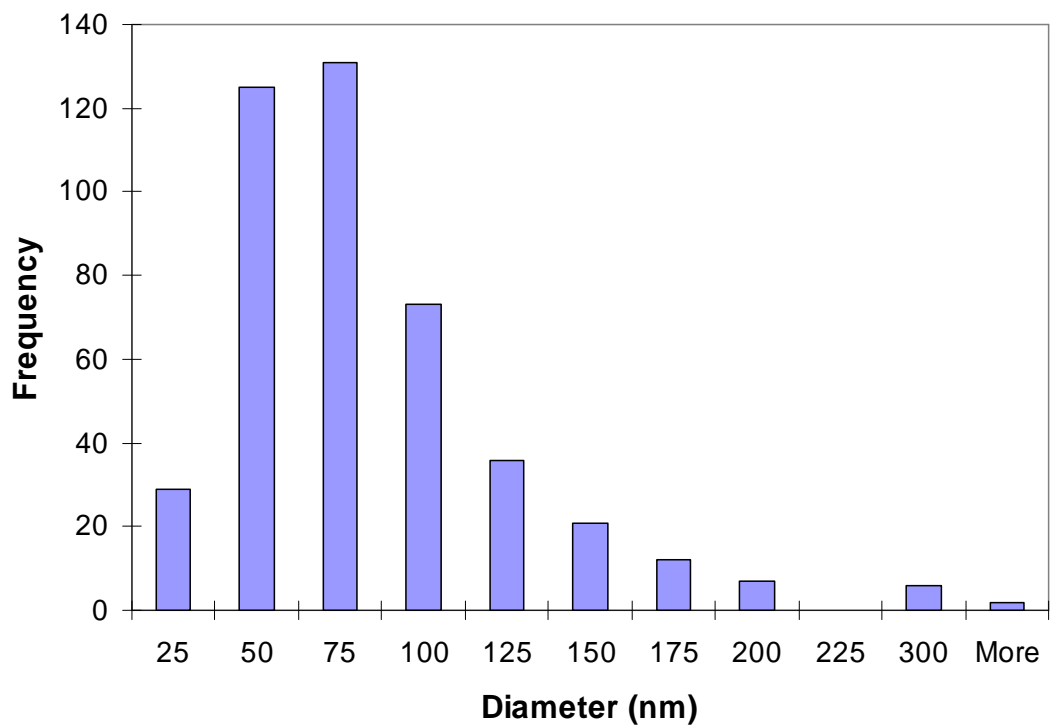
Figure 2.2. Size distribution of the iron particles. A total of 420 particles were counted.

20
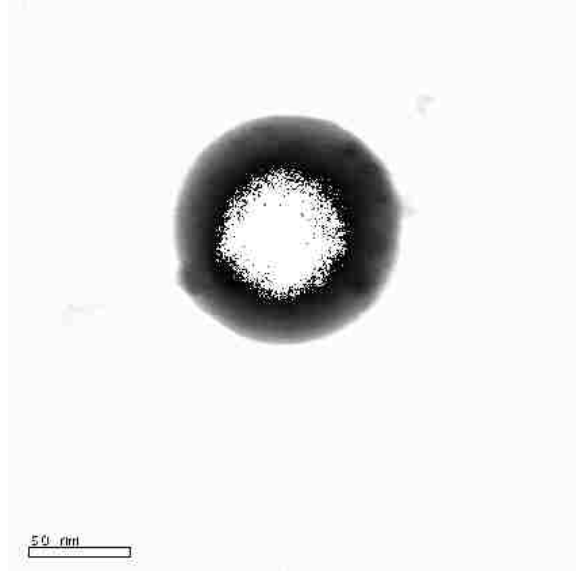
Figure 2.3. The image of single iron nanoparticle showing the spherical shape of the particle.

2.2.4 Surface area

Reactions with zero-valent iron are the net results of surface-mediated reactions. In other words, it is the surface atoms that contribute directly to the reactions. The larger the available surface area, the higher the rate of contaminant degradation (Johnson et al. 1996, Zhang et al. 1998, Lien and Zhang 1999). The reaction rates are expected to decrease with time as the surface layer is oxidized from metallic to ferrous and to ferric iron and deposited with reaction byproducts such as iron hydroxides and calcites.

Nanoparticles refer to particles generally smaller than 100 nm. An obvious effect of small particle size is the increased surface area. The smaller the particle size is, the larger the specific surface area (SSA). For a spherical particle with a diameter of d, SSA can be calculated by the following equation:

$$SSA = \frac{\text{Surface Area}}{\text{Mass}} = \frac{\pi d^2}{\rho \frac{\pi}{6} d^3} = \frac{6}{\rho d} \tag{2.3}$$

Where ρ is the density (kg/m^3) of the solid particle. For example, iron powders or filings used in permeable reactive barriers (PRBs) have diameters typically on the order of 0.5 mm and thus a theoretical SSA of approximately 1.5 m^2/kg. For iron nanoparticles of 50 nm, the corresponding SSA is ~15,000 m^2/kg. More examples of calculated and measured SSAs are given in Table 2.3.

Table 2.3. Specific surface areas (SSA) of spherical iron particles.

Diameter (d)	SSA (m^2/kg)
1 nm	763,358[1]
1 µm	763[1]
1 mm	0.763[1]
0.4 –2.0 mm[3]	1.68[2]
1 µm[4]	1,000[2]
66 nm[5]	14,500[2]

(1)   Calculated using Equation (3) with ρ at 7,860 kg/m^3 for iron.

(2)   Measured BET surface area with a Micromeritics 20/20 surface area analyzer.

(3)   Iron particles from Aldrich (10-40 mesh)

(4)   Iron particles from BASF

(5)   Particles synthesized in this work

BET (Brunauer-Emmett-Teller isotherm) is the basic method for determining the surface of particles. The basis of BET adsorption is well known in the literature and is as follows. The iron sample is contained within an evacuated sample tube cooled to cryogenic temperature. It is then exposed to nitrogen gas at a series of precisely controlled pressures. With each incremental pressure increase, the number of nitrogen molecules on the surface increases. The pressure at which adsorption equilibrium occurs is measured and the Universal Gas Law can be used to determine the quantity of gas adsorbed. As adsorption proceeds, the thickness of the adsorbed nitrogen film increases with surficial micropores being filled before macropores. The process continues until the point of bulk condensation of the nitrogen and then the reverse sequence of desorption occurs. The systematic sorption and desorption of nitrogen provides a wealth of information on the surface characteristics of the iron. The average specific surface area of iron nanoparticles is about 30 - 35 m^2/g (Zhang 2003). As a comparison, a 10-40 mesh (2 – 0.425 mm) iron filing from Aldrich was also analyzed. This Aldrich iron has a BET surface area of 1.5 m^2/kg (Cao et al. 2005a).

2.2.5 Efficiency of materials utilization

Smaller particles also mean higher efficiency of materials utilization efficiency. It is rather informative to estimate the fraction of iron atoms on the surface as a function of particle size. As illustrated in Figure 2.4, for a cube of iron particles with n atoms on each side and n^3 atoms in total, the percentage of atoms on the outer surface can be calculated:

23

$$D = \frac{\text{number of surface atoms}}{\text{total number of atoms}} = \frac{2n^2 + (n-2)[n^2 - (n-2)^2]}{n^3} \cdot 100 \quad (2.4)$$

Therefore, for a cube of 8 atoms (Fig. 2.4), all atoms sit on the surface and are exposed directly to the contaminant molecules in solution. As illustrated in Figure 2.5, D decreases rapidly with increasing particle size. As the particle grows, atom becomes surrounded by their neighbors, the dispersion (D) decreases. For nanoscale iron particles with average particle size of 50 nm, the corresponding D is ~3%. To compare, iron powders with diameters at 0.5 mm have a theoretical D of only 0.0003%.
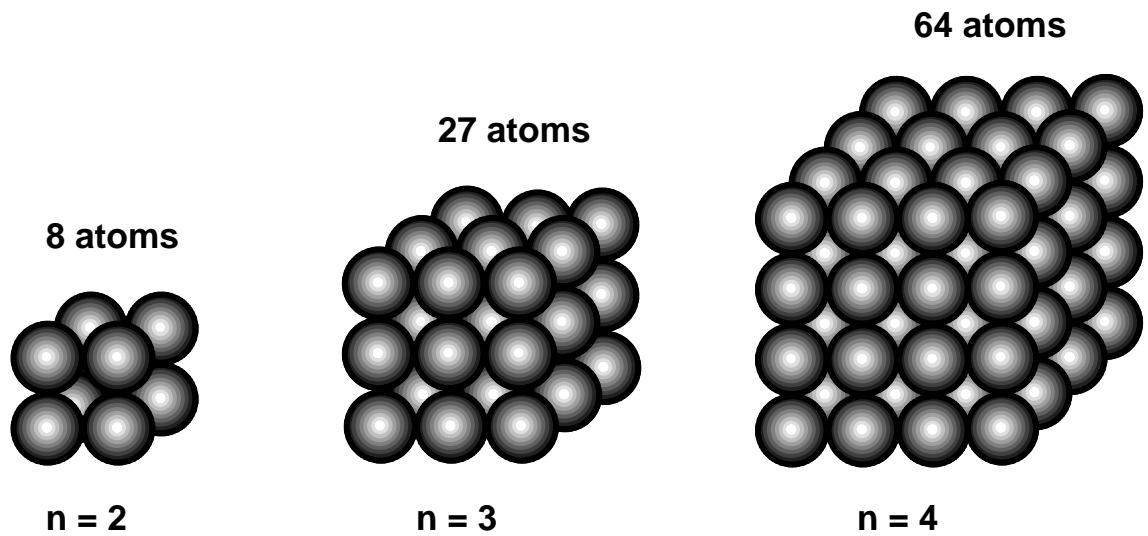
Figure 2.4. Cubes of iron atoms illustrating the number of iron atoms on the outer surface. All atoms (100%) are on the surface for a cube of 8 atoms (23). For a cube of 27 atoms (33), 26 of the atoms (96.2%) are on the outer surface. For a cube of 64 atoms (43), only 56 of the atoms (87.5%) are on the outer surface. Only a very small fraction of the atoms are on the outer surface for large (e.g., > 1 µm) particles.

24
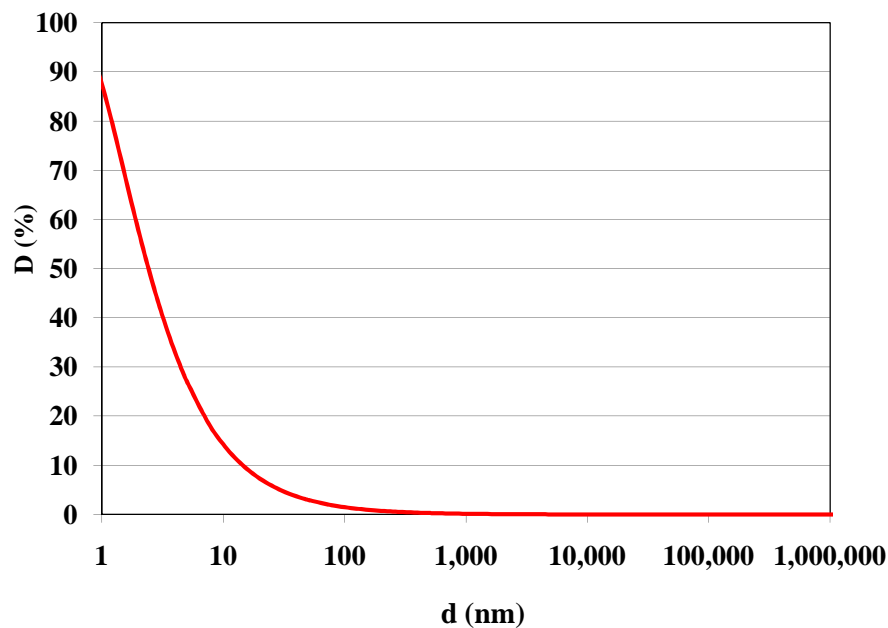
Figure 2.5. The fraction of atoms on the outer surface (D) as a function of particle size (d). D decreases rapidly with increasing particle size. An atom of iron has a diameter of approximately 0.25 nm. Four iron atoms have a total length of roughly 1 nm.

2.2.6 Water Chemistry

The oxidation of iron in the presence of oxygen and water is a common case of iron corrosion which, because of its enormous economic importance, has received much attention. For corrosion to occur at room temperature, the presence of water, an electrolyte (e.g., chloride) and oxygen is crucial. Iron completely immersed in fresh or salt water undergoes slow oxidation. Iron oxidation is more rapid if iron is only partially immersed since oxygen is rapidly replenished at the iron-water interface. The mechanism of corrosion is undoubtly electrochemical. The corrosion rate is governed by processes occurring at the water-iron interface.

25

At this junction, oxygen is reduced by a stepwise cathodic reaction which can be summarized as:

$$O_2 + 2H_2O + 4e^- \rightarrow 4OH^- \tag{2.5}$$

The four electrons required for this reaction are supplied by iron entering the solution as iron (II) cations in an anionic reaction which may be summarized:

$$2Fe \rightarrow 2Fe^{2+} + 4e^- \tag{2.6}$$

It is well known that zero-valent iron reacts with water and with naturally-occurring electron acceptors such as molecular oxygen (O_2):

$$Fe^0_{(s)} + 2H_2O_{(aq)} \rightarrow Fe^{+2}_{(aq)} + H_{2\,(g)} + 2OH^-_{(aq)} \tag{2.7}$$

$$2Fe^0_{(s)} + 4H^+_{(aq)} + O_{2(aq)} \rightarrow 2Fe^{+2}_{(aq)} + 2H_2O_{(l)} \tag{2.8}$$
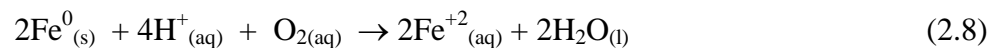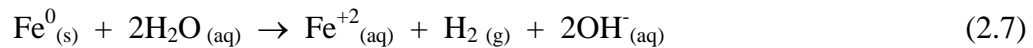
According to above reactions, iron-mediated reactions should produce a characteristic increase in pH and decline in dissolved oxygen concentration and solution standard electrode potential (E_H).

As shown in Figure 2.6, a highly reducing environment ($E_H \ll 0$) is created through the rapid consumption of oxygen and other potential oxidants and production of hydrogen. At iron nanoparticle concentration at 1.6 mg/L, the standard potential is reduced from +500 mV to below zero in ~ seconds. The highly reducing conditions are requisite for chemically-induced dechlorination. It

is also possible that at some sites, small amount of iron nanoparticles could be used to rapidly create a favorable anaerobic environment for enhanced biodegradation.
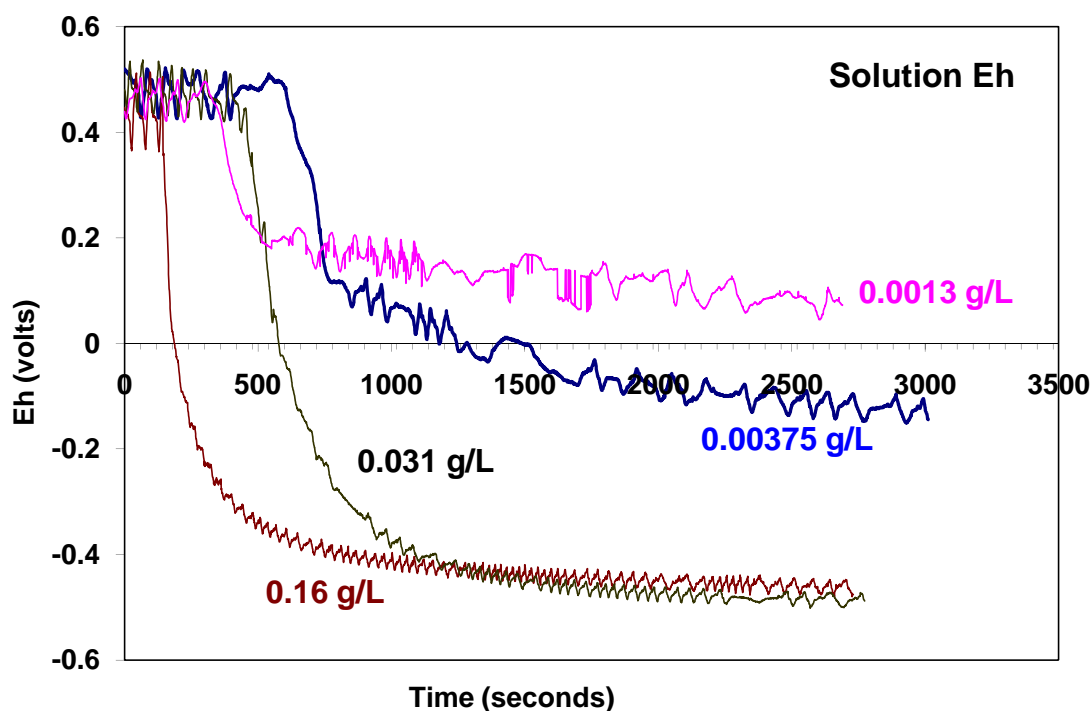
Figure 2.6. Eh as a function of reaction time and nanoparticle dosage.

2.2.7 Degradation of chlorinated aliphatic compounds

Unique physical, chemical and biological properties have been observed in various nanoparticles. Gold, for example, is a famous inert metal. However, recent research reveals that nanoparticles of gold (<10 nm) are extremely reactive, with the capacity to catalyze chemical reactions such as oxidation of carbon monoxide and hydrocarbons. It has been suggested that below 100 nanometer, the quantum forces that govern the behavior of individual atoms and molecules begin to have a discernible impact on metals and other materials, which can influence characteristics like mechanic strength, electrical conductivity, and chemical

27

reactivity. When sizes are significantly less than the wavelength of visible lights (400 - 700 nm), the particles are much less effective for light deflection and more effective for light adsorption. New phenomena of chemical, photochemical, and biological reactions could be generated. For example, our work has confirmed the complete reduction and dechlorination of perchlorate (ClO_4^-) by the nanoscale iron particles while no reaction was observed with microscale iron particles under identical experimental conditions (Cao et al. 2005b). Small particles, with large fraction of atoms on the outer surface and on the edges of the particles, and have higher surface electron density and better access by contaminant molecules in water. This can result in accelerated reactions with nanoparticles. As discussed later, reactions with the iron nanoparticles have general lower activation energy (E_a). In other words, the nanoscale particles behave like catalysts.

The chemical principles underlying the transformation of halogenated hydrocarbons by zero-valent iron have been particularly well documented. Zero-valent iron, ZVI, is an efficient electron donor in water:

$$Fe^0 \rightarrow Fe^{2+} + 2e^- \qquad\qquad E^0 = + 0.447 \text{ V} \qquad\qquad (2.9)$$
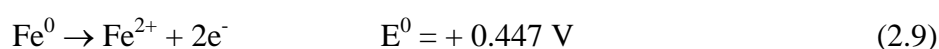
Many environmental contaminants such as polychlorinated hydrocarbon and heavy metals can serve as the electron acceptors. For example, the dechlorination of chlorinated hydrocarbon solvents such as trichloroethene and tetrachloroethene serves as a good example (Matheson and Tratnyek 1994).

$$RCl + H^+ + 2e^- \rightarrow RH + Cl^- \qquad\qquad (2.10)$$

28

From a thermodynamic perspective, the coupling of the reactions (2.9) and (2.10) is often energetically highly favorable:

$$RCl + H^+ + Fe^0 \rightarrow RH + Fe^{2+} + Cl^- \qquad\qquad (2.11)$$

For dechlorination by zero-valent iron, there are three potential transformation mechanisms proposed: (1) direct reduction at the metal surface; (2) reduction by ferrous iron at the surface; and (3) reduction by hydrogen (Matheson and Tratnyek 1994). Reduction by ferrous iron, in concert with certain ligands, is a slow process. Electron transfering from ligand-ferrous ions through the nZVI oxide shell is thought to be relatively slow and is probably not of great consequence. Dissolved hydrogen gas is not a facile reductant, and will not contribute directly to dehalogenation in the absence of a suitable catalyst (e.g., Pd). Therefore, direct reduction at the surface of metal is a major mechanism for the dechlorination of zero-valent iron. Several papers explain that the dechlorination by zero-valent iron is occurred at the surface of iron particles (Matheson and Tratnyek 1994, Zhang et al. 1998, Arnold and Roberts 2000). The core-shell structure model has been used to explain the transformation of halogenated hydrocarbons at the surface of iron particles (Li and Zhang 2006, Li et al. 2006b). However, the rate of dechlorinated reaction by zero-valent iron can be described by easy pseudo-first-order model with surface area-normalized kinetics as following equation: (Johnson et al. 1996, Zhang et al. 1998, Lien and Zhang 1999)

$$\frac{dC}{dt} = -k_{SA}a_S\rho_m C \tag{2.12}$$

Where:

C = concentration of organic compound in aqueous phase (mg/L)

k_{SA} = specific reaction rate constant (L/hm^2)

a_s = specific surface area of Fe0 (m^2/g)

ρ_m = the mass concentration of Fe (g/L of solution).

Following the reaction above (Eq. 2.11), iron nanoparticles can reduce and dechlorinate many common chlorinated aliphatic hydrocarbons. For example, TCE can be rapidly dechlorinated to ethane and CT can be reduced to mostly methane. The reduction power of nZVI is substantially increased when its size is reduced to nanoscale (< 100 nm) (Zhang 2003, Wang and Zhang 1997, Cheng et al. 2006). The dechlorination reaction rate of ZVI is depended upon the surface reaction (Matheson and Tratnyek 1994, Johnson et al. 1996). Therefore, nZVI in nano scale with huge specific surface at around 34 m^2.g^{-1} compared to less than 3 m^2.g^{-1} of micro scale ZVI (Zhang et al. 1998, Sun et al. 2006) also has very fast dechlorination reaction rate. Extensive laboratory studies have demonstrated that nZVI is a very effective material for transforming a wide array of environmental contaminants such as chlorinated organic solvents, organochlorine pesticides, polychlorinated biphenyls (PCBs), organic dyes, and various inorganic compounds (Zhang 2003, Lien and Zhang 2001, Wang and Zhang 1997, Li et al. 2006b). Figure 6 presents an example of a laboratory study on a mixture of chlorinated hydrocarbon. Six compounds mixing trans-dichloroethene (t-DCE), cis-dichloroethene (c-DCE), 1,1,1-trichloroethane (1,1,1-TCA), tetrachloroethylene (PCE), trichloroethylene (TCE), and tetrachloromethane were investigated. The

initial concentration was 10 mg/L for each of the six compounds and the total nZVI loading was 5 g/L. As illustrated in Figure 2.7 by the trend illustrated in the gas chromatograms over the reaction course, all of six compounds were reduced by the ZVI nanoparticles. Within one hour, over 99% removal of PCE was observed. Greater than 95% removal efficiency of the 6 compounds was achieved within 120 hours. So far, little has been published on the treatment of pure phase organic pollutants.

31
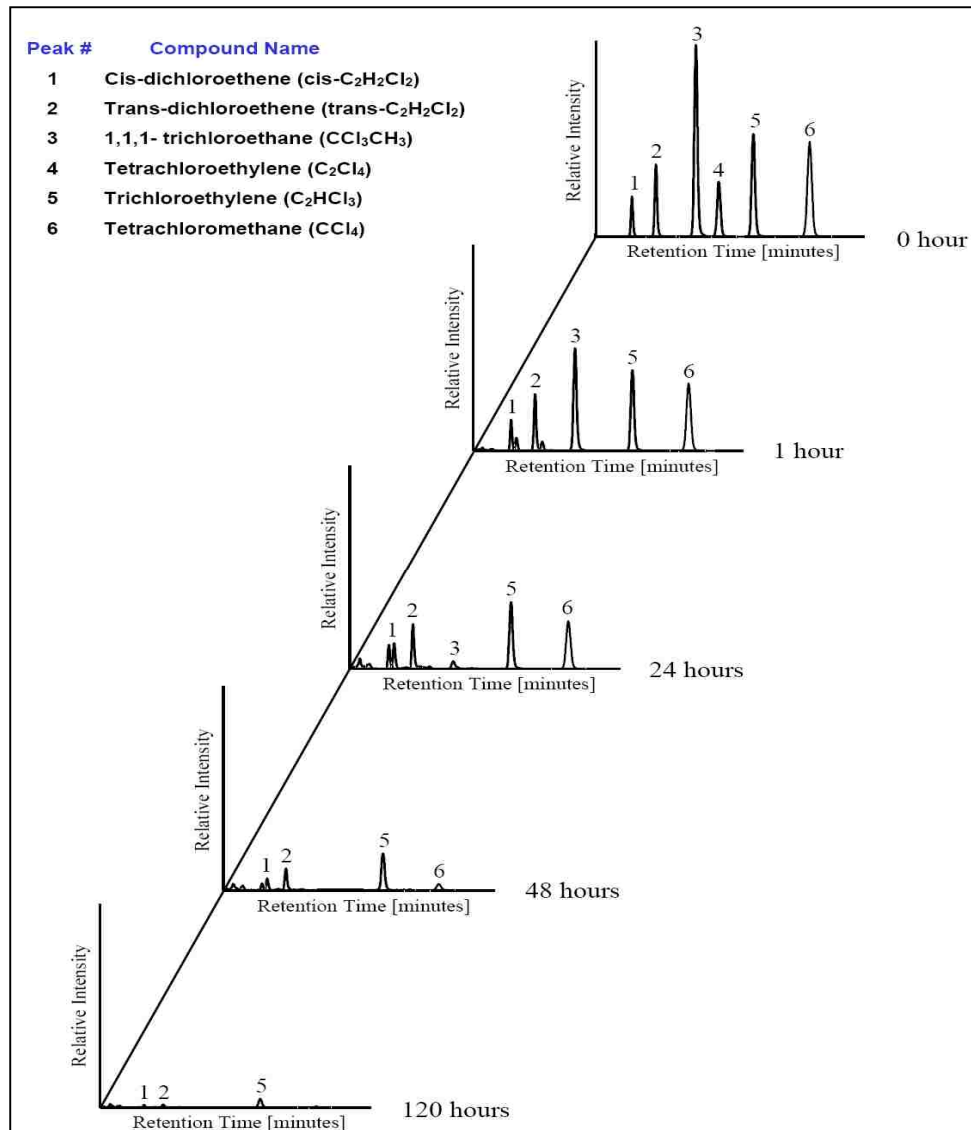
Figure 2.7. Reactions of iron nanoparticles (5g/L) with a mixture of chlorinated aliphatic hydrocarbon. Gas chromatograms are shown in this figure. Six compounds with initial concentration at 10 mg/L are presented; trans-dichloroethene (t-DCE), cis-dichloroethene (c-DCE), 1,1,1-trichloroethane (1,1,1-TCA), tetrachloroethylene (PCE), trichloroethylene (TCE), and tetrachloromethane (Zhang 2003).

2.2.8   Bimetallic iron nanoparticles

As mentioned previously, iron nanoparticles can form bonds with various less reactive metals such as palladium, silver, copper etc. Iron nanoparticles can reduce Co, Ni, Pb, Cu, Ag, Pd and the reduced metal precipitates on their surfaces. Many bimetallic particles have shown with enhanced reactivity towards various contaminants (Grittini et al. 1995, Korte et al. 1995, Muftikian et al. 1995). In other words, the surface metals may serve as catalysts for contaminant transformation. By the corporation of a noble or catalytic metal such as Pd, Ni, Pt, or Ag, iron nanoparticles can substantially enhance the overall dechlorination rate. It has been reported that the surface area normalized rate constant (K_{SA}) of Fe/Pd nanoparticles for the degradation of tetrachloromethane is more than twice orders of magnitude of microscale iron particles (Lien and Zhang 1999). The activation energy of Fe/Pd nanoparticles in the transformation of tetrachloroethylene (PCE) was calculated to be 31.1 kJ/mole compared to 44.9 kJ/mole for iron nanoparticles (Lien and Zhang 1999). The fast reaction generated by the bimetallice nanoparticles also reduces possibility of toxic byproduct formation and accumulation.

2.2.8.1 Function of secondary metallic catalyst

In principle, iron can reduce metal ions such as Co, Ni, Pb, and Cu which have higher standard potentials (E) as shown in Table 2.1. Furthermore, it is also possible to prepare bimetallic particles of Zn-Pd, Zn-Ni etc. At many sites, metal ions such Ni(II) and Cu(II) co-exists with chlorinated solvents. Bimetallic iron nanoparticles (e.g., Fe-Me) can actually form in situ. The presence of some heavy metal ions actually promotes the reduction of halogenated hydrocarbons.

33

In our laboratory, iron nanoparticles with varied palladium loadings (0-50%) were prepared and tested according to Lien and Zhang (2007) method. In all of the batch experiments, the initial concentration of TCE was 120 mg/L and the metal loading was 0.25g per 50 mL aqueous solution. Higher degradation rates of TCE by nanoscale Pd/Fe particles appeared between 1 and 5% by weight palladium. The reactivity was greater than the iron nanoparticles (with no palladium) by a factor of about 50. Little benefit was observed when the palladium content increased from 5 to 50%. Actually, the reactivity actually decreased significantly. No reaction was observed when the palladium content was approximately 50% of iron mass. If the role of palladium is purely a catalyst, a monolayer of palladium on the nano iron surface should be sufficient. If all the palladium atoms are closely packed, it requires ~9.3% wt of palladium to form a monolayer of palladium.

Surface composition of the bimetallic particles was determined by the methods of X-ray diffraction (XRD). The XRD analysis was conducted with a Philips XRD 3100 diffractometer at 45 kV and 30 mA. It used copper Kα radiation and a graphite monochromator to produce X-rays with a wavelength of 1.54060 Å. Iron nanoparticles were placed in a glass holder and scanned from 20 to 60° 2θ. This scan range covered all major species of iron, palladium, Pd/Fe alloy, and iron oxides shown in Table 2.4. The scanning rate was set at 2.0 degree/minute.

34

Table 2.4. XRD diffraction angles of characteristic peaks for iron and palladium.

Species of iron	Diffraction angle (2θ)
Iron (Fe)	44.7° (main peak), 65.0°
Iron Oxide (-Fe_2O_3)	30.5°, 35.8° (mean peak), 43.3°
Palladium (Pd)	40.1° (main peak), 46.4°, 67.8°, 81.9°, 86.5°
Palladium Oxide (PdO)	33.6°, 33.9° (main peak), 42.1°, 54.9°

An example of X-ray diffractogram of nanoscale Pd/Fe particles is shown in Figure 2.8. Apparent peaks included zero-valent iron, iron oxide (Fe_2O_3) and palladium that appeared at the 2θ of 44.9°, 35.8°, and 40.0°, respectively. This confirmed that the nanoscale Pd/Fe particles had the surface structures consisting of mainly iron and palladium.

35
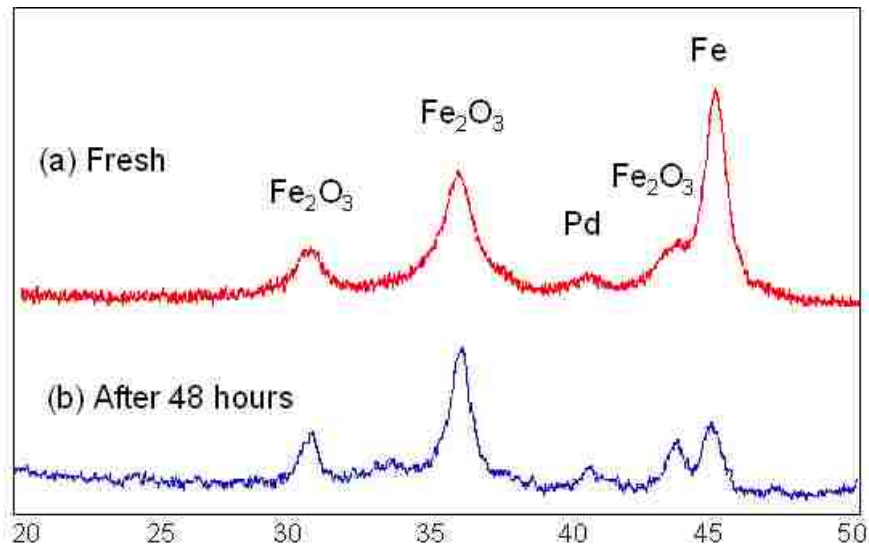
Figure 2.8. X-ray diffractogram of nanoscale Pd/Fe particles.

A total of 15 chlorinated aliphatic compounds were tested in our laboratory as listed in Table 2.5. An example is shown in Figure 2.9. Concentrations in Fig. 9 are expressed as the ratio to initial organic carbon. Immediate appearance of ethane corresponds to the disappearance of PCE. Average yield of ethane was 89 % after one hour. Trace amounts of TCE were detected briefly (< 1 hour). The amount of TCE was near the detection limit (< 10 µg/L). No other product was detected within a three-hour reaction time.

36

Table 2.5. Chlorinated aliphatic compounds tested by Fe/Pd nanoparticles.

	Compound Name	Molecular Formula	K_{SA} (L/m^2/hr)	$K_{SA}^{(1)}$ (L/m^2/hr)
1	Tetrachloroethylene (PCE)	C_2Cl_4	0.0122	2.1×10^{-3}
2	Trichloroethylene (TCE)	C_2HCl_3	0.0182	3.9×10^{-4}
3	*trans*-Dichloroethylene (*tans*-DCE)	$C_2H_2Cl_2$	0.0151	1.2×10^{-4}
4	*cis*-Dichloroethylene (cis-DCE)	$C_2H_2Cl_2$	0.0176	4.1×10^{-5}
5	1,1-Dichloroethylene (1,1-DCE)	$C_2H_2Cl_2$	0.0115	6.4×10^{-5}
6	Hexachloroethane (HCA)	C_2Cl_6	0.020	0.031
7	Pentachloroethane (PCA)	C_2HCl_5	0.026	-
8	1,1,1,2-Tetrachloroethane (1,1,1,2-TeCA)	$C_2H_2Cl_4$	0.021	0.014
9	1,1,2,2-Tetrachloroethane (1,1,2,2-TeCA)	$C_2H_2Cl_4$	0.0088	0.012
10	1,1,1-Trichloroethane (1,1,1-TCA)	$C_2H_3Cl_3$	0.0054	0.011
11	Carbon Tetrachloride (CT)	CCl_4	0.009	-
12	Chloroform (CF)	$CHCl_3$	0.0065	-
13	Bromoform (BF)	$CHBr_3$	0.079	-
14	Dibromomethane (DBM)	CH_2Br_2	0.044	-
15	Dibromochloromethane (DBCM)	$CHBr_2Cl$	0.056	-

(1) K_{SA} values for microscale iron particles (Johnson et al., 1996)
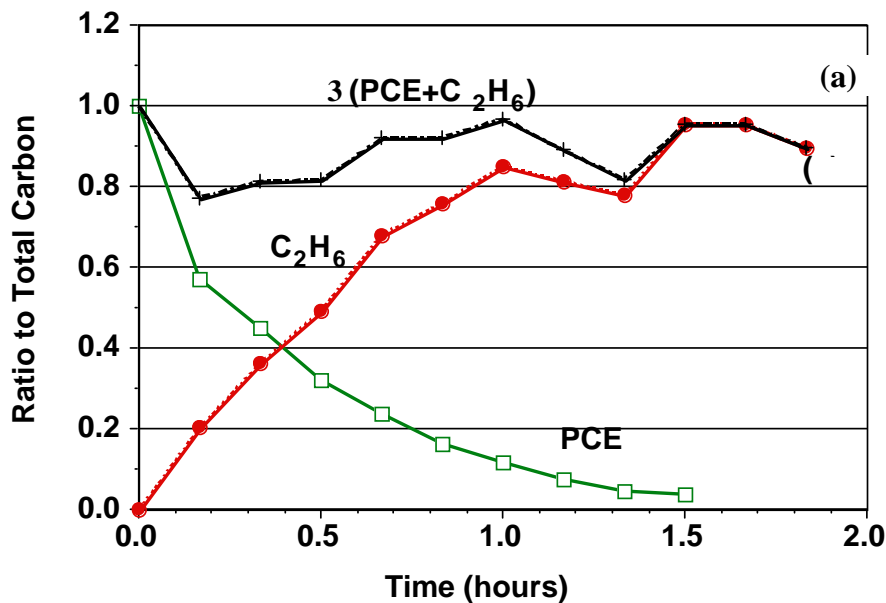
Figure 2.9. Reactions of nanoscale Pd/Fe bimetallic particles with 20 mg/L of PCE. Metal to solution ratio was 0.25g/50mL (Lien and Zhang 1999).

The rates of transformation are quantified by the surface-area normalized rate coefficient ($L/hr/m^2$). Values of K_{SA} for other compounds are given in Table 2.5. It also contains literature K_{SA} values for much larger iron particles (Johnson et al. 1996). Three key observations can be made: (1) K_{SA} values for the nanoscale metal particles were about 5.8 to 429 times higher than the commercial-grade iron particles. These results for nanoscale bimetallic iron particles are consistent with experimental observations for palladized iron (40 mesh), which were found to be more than an order of magnitude faster than zero-valent iron for the transformation of TCE (Liang et al. 1997). Several factors may contribute to this rate enhancement. Laboratory synthesized nanoscale iron surfaces may have a "fresher" metal surface due to less surface oxidation and/or surface contamination.

38

Mass transfer resistance in the batch system could also be less significant. It was observed that the Aldrich iron particles settled at the bottom of the batch bottle while a large fraction of nanoscale iron particles remained suspended in solution. Therefore slow transport or diffusion of chlorinated ethylenes to the settled Aldrich iron surfaces may have contributed to the slower reaction for the commercial-grade iron particles. (2) Differences of nanoscale metal K_{SA} values among the chlorinated ethylenes are quite small (max/min=1.50), compared to orders of magnitudes for the larger iron particles. (3) Both a_s and K_{SA} are tens to hundreds of times higher than those of commercial-grade iron particles. Taken as a whole, the overall performance of a nanoscale metal system could be potentially thousands of times better according to Eq. 2.12.

Based upon our laboratory experiments on Pd/Fe nanoparticles, the mechanism of bimetallic has been proposed (Lien and Zhang 2007). Palladium on iron surface creates indirect reduction by producing atomic hydrogen. Because of low activation barrier for H_2 dissociation on palladium surface (2 kcal/mol or less) (Masel 1996), atomic hydrogen is readily formed at the palladium surface with the low cathodic hydrogen overpotentials. A conceptual model that explains the catalytic behavior of palladium in the hydrodechlorination of chlorinated hydrocarbons is illustrated in Figure 2.10. Following Eq. 2.7, water is dissociated by zero-valent iron and produces the hydrogen evolution and is followed by the formation of atomic hydrogen at the palladium surface. Then, atomic hydrogen degrades chlorinated hydrocarbons such as PCE through a surface-mediated process (Fig. 2.10). This proposed model explains the intrinsic function of palladium and how the proton source gets involved into the overall reaction.
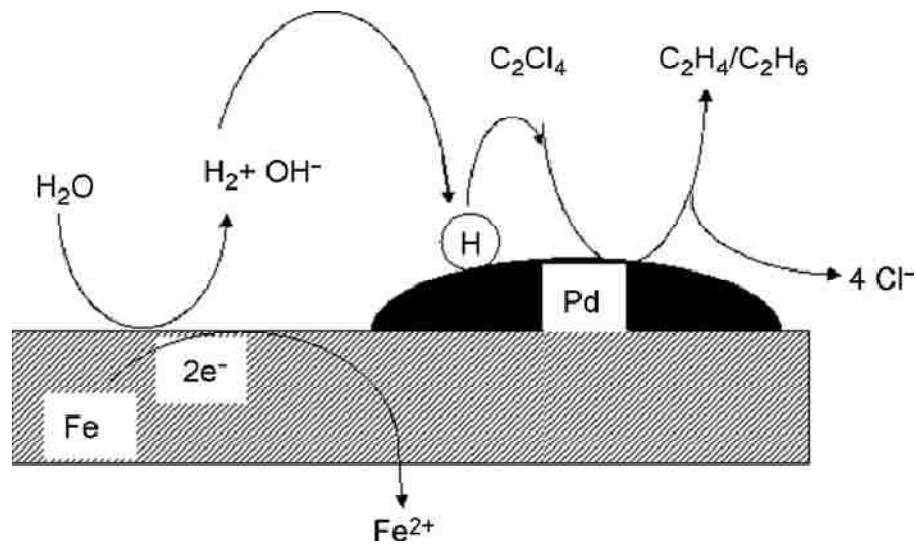
Figure 2.10. A conceptual model for the hydrodechlorination of tetrachloroethylene.

2.2.9 Effect of Temperature

All chemical and biological reactions are influenced by temperature changes. Laboratory experiments are typically conducted at room temperatures (~20°C). On the other hand, temperature in the subsurface environment is typically in the range of 10-15°C. It is thus of great importance to determine the effect of temperature on the rate and extent of dechlorination with the iron nanoparticles. Data gathered under different temperatures could further provide insights into the underlying reaction mechanisms. For example, a chemical reaction (e.g., oxidation-reduction) tends to show larger temperature dependence than a physical process (e.g., sorption). As a matter of fact, the effect of temperature on the rate of heterogeneous reaction has frequently been used as a tool to distinguish the rate-limiting step, which may involve a chemical reaction at the surface or the diffusion

40

of a reactant to the surface. Diffusion-controlled reactions in aqueous solution have relatively low activation energies (~8 to 21 kJ/mole), whereas surface-controlled reactions may have relatively larger activation energies (> 29 kJ/mole) (Brezonik 1994).

Batch experiments with the nanoscale Fe and Fe/Pd particles were conducted in temperatures ranging from 5°C to 50°C (Lien and Zhang 2007). Batch bottles were incubated in a Fisher Scientific 307 low temperature incubator. Results for PCE dechlorination are shown in Figure 2.11. It was obvious that PCE reduction increases with increasing temperature. Complete degradation of PCE took less than 45 min at 50°C and over six hours at 5°C with the nanoscale Pd/Fe particles. Experiments conducted under similar conditions showed that it took more than 100 hours to achieve similar results by the nanoscale Fe particles at 25°C (Fig. 2.11b).

41
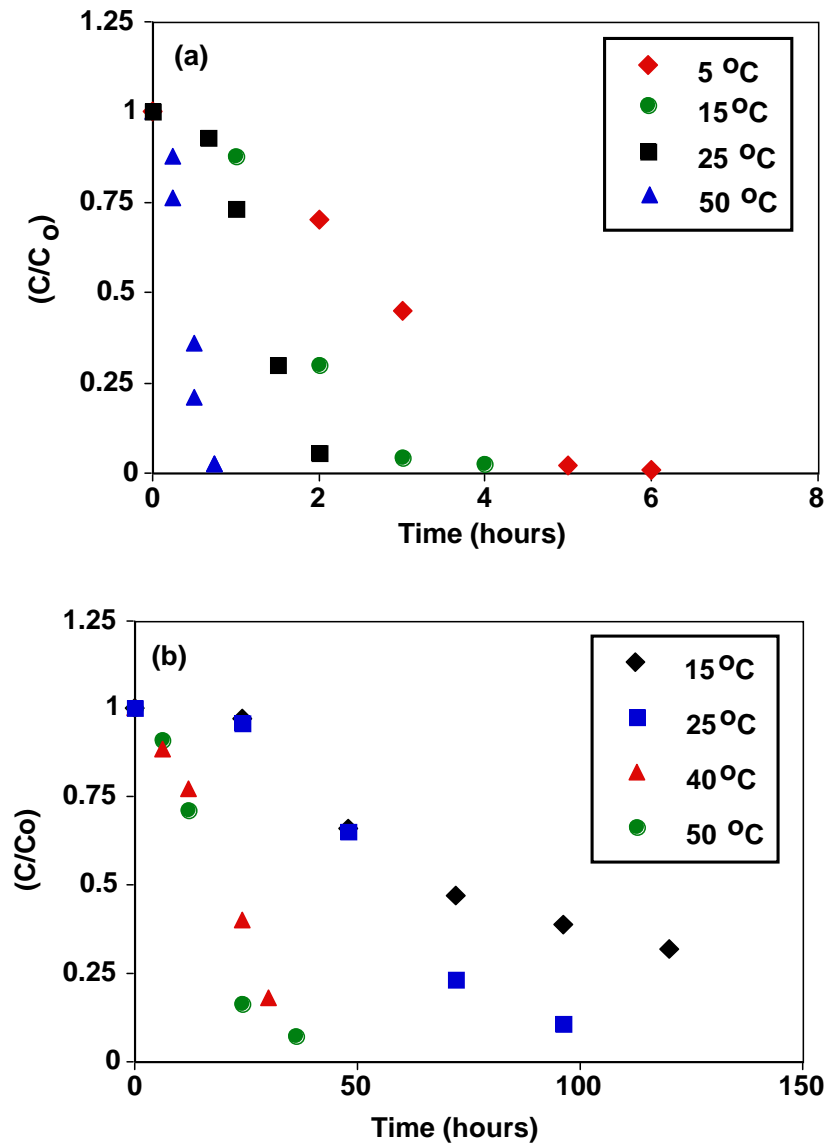
Figure 2.11. Transformation of PCE by nanoscale Pd/Fe particles and iron nanoparticles. Initial concentration of PCE was 30 mg/L. (a) nanoscale Pd/Fe particles loading was 0.25g in 150 mL and (b) iron nanoparticles loading was 1.0g/150mL.

42

Effect of temperature on reaction rate is often expressed by the classical Arrhenius equation:

$$k = A \exp(-\frac{E_a}{RT})$$ (2.13)

where k is the rate constant, A is a frequency factor, and E_a is the activation energy. Integrating the above equation yields:

$$Lnk = -E_a / RT + \ln A$$ (2.14)

A plot of Ln k versus 1/T would result in a linear relationship as shown in Figure 2.12.
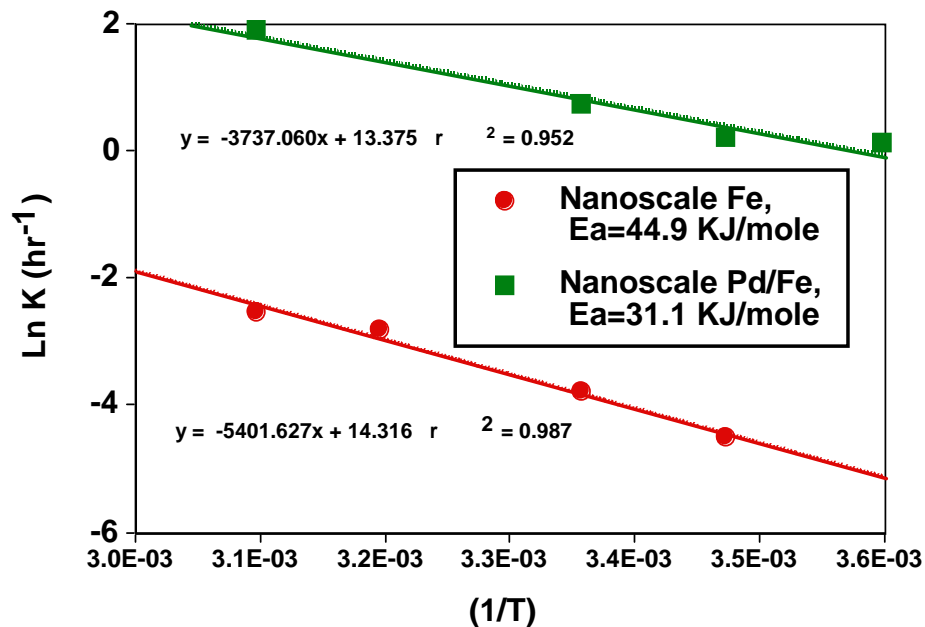
Figure 2.12. Activation energy for the transformation of PCE by nanoscale Pd/Fe and iron nanoparticles.

For the nanoscale Pd/Fe bimetallic system, the measured rate constants were 1.14, 1.23, 2.07, and 6.71 (hr^{-1}), corresponding to 5, 15, 25, and 50°C, respectively. For the nanoscale Fe system, the measured rate constants were 0.011, 0.023, 0.064, and 0.081 (hr^{-1}), corresponding to 15, 25, 40, and 50°C, respectively. The slope of the plot was assigned as a ratio of the activation energy (E_a) to the gas constant (R) in Fig. 2.12. By this method, the activation energies of dehalogenation of PCE by nanoscale Pd/Fe and Fe particles are approximately 31.1 and 44.9 kJ/mole, respectively (Lien and Zhang 2007). Using Eq. 2.14, the reaction rate for the Fe/Pd particles will be 278.47 times as that of the iron nanoparticles at the same temperature if the A is assumed to be the same for the two types of nanoparticles. Adding 1% of palladium clearly enhances the rate of dechlorination. The reduction of the activation energy for the Pd/Fe bimetallic system suggested further supports the hypothesis that palladium serves as a catalyst for the dechlorination and hydrogenation reactions.

The activation energy can be considered to be the kinetic barrier that the molecules must overcome in order to compete the dechlorination reactions. Heterogeneous reactions usually involve multiple reaction steps in the overall reaction of PCE or TCE with iron particles including the diffusion of PCE molecules onto the surface, chemical reactions occurring on the surface, and diffusion of product(s) back into the solution. The rate-limiting step, the slowest reaction step requiring the greatest activation energy, determines the overall kinetics. The activation energies obtained in this study using Pd/Fe and Fe particles are greater than 29 kJ/mole, a suggested minimum value of the activation energy for chemical-controlled reactions. This may imply that the surface-chemical reaction could be the rate-limiting step for PCE transformation. Similar

44

conclusions for the dehalogenation of TCE and CT using zero-valent iron were also suggested by Su, and Puls (1999): E_a = 32.3 – 39.4 kJ/mole for dehalogenation of TCE (Su and Puls 1999), and Scherer et al. (1997): E_a = 55.9 kJ/mole for CCl_4 and 40.5 kJ/mole for hexachloroethane (Scherer et al. 1997).

2.2.10 Mobility

An important attribute of nanoparticles is the high mobility in environmental media, especially in the subsurface environment. An iron particle in water is subjected to various forces, e.g., gravitational, electrostatic, magnetic, and random Brownian motion. For large particles (e.g., diameter > 1 µm), the gravitational force dominates and leads to rapid sedimentation of particles. For ultrafine iron particles (<100 nm), the random Brownian motion could govern. Evidence observed suggests that iron nanoparticles have strong tendency to form much larger aggregates. As discussed later in this paper, a relatively stable dispersion of iron particles can be prepared by modifying the iron surface. The surface modified iron nanoparticles can remain in suspension for extended periods. Stable dispersion of iron particles offers the possibility of uncomplicated injection, mixing and rapid transport within the slow flowing groundwater. Many of in situ injections have been reported so far (Elliott and Zhang 2001, Wei et al. 2010, He et al. 2010, Henn and Waddill 2006, Quinn et al. 2005). However, many field tests indicate that nZVI may migrate only very short distance (few feet) from the point of injection (Zhang 2003).

Aggregation and sedimentation of nZVI can be controlled by Brownian diffusion and advection. Unfortunately, the relatively high ionic strength environment of groundwater results in a colloidal aggregation and the high density

45

of bare nZVI limit their mobility in the subsurface. Based upon theories of colloidal aggregation in water, it has been generally assumed that nZVI suspension in water depends on the net effect of attractive and repulsive forces among nZVI particles. According to the DLVO theory, the overall stability of a colloidal system is determined by the sum of van der Waals attraction and electrostatic double layer repulsion (Stumm and Morgan 1996).

To create and maintain stable suspension of nZVI particles, a common strategy is to increase the repulsive electrostatic forces. Several studies have reported that the certain polymeric materials are able to stabilize nZVI in water. A wide array of polymers has been investigated including poly acrylic acid (PAA), polyvinyl alcohol-co-vinyl acetate-co-itaconic acid (PV3A) and biopolymer such as soy proteins, starch, and carboxymethyl cellulose (Schrick et al. 2004, He and Zhao 2005, He et al. 2010, Sun et al. 2007). In general, the polymers consists of polar anchoring groups (e.g., -COOH, -OH, -C=O) and a stabilizing hydrocarbon chains. The anchoring groups can chemically or physically attach onto the surface of nZVI while the stabilizing chains in water can waggle around and take up varied configurations. Overlap of these flexible chains associated with the neighboring particles produces electrostatic and steric repulsions between particles and can thus stabilize the particles under certain conditions (Everett 1989). Our previous work has demonstrated that PV3A provides great electro-steric stabilization for nZVI (Sun et al. 2007, Sun and Zhang 2005). As illustrated in Figure 2.13, in the absence of PV3A, the bare nZVI, has a particle size of about 100 nm that is apparently a loose aggregate of numerous primary ZVI nanoparticles with the size less than 10 nm (Lin et al. 2010). The bare nZVI aggregates and precipitates in a few min. With

the addition of PV3A, nZVI with the size of about 15 nm can exist in water for months (Li et al. 2006b).

In general, aquifer materials are negatively charged; thus, a negatively charged surface of particles would be favorable for particle transport. The zero-point of charge (pH_{zpc}) has been determined to be 8.1 for bare nZVI (Sun et al. 2007, Sun and Zhang 2005). In other words, the nZVI surface is negatively charged at pH greater than 8.1. At near neutral pH, bare nZVI has positive charges, which are detrimental to nZVI transport due to the rapid attachment to aquifer materials. On the other hand, both PAA and PV3A stabilized nZVI showed a relatively low value of pH_{zpc}. For example, the addition of PV3A significantly converted nZVI to a negative charge over a wide pH range. The pH_{zpc} of PV3A stabilized nZVI was measured to be about 4.7. Consequently, the polyelectrolyte stabilized nZVI possesses strong electrostatic repulsion against the attachment to aquifer materials under neutral pH conditions.
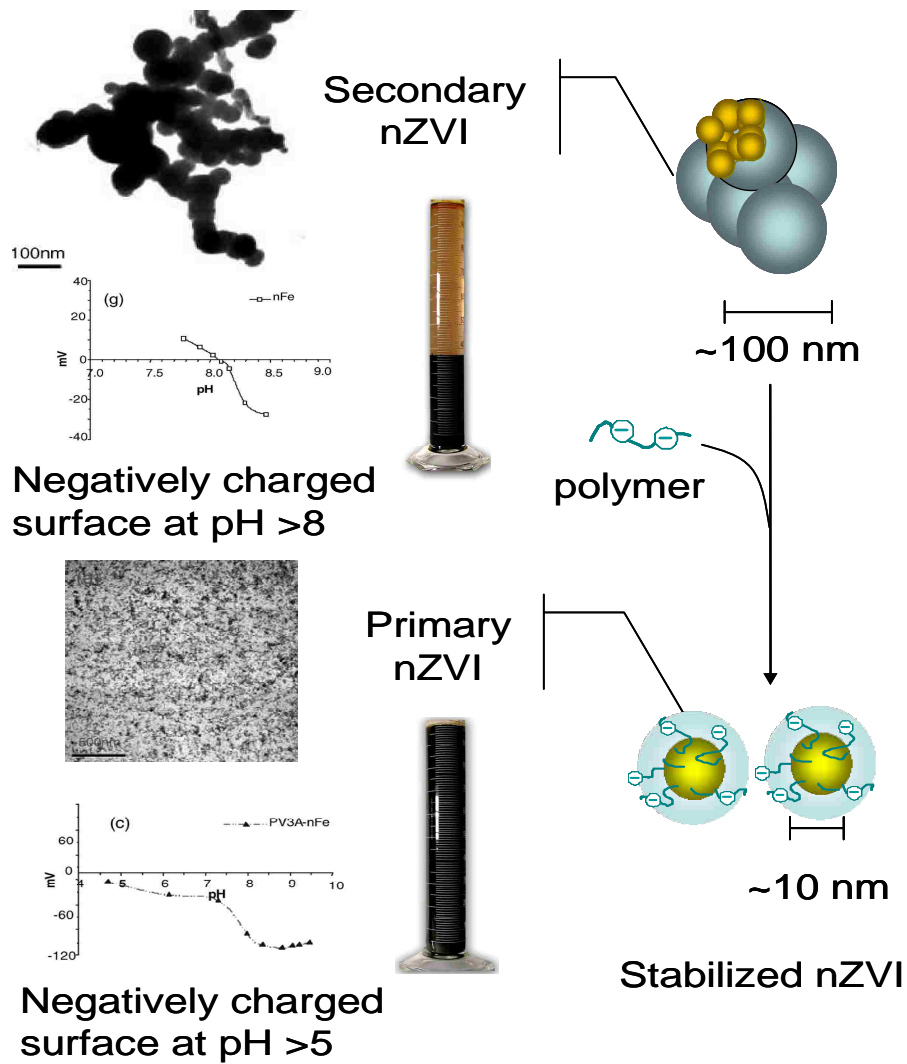
Figure 2.13. Stabilized nZVI by polymer (PV3A) reduces size and isoelectric point.

2.3 Impact of iron nanoparticles

2.3.1 Biological importance of iron

Iron plays an important role in the chemistry of living organisms being found at the active center of many biological molecules. It is an important constituent of the blood and tissues of the animal body. Most of the iron in the

body is present as iron porphyrin or heme proteins which include hemoglobin in the blood, myoglobin and the heme enzymes. For example, heme is an iron (II) complex of porphyrin, in which the iron atom has a coordination number of 6 (Figure 2.14). This configuration permits the reversible combination with molecular oxygen. It is by mechanism that the red blood cells carry oxygen from one part of the body to another. Iron also presents in other types of proteins such as transferrin, ferritin and hemosiderin. In ferritin, iron is believed to be present as iron (III) hydroxide micelles or clusters. Many enzymes require iron for activity and in some cases the iron is weakly bound, as, for example, with aconitase. Some of these enzymes are involved in the production or removal of potentially toxic chemicals, including hormones.

The intracellular concentration of free iron, iron not bound to organic ligands, is tightly controlled in animals, plants, and microbes. This is partly a result of the poor solubility of iron under aqueous and aerobic conditions: Solubility product (K_{SP}) of $Fe(OH)_3$ is $4x10^{-38}$ (Snoeyink and Jenkins 1980). Within the cell, free iron generally precipitates as polymeric hydroxides.

49

(a)   (b)
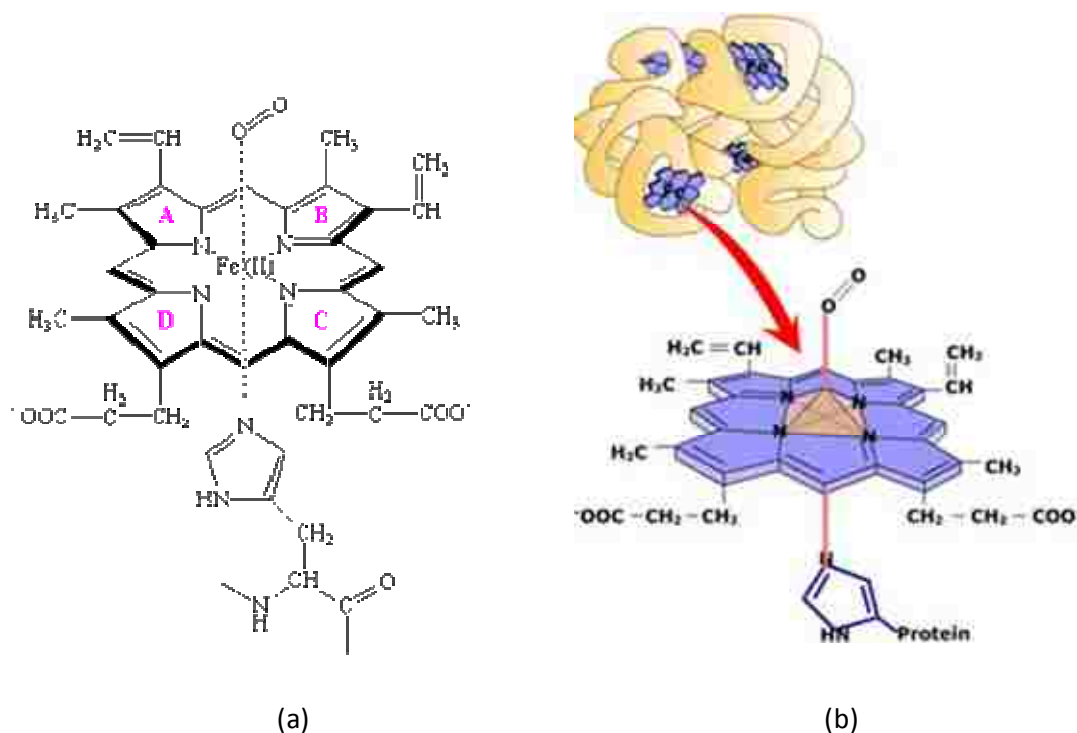
Figure 2.14. An iron (II) complex of porphyrin (heme): (a) Structural formula and (b) hemoglobin (http://chemed.chem.purdue.edu/).

2.3.2   Iron and human health

There are three main areas where the amount of bioavailable iron affects human health. The one that is most important numerically is iron deficiency, with usually leads to low haemoglobin levels and anemia. A large proportion of the world's population are iron deficient and in most cases iron sufficiency could be achieved relatively easily through a greater dietary intake of bioavailable iron. Many iron-containing preparations are currently used for the treatment of iron-deficiency anaemia. Oral iron treatments to achieve the daily dose of 100-200 mg are usually used. Iron (II) salts are more commonly used than iron (III) salts because the former are more soluble. The main compounds are iron (II) fumarate,

50

gluconate, sulfate, cuccinate etc. Secondly, too much iron, or iron overload, is not so common. Primary haemochromatosis results from a genetic defect leading to enhanced iron uptake. Secondary haemochromatosis occurs because excess iron has accumulated in the body as a result of the extensive blood transfusions. The treatment is to remove excess non-heme iron by chelation therapy, or the removal of both heme and non-heme iron by bleeding. The third area is the role of iron in infection. Because iron is essential for the growth of microbes, pathogenic microbes growing in plants and animals usually do so under iron-limited conditions. Consequently, many microbes have envolved complex mechanisms to acquire their iron.

2.3.3 Environmental impact

Until now, there has been no report on the ecotoxicity of iron nanoparticles in soil, water, and groundwater. Based on our knowledge on iron corrosion, iron in water or groundwater environment tends to form iron (II) or iron (III) oxide. Both forms are easy to be separated from water and have an advantage to absorb some toxic organic chemicals.   The study of reactions on the surface of iron nanoparticles provides evidence to confirm that after reacting with hazardous hydrocarbon and water, the shell of iron nanoparticles forms iron oxide at the outer surface, called core-shell structure model (Li and Zhang 2006, Li et al. 2006b). Based on the core-shell structure model, we can expect that iron nanoparticles may react with their surrounding chemicals including chlorinated hydrocarbon, water, and even oxygen and finally form their oxide form, which does not danger their environment. On the other hands, bimetallic iron nanoparticles such as Pd/Fe and Ni/Fe might gain some problems due to the releasing undesirable metals such as Pd

51

and Ni into the groundwater. However, due to their highly reactive power, the studies on their impact are still required.

CHAPTER 3

Experimental Section

3.1 Synthesis of nano particles

3.1.1 Synthesis of nZVI

The nZVI was prepared by reducing ferric chloride with sodium borohydride. Equal volumes of 0.94 M $NaBH_4$ and 0.18 M $FeCl_3$ were quickly mixed in a batch reactor. The borohydride was slowly metered into the ferric chloride solution stirred at ~400 rpm. The redox reaction can be formulated as :

$$4Fe^{3+}_{(aq)} + 3BH_4^-{}_{(aq)} + 9H_2O \rightarrow 4Fe^0_{(s)} + 3H_2BO_3^-{}_{(aq)} + 12H^+_{(aq)} + 6H_{2(g)} \qquad (3.1)$$
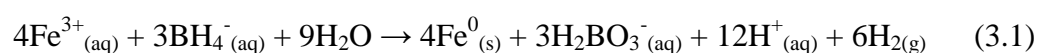
Additional 10 min was given to complete the reaction after the titration was completed. The formed iron nanoparticles were harvested by vacuum filtration through 0.2 µm filter papers. The iron particles were then washed several times with DI water and ethanol before use. The average particle diameter of nZVI was around 60-70 nm, as determined by scanning electron microscopy. The finished nanoparticles were washed with ethanol, purged with nitrogen, and refrigerated in a sealed polyethylene container under ethanol ($<5\%$) until use. The residual water content of the nanoparticles as used typically varied between 60-70%.

3.1.2 Synthesis of polymer stabilized nZVI

Polyvinyl alcohol-co-vinyl acetate-co-itaconic acid (PV3A), Polyacrylic acid (PAA), sodium salt, and soy powder were used to prepare aqueous

53

suspensions of nZVI. Figure 3.1 illustrates the molecular structure of PV3A, PAA and soy proteins. PV3A, with molecular weights in the range of 4300-4400, is a food grade material, biodegradable and nontoxic, likely due to the presence of highly biodegradable –OH, –CO–, and –COOH groups in the molecules (Sun et al. 2007). PAA with molecular formula $[CH_2CH(CO_2Na)]_n$ contains carboxylic acid (-COOH) groups for stabilizing nZVI. In an alkaline solution, carboxylate is assumed to be the anchors coordinating onto the iron surface (Harris et al. 2003, Wu et al. 2004) and thus provide iron particles with additional charges. Monomers of natural soy proteins have amino acid residues linked by amide bonds to form polypeptide chains. The polypeptide chains can interact with each other and entangle into complicated three-dimensional structures by disulfide and hydrogen bonds with a molecular weight ranging from 300,000 to 600,000 Dalton (Da). Soy proteins can be divided into water-soluble albumins and salt solution-soluble globulins. Most soy proteins are globulins, containing about 25% acidic amino acids, 20% basic amino acids, and 20% hydrophobic amino acids (Wool and Sun 2005).

PV3A stabilized nZVI was prepared in a 500 mL flask reactor with three open necks. The center neck hosted a mechanical stirrer with a speed set at 60 rpm. 2 g/L of nZVI particles was mixed with PV3A with the mass ratio of PV3A to nZVI from 0.05 to 0.1. In other words, the dose of PV3A accounted for 5-10% of nZVI mass. The solution was mixed for 2 h at pH 9.5-10 under ambient temperature conditions (23 ± 0.5 ℃). Similar procedures were also conducted for synthesizing the PAA and soy proteins stabilized nZVI.
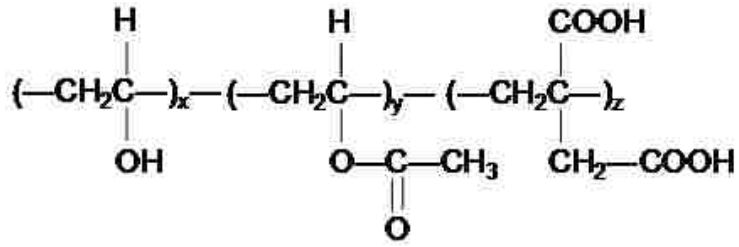
a) Polyvinyl alcohol-co-vinyl acetate-co-itaconic acid (PV3A)
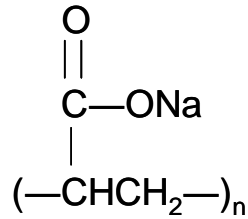
b) Poly acrylic acid (PAA)
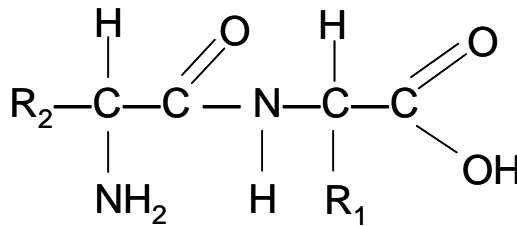
c) Soy proteins: An example of representative molecular structure

Figure 3.1. Molecular structures of (a) polyvinyl alcohol-co-vinyl acetate-co-itaconic acid (PV3A), (b) poly acrylic acid (PAA), and (c) soy proteins.

3.1.3 Synthesis of nCaO$_2$

A laboratory-use ball mill (Labstar®) from Netzsch (Exton, PA, USA) was used to produce nano particles of calcium peroxide. The mechine contains 2 sub-system: (1) the milling system consisting of a motor, a grinding chamber, an agitator and beads, and (2) a particle circulation and cooling system containing a pump and a holding tank to control the temperature of the particle suspension in

55

the tank and inside the mill. In a typical milling cycle, 1-2 kg of particles can be processed per batch. The setting used and the results achieved (e.g. power input, milling time, and product yeild) on this mill are linearly scalable for large-scale production-sized mills which can process over 1000 kg of particles each batch (Li et al. 2009).

The steel beads (dia.250 µm) were loaded into the milling chamber as the milling medium. The milling speed was 2000-2500 rpm to stir up the milling medium (beads). Calcium hydroxide ($Ca(OH)_2$) powder was added and smashed by the moving beads, and the impact energy fractures the micro scale powder into smaller particles. Liqiud H_2O_2 (30%) was added and the temperature of the milling chember was controlled to be less than 35 ℃. The nano scale calcium peroxide paerticles were produced via the reaction of $Ca(OH)_2$ and H_2O_2. A stainless steel cylinder screen with laser-cut slots fits in at the open end of the agitator, which functions as a filter to retain the milling beads but allow the processed materials to pass through and go into the holding tank. From the holding tank the particles were recycled back to the milling system by circulation pump. The milling procedure used here begins with mixing 1000 grams of the feed particles in the holding tank for 30 minutes before the circulation pump and the motor was turned on. The particle samples can be collected at the outlet of the grinding chamber to assess the size reduction.

3.2 Analytical Methods

3.2.1 Transmission electron microscopy (TEM)

Images of nZVI were recorded with a Philips EM 400T TEM (Philips Electronics Co., Eindhoven, Netherlands) operated at 100 kV. The TEM samples were prepared by depositing two to three droplets of the sample suspension onto a holey carbon film (Ernest Fullam, Inc., Latham, NY), which was completely dried in a fume hood prior to the TEM analysis.

TEM operates on the same basic principles as light source microscope except that TEM uses electrons instead of light and electromagnetic lenses. The electron source at the top of the microscope emits electrons, which travel down the vacuum column in the microscope. These electrons are focused by the electromagnetic lenses into a very small beam which travels through the specimen. Due to the interaction between the electrons and the specimen, some electrons are scattered and some are not. The unscattered electrons hit the fluorescent screen at the bottom, giving rise to a "shadow image" of the specimen. Compared to light microscope, whose resolution is restricted by the wavelength of visible light, the resolution of TEM is thousand times higher and can study materials at near atomic level. (Williams and Carter, 1996; http://nobelprize.org).

3.2.2 Scanning Electron Microscope (SEM)

Morphology characterization of nZVI was carried out using a field-emission scanning electron microscope (FE-SEM) (Hitachi 4300). The popularity of SEM for characterizing nanomaterials stems from its capability of obtaining 3-dimensional-like topographical images in secondary electron (SE) imaging mode, Z-contrast imaging using back-scattered electrons (BSE), and quantitative

57

elemental mapping with energy-dispersive X-ray spectrometer (XEDS) (Goldstein 2003). Imaging under SE mode was typically conducted at 5 kV accelerating voltage. Samples with poor electron conductivity (e.g. severely oxidized surfaces) were coated with a thin layer of iridium to minimize surface charging.

3.2.3 X-ray diffraction

X-ray diffractogram was obtained with a Rigaku diffractometer (Rigaku, Japan) with Cu Kα (λ= 1.5418 A) radiation generated at 40 kV. Bragg Equation (Eq. 3.2) was used to convert from diffraction angel (θ) to the lattice spacing (d):

$$n\lambda = 2d \, sin\theta \tag{3.2}$$

Samples were scanned from a 2 θ range of 10° to 80° with a stepping size of 0.1^0 and a scanning rate of 60 second per step. The crystalline phase was identified by comparing with XRD diffraction patterns in the literature (JCPDs 1998).

3.2.4 Atomic Absorption (AA) Spectroscopy

Atomic absorption (AA) method was used to measure the iron concentration in solution samples. 1 mL nZVI suspension was first transferred into a 100 mL volumetric flask and mixed with 50 mL of 2.4 N of HCl and 0.27 N of HNO_3. The solution was mixed for 1 h. DI water was then added to make up the solution to 100 mL. The solution was then diluted for AA analysis. A Perkin Elmer AAnalyst 200 Atomic Absorption Spectrometer was used in this work.

Atomic absorption spectroscopy is one of the most common instrumental methods for quantitative analyzing for metals and some metalloids. In its atomic form, an element will absorb light when it is excited by heat. The adsorbed light is

58

characterized for each element and the amount of absorbed light is proportional to the concentration of the element.

3.2.5 Gas Chromatography (GC)

Aqueous and gaseous TCE concentrations were analyzed by a gas chromatograph (Shimadzu GC-17A) equipped with a flame ionization detector (FID) and Supelco SPB-624 capillary column (30m × 0.53mm). Temperature conditions were programmed as follows: oven temperature at 40 °C for 5 minutes and temperature was increased at rate of 10°C/min until oven temperature reach 200 °C for 5 minute with a split ratio of 10; injection port temperature at 250 °C; and detector temperature at 300 °C. The carrier gas was ultra-pure helium at a flow rate of 30 cm.min^{-1}. The method follows the EPA procedures.

Gas product identification was analyzed by a gas chromatograph (HP 5890) equipped with a flame ionization detector (FID) and CP PoraPLOT Q fused silica capillary column (10m × 0.32mm). Temperature conditions were programmed as following: oven temperature at 33 °C for 1 minutes and temperature was increased at rate of 25°C/min until oven temperature reaches 200 °C for 5 minutes; injection port temperature at 200 °C; and detector temperature at 225 °C. The carrier gas was ultra-pure helium at a flow rate of 8.6 mL.min^{-1}. Standard hydrocarbon gas contained C1 – C6 gas was used as peak identification.

The sample was injected through the injector port, where it was vaporized and transported through the column by the flow of inert, gaseous mobile phase (Helium). The column contains a stationary phase, where the compounds in the sample were separated and the compound signal was detected by a flame ionization detector (FID).

59

3.2.6   pH/Standard Potential (E_h) measurement

A combination pH electrode (Orion) was used in conjunction with a Sension1 (Hach) meter to track the solution pH. It was calibrated prior to each test. A combination Ag/AgCl reference electrode (Cole-Parmer) was used with a Model 420A pH/ORP meter (Orion) to monitor redox potential and was calibrated with fresh ZoBell solution before each test. Measured redox potential readings (mV) were converted to E_h, the potential relative to the standard hydrogen electrode, as a function of solution temperature by adding +199 mV at 25°C.

3.3 Chemical and Materials

ACS grade ferric chloride ($FeCl_3$) was purchased from Alfa Aesar. Sodium borohydride ($NaBH_4$) with 98% purity was obtained from Finnish chemicals (Finland). Polyvinyl alcohol-co-vinyl acetate-co-itaconic acid (PV3A) and sodium bromide (NaBr) were from Aldrich. Poly(acrylic acid), sodium salt (PAA) with molecular weight ranging from 4,300 to 4,400 g/mol and 40 wt% solution was purchased from Polysciences, Inc. Standard Ottawa sand, designated as ASTM 20/30 was from U.S. Silica Company. Hydrochloric acid (12.1 N) and nitric acid (15.8 N) were purchased from EMD Chemicals and Fisher Chemicals, respectively. Soy proteins (Gold 300 soy powder, 300 mesh) with 40% protein and 20% fat were obtained SoyLink[TM], Iowa. Hydrochloric acid (12.1 N) and nitric acid (15.8 N) were purchased from EMD Chemicals and Fisher Chemicals, respectively. Pentane $\geq$ 99%, spectrophotometric grade was obtained from Sigma-Aldrich. 95% ethanol was purchased from Pharmco-AAper.

60

CHAPTER 4

Trichloroethylene Pure Phase removal by nano-scale Zerovalent Iron

Particles

4.0 Abstract

Trichloroethylene (TCE) is known as high toxic chlorinated hydrocarbon for groundwater. Direct removal of TCE from liquid phase contaminated sources can speed up the remediation processes. In this report, batch experiments were conducted to study the direct reaction of nano-scale zerovalent iron (nZVI) particles and TCE in liquid phase. Results show that nZVI has capability to remove pure TCE via reduction reactions. The reaction products were analyzed by GC using samples collected from head space. The results suggest that there is a mechanism other than reduction reaction corresponding to removal of pure TCE in batch experiments. Mass balance analysis demonstrate that 7 – 9 % TCE mass was trapped in 1 g of nZVI sludge indicating absorption occurred during the removal process. However, when amount of nZVI was increased in the batch experiment, TCE removal efficiency compared to the stoichiometric reaction calculation was decreased. The reaction and absorption abilities of nZVI are depended upon its surface areas.   Increasing amount of nZVI reduces the space of batch experiment systems, so TCE removal efficiency of nZVI is decreased. Continuously adding small amount of nZVI can increase TCE pure phase removal efficiency.

4.1 Introduction

Trichloroethylene (TCE: C_2HCl_3) is known as high toxic chlorinated hydrocarbon not only for human, but also for the environment. TCE has been used as a solvent to remove grease from metal parts and a solvent to make other chemicals. TCE can be found in some household products, including typewriter correction fluid, paint removers, adhesives, and spot removers. TCE is one of Dense Nonaqueous Phase Liquids (DNAPL), which has higher density than water; therefore, it may penetrate into unsaturated or saturated zones under the influence of gravity. Because it is denser than water, TCE tends to sink in water and exists as a separate phase in the deep subsurface below the water table. TCE can be slowly dissolved in water and this limits the effectiveness of conventional pump-and-treat methods. The flow pattern of TCE within the various permeability zones of the aquifer increases the complexity of the remedial process required for cleanup (Tsai et al. 2009). Because DNAPL is immobile under normal subsurface conditions, they can act as a long-term source for continuing dissolution of contaminants into the passing ground water. TCE is often considered to be the continuous long-term sources of halogenated organic contaminants (HOCs) to groundwater.

Permeable reactive barriers (PRBs) containing granular zero-valent Iron (ZVI) have shown the effective results for the remediation of chlorinated organic solvents in contaminated aquifer (Wilkin et al. 2003, Puls et al. 1999). Even though, conventional PRBs can serve as TCE remediation very well, there are many limitations of using PRBs. As illustrated in Figure 1, PRBs can only be used to treat contaminated TCE dissolved in ground water and PRBs is a passive method that is relied on ground water flowing through it (Fig. 4.1), so PRBs requires very huge areas, and that means high construction cost and long time to

62

clean all TCE contaminants. PRBs as shown in Fig. 4.1 cannot treat the contaminants that stay deep down under its construction length underground. Even though the promising results of TCE remediation by PRBs with ZVI have been reported, these PRBs-ZVI also produce considerable amounts of chlorinated intermediates and byproducts such as dichloroethylenes, acetylene and vinyl chloride due to the reaction mechanism of ZVI with TCE (Su and Puls 1999, Roberts et al. 1996, Arnold and Roberts 2000, Orth and Gillham 1996). Treatment mechanism is due to oxidation-reduction reactions when iron acts as electron donors and chlorinated hydrocarbons receive electrons (Vogel et al. 1987). In the reaction between TCE and ZVI, TCE is reduced and releases chloride ions, while iron is oxidized and donates electrons (Gillham and Ohannesin 1994, Matheson and Tratnyek 1994, Roberts et al. 1996, Orth and Gillham 1996, Arnold and Roberts 2000).

For more than a decade, PRBs-ZVI has been used to treat TCE-contaminated groundwater plumes from TCE source areas and has focused on the treatment of TCE dissolved in groundwater, but there is no report on the method that directly remove TCE pure phase contaminated sources. Directly removing TCE contaminated sources can speed up the contaminated site remediation processes and decrease time and cost of treatment process. The discovery of nano-scale zerovalent iron particles (nZVI), which enhance the ability to treat chlorinated hydrocarcon with less production of chlorinated intermediates and by products, motivates an interesting idea of direct removal of TCE contaminated sources. Figure 4.1 shows the schematic ideas of using nZVI to directly treat TCE pure phase contaminated sources.
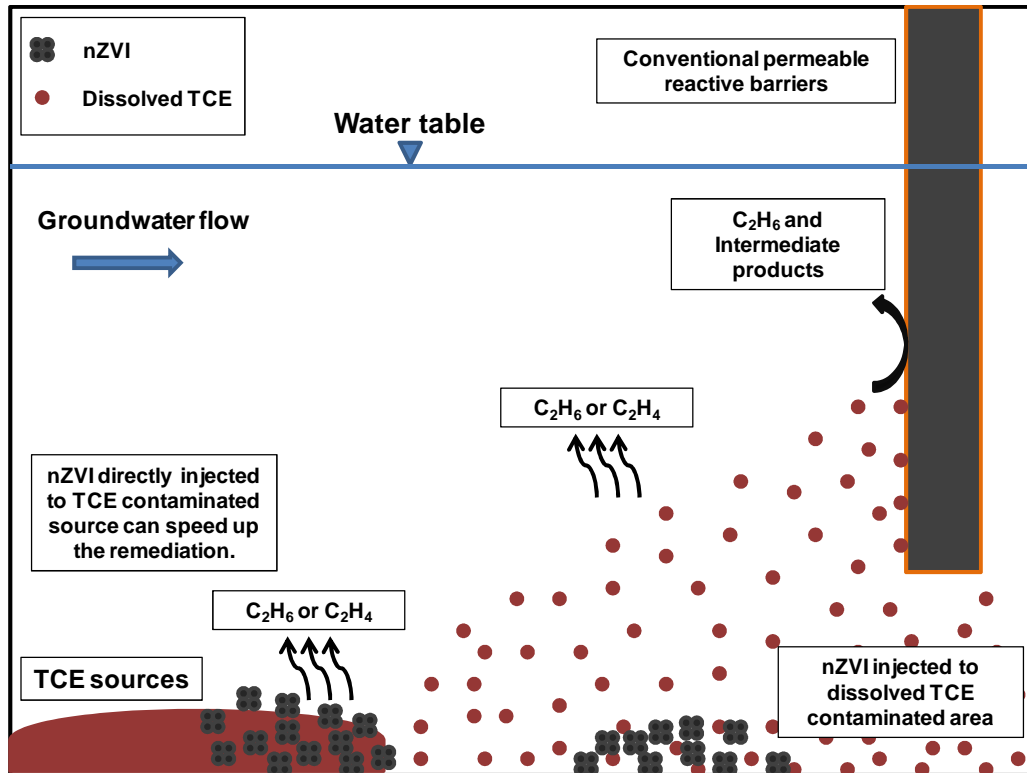
Figure 4.1. The schematic picture for using nZVI to directly treat TCE pure phase contaminated sources.

The reduction power of nZVI is depended on its size in nanoscale (< 100 nm) (Zhang 2003, Wang and Zhang 1997, Cheng et al. 2006) and the dechlorination reaction rate of ZVI is depended upon the surface reaction (Matheson and Tratnyek 1994, Johnson et al. 1996). Therefore, nZVI in nano scale with huge specific surface at around 34 $m^2.g^{-1}$ compared to less than 3 $m^2.g^{-1}$ of micro scale ZVI (Zhang et al. 1998, Sun et al. 2006) has a very fast dechlorination reaction rate. Extensive laboratory studies have demonstrated that nZVI is a very effective material for transforming a wide array of environmental contaminants such as chlorinated organic solvents, organochlorine pesticides, polychlorinated biphenyls (PCBs), organic dyes, and various inorganic compounds (Zhang 2003, Lien and Zhang 2001, Wang and Zhang 1997, Li et al. 2006b). Several field tests

64

have also conducted the promising prospects for in situ remediation (Elliott and Zhang 2001, Glazier et al. 2003). Recently, bimetallic nano-scale particles such as Pd/Fe and Ni/Fe have been created and have much higher TCE dechlorination rates than nZVI (Elliott and Zhang 2001, Wang and Zhang 1997, Lien and Zhang 2001, Lien and Zhang 1999, Schrick et al. 2002, Zhang 2003, Ponder et al. 2000, Ponder et al. 2001). Their high reaction rates are due to their high specific surface and the addition of a catalyst. Although bimetallic partilces effectively degrade TCE with less production of chlorinated intermediates, they may themselves create environmental problems by releasing undesirable metals such as Pd and Ni into the groundwater. However, all TCE dechlorinations with nZVI mechanisms have been studied when TCE is dissolved in aqueous solution. Therefore, the phenomena occuring when nZVI mixes with TCE pure liquids are still unclear. The objectives of this report are to study the capability of using nZVI to remove TCE pure phase and the mechanisms and factors that affect the TCE pure phase removal processes.

4.2 Materials and Methods

4.2.1   Chemical reagents

ACS grade ferric chloride (FeCl$_3$) was purchased from Alfa Aesar. Sodium borohydride (NaBH$_4$) with 98% purity was obtained from Finnish chemicals (Finland). Hydrochloric acid (12.1 N) and nitric acid (15.8 N) were purchased from EMD Chemicals and Fisher Chemicals, respectively. Pentane $\geq$ 99%, spectrophotometric grade was obtained from Sigma-Aldrich. 95% ethanol was purchased from Pharmco-AAper.

4.2.2   Synthesis of nZVI

The nZVI used in this work was prepared with the reduction of ferric chloride by sodium borohydride. Equal volumes of 0.94 M $NaBH_4$ and 0.18 M $FeCl_3$ were quickly mixed in a batch reactor. The borohydride was slowly metered into the ferric chloride solution stirred at ~400 rpm. The redox reaction can be formulated as follows:

$$4Fe^{3+}_{(aq)} + 3BH_4^-{}_{(aq)} + 9H_2O \rightarrow 4Fe^0{}_{(s)} + 3H_2BO_3^-{}_{(aq)} + 12H^+{}_{(aq)} + 6H_{2(g)} \qquad (4.1)$$
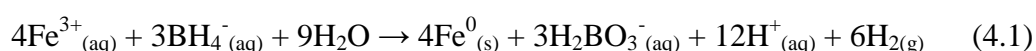
Additional 10 min was given to complete the reaction after the titration was completed. The formed iron nanoparticles were harvested by vacuum filtration through 0.2 µm filter papers. The iron particles were then washed several times with DI water and ethanol before use. The average particle diameter of nZVI was around 60-70 nm, as determined by scanning electron microscopy. Detailed procedures on the nZVI synthesis and characterization have been previously published (Sun et al. 2006, Sun et al. 2007, Wang and Zhang 1997). The finished nanoparticles were washed with ethanol, purged with nitrogen, and refrigerated in a sealed polyethylene container under ethanol ($<5\%$) until use. The residual water content of the nanoparticles as used typically varied between 60-70%.

4.2.3   Batch Experiments

Open-batch reaction experiments were conducted in screw cap 30 ml glass vials (VWR), and closed-batch reaction experiments were in 20 mL glass vial with a seal cap for reaction time experiments. 2 mL of pure TCE was mixed with various mass of nZVI ranging from 1 – 3 g for open-batch experiments and 0.5 – 2

66

g for closed-batch experiments and 10 mL of distilled water; then placed in 30 rpm vertical rotor at room temperature (22 ± 1 °C) with various time periods. Then, at certain times, mixed samples were centrifuged at 6,000 rpm to separate the liquid part from the solids for 30 minutes and the liquid part was filtrated by syringe filter (Millex-LG Syringe-Driven Filter Unit 0.2 µm). Volumes of TCE remaining in test tubes in various time periods were measured and the aqueous solutions of each sample were taken and aqueous TCE samples were extracted by n-Pentane (Liang et al. 2007). TCE concentration was quantified by gas chromatography (GC). Similar batch experiments were set up with various amounts of nZVI including 0, 1, 2, 3 and 4 g for open-batches and 0.5, 1 and 2 g for closed-batches.

Mass balance batch experiments were conducted in 20 mL glass vial with a seal cap. To avoid the error of volume-mass conversion, only 0.2 mL pure phase TCE was mixed with 10 mL of water and 1 and 3 g dried nZVI and placed in 30 rpm vertical rotor at room temperature (22 ± 1 °C) for 24 hours. Head space air of each sample was collected by using a 25 µL gastight syringe and TCE was measured by GC. Then, mixed samples were centrifuged at 6,000 rpm to separate the liquid part from the solids for 30 minutes. The aqueous solutions of each sample were taken and aqueous TCE samples were extracted by n-Pentane (Liang et al. 2007). TCE concentration was quantified by gas chromatography (GC). Some of the solid sludge was collected into 5 mL vial and the weight of sludge sample was measured. TCE in sludge samples was extracted by n-pentane and measured by GC.

4.2.4 Analytical Method

TCE volume: The volume of TCE remaining in sample liquids was measured by using 15 mL "fine measurement scale graduated centrifuge tubes" by Kimble Kontes LLC.

TCE concentration: Aqueous TCE samples from batch experiments were measured by using n-Pentane extraction (Liang et al. 2007). Liquid and gaseous TCE samples were analyzed by a gas chromatograph (Shimadzu GC-17A) equipped with a flame ionization detector (FID) and Supelco SPB-624 capillary column (30m × 0.53mm). Temperature conditions are programmed as following: oven temperature at 40 °C for 5 minutes and temperature is increased at rate of 10°C/min until oven temperature reaches 200 °C for 5 minutes with a split ratio of 10; injection port temperature at 250 °C; and detector temperature at 300 °C. The carrier gas was ultra-pure helium at a flow rate of 30 cm.min^{-1}. The method follows the EPA procedures.

Gas product identification: Head space gas of closed-batch reaction was analyzed by a gas chromatograph (HP 5890) equipped with a flame ionization detector (FID) and CP PoraPLOT Q fused silica capillary column (10m × 0.32mm). Temperature conditions was programmed as following: oven temperature at 33 °C for 1 minutes then temperature was increased at rate of 25°C/min until oven temperature reaches 200 °C for 5 minutes; injection port temperature was set at 200 °C and detector temperature at 225 °C. The carrier gas

68

was ultra-pure helium at a flow rate of 8.6 mL.min^{-1}. Standard hydrocarbon gas contained C1 – C6 gases and it was used as peak identification.

4.3 Results and Discussions

Figure 4.2 shows the volume removal of TCE in open-batch and closed-batch reactors over various periods of times. The separated clear liquid at the bottom of graduated centrifuge tubes in Figure 4.2a is TCE pure phase in 1 g nZVI open-batch experiment. The start volume of TCE pure phase in each batch was 2 mL. The result shows that TCE pure phase is decreased by nZVI. When reaction time was increased, more pure TCE was removed. The removed volumes of TCE were measured and presented in Figures 4.2b, 4.2c and 4.2d. Volumes of TCE in open-batch reactors in Figure 2b were removed rapidly by 0.5, 0.6 and 0.8 mL within 10 hr for 1, 2 and 3 g nZVI, respectively. After 24 hr these amounts increase to 0.85, 0.95 and 1.2 mL for 1, 2 and 3 g nZVI, respectively. It should be noted that a linear relationship of pure phase TCE volume loss in open reactors was observed in the absence of nZVI. This could be due to TCE evaporation (TCE B.p. 87.2 °C) during the circulation process (Fig. 4.2b). Therefore, after subtracting the loss of TCE in systems, the net volume reduction of TCE by nZVI is shown in Figure 4.2c. The net volumes of TCE in open-batch reactors in Figure 4.2c were 0.4, 0.55 and 0.75 mL at 10 hr for 1, 2 and 3 g nZVI, respectively, and 0.48, 0.6 and 0.85 mL for 1, 2 and 3 g nZVI, respectively at 72 hr. The net volume reduction data indicate that the reaction of TCE and nZVI was occurred rapidly within 10 hr. The volume reduction of TCE in open-batch reactors after 10 hr might be related to TCE transferring phase from liquid to gas. The results in closed-batch reactors in Figure 2d also show that the reactions of TCE and nZVI occur rapidly within the first 10

69

hr. The volume removal of TCE in closed-batch reactors in Figure 4.2d was 0.4, 0.5 and 0.7 mL at 10 hr for 0.5, 1 and 2 g nZVI, respectively, and then no volume decrease was observed.
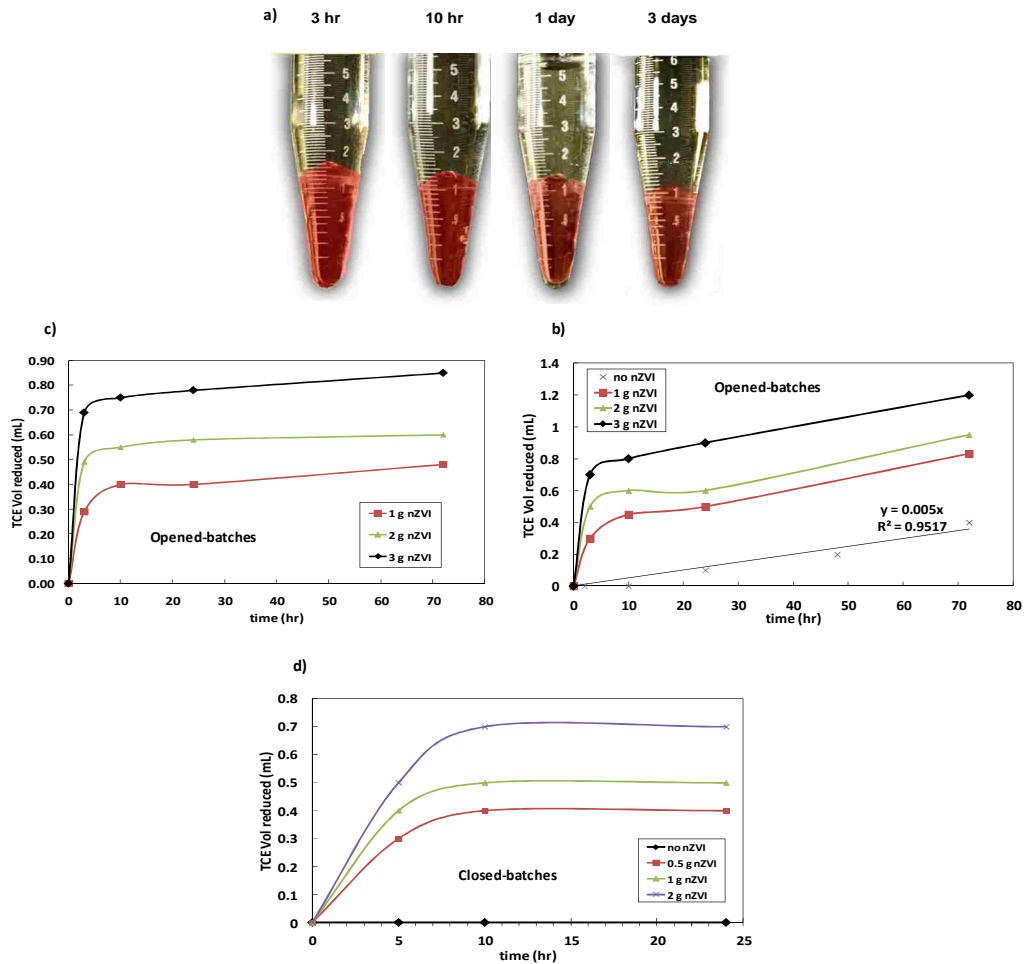
Figure 4.2. TCE pure phase volume reduction by nZVI: a) TCE pure phase remained in test vials after reacting with nZVI, b) TCE pure phase volume reduction in open-batch experiments with various times, c) net volume reduction in open-batch experiments with various reaction times and d) TCE pure phase volume reduction in closed-batch experiments with various times.

70

Figure 4.3 presents the environmental conditions of closed-system experiments including Oxidation reduction potential (ORP: mV) and dissolved oxygen (DO: mg/L). ORP of all closed-batches showed significant decrease to around -550 to -600 mV at 5 hr reaction time and still be around -500 to -600 mV throughout the experiments, but for no nZVI closed-batch, ORP of the system is around 50 to -50 throughout the experiment (Fig. 4.3a). DO also showed a similar decrease (Fig 4.3b). Although we expected to see the zero concentration of dissolved oxygen in all nZVI samples, but DO was still detectable in all samples because plastic DO probe cannot be used in the mixtures that contain pure TCE (because TCE is a solvent that can dissolve plastic); therefore, DO measurement was conducted in the clear separated solution samples. During the separation process, oxygen can dissolve into the samples. However, DO of all closed-batches decreased to around 1.3 mg/L in 5 hrs reaction time and stayed unchanged around 1 to 1.5 mg/L throughout the experiments (Fig 4.3b). The ORP and DO results indicate that only reductive reactions occur in all of batch experiments that we have studied.

71
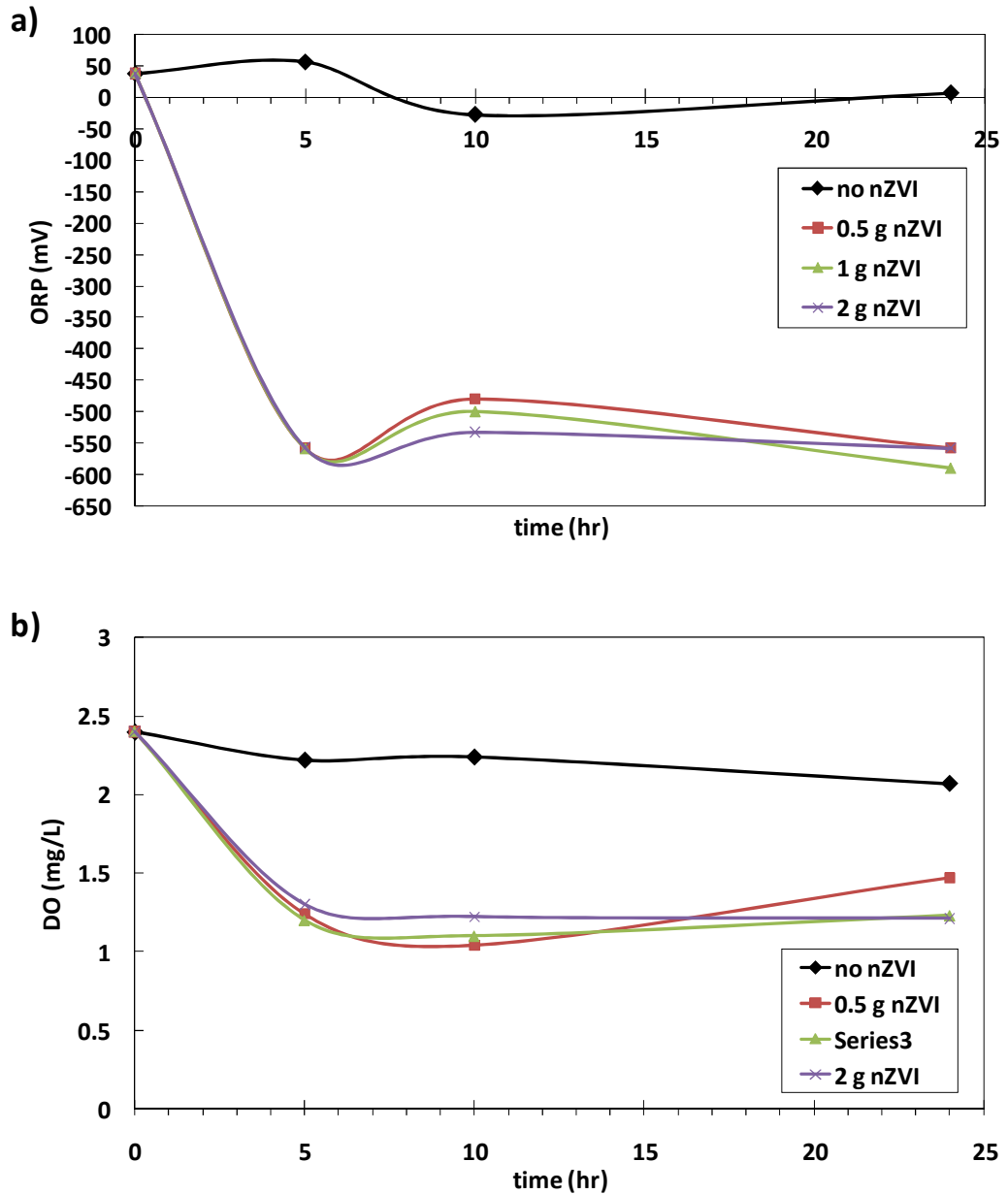
Figure 4.3. Closed-batch experiments reaction evidence: a) ORP measurement and b) DO in clear solution after centrifugation.

Figure 4.4 presents TCE concentration in aqueous solution of 1 g nZVI open-batch reaction experiment at various periods of reaction times. TCE concentration in solution samples without nZVI was rapidly reached to solubility concentration (around 1,100 mg/L) within 1 hr. On the other hand, TCE

72

concentration in TCE – nZVI reaction samples was increased to around 600 mg/L after few hours of experiments and slowly increased to 650 mg/L after 24 hr. The concentration of TCE in aqueous solution is related to three factors: 1) dissolution rate from pure liquid phase to aqueous phase, 2) adsorption rate of TCE to the surface of nZVI and, 3) reaction rate of TCE with nZVI at the surface of nZVI (Arnold and Roberts 2000, Tee et al. 2009). Dissolution and adsorption processes are occurred in very fast rates because of the mixing in the batch experiments. Therefore, the reaction process may be the major factor that controls the concentration of TCE in aqueous phase. The reaction rate of ZVI is due to the surface reaction (Matheson and Tratnyek 1994, Johnson et al. 1996). nZVI in nano scale has huge specific surface at around 34 $m^2.g^{-1}$ compared to less than 3 $m^2.g^{-1}$ of micro scale ZVI (Zhang et al. 1998, Sun et al. 2006); hence, the reaction of nZVI can occur very fast. Based upon the results in Figure 4.4, the concentration of TCE in aqueous phase is increased rapidly at the first several hours due to the dissolution rate, while the reaction of TCE on the surface of nZVI is occurred and maintains the concentration at the certain level. However, the reaction rate was decreased due to the reduction of available surface of nZVI and the formation of iron oxide on the surface of nZVI (the core-shell structure model) (Li and Zhang 2006, Li et al. 2006b). Therefore, the concentration of TCE tends to gradually increase and may finally reach to its solubility. Instead of rapid increase in TCE concentration, the slow rise of the concentration might due to the remaining reactive nZVI following core-shell structure model and the adsorption of TCE by iron oxide formed on the surface of nZVI (Li and Zhang 2006). The corresponding results of pure phase TCE volume reduction and TCE concentration in water

73

solution show the capability of nZVI to remove DNAPLs phase of TCE and lower
TCE dissolution.
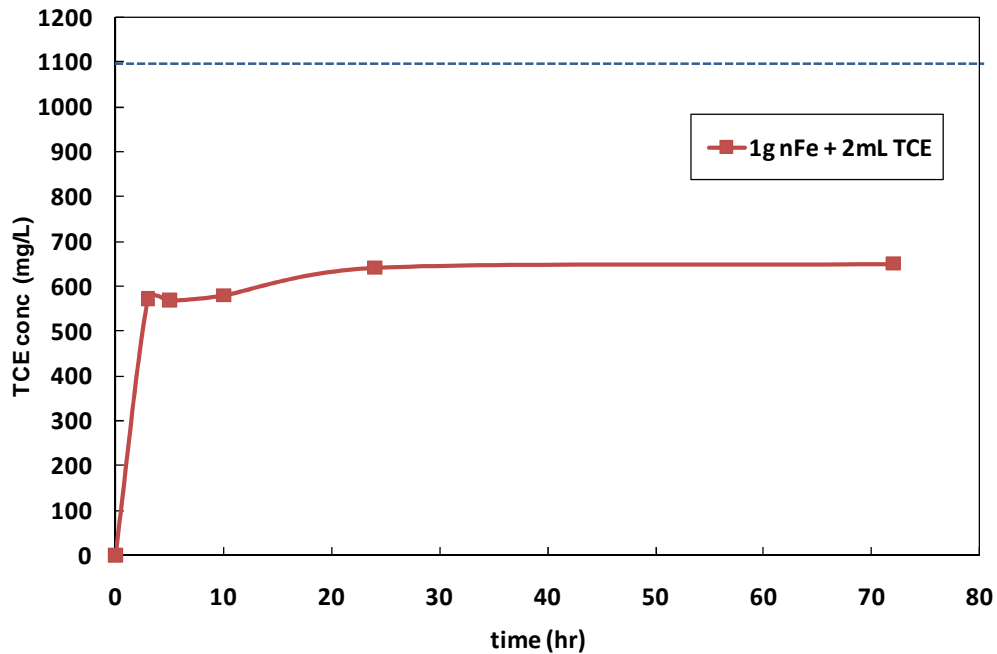
**Figure 4.4. TCE concentrations in water solution of 1 g nZVI reaction batch
experiment at various periods of reaction times.**

Head space gases of closed-batch samples, containing 0.2 mL of TCE
mixed with 1 g nZVI and 10 mL of water after 1 and 3 days of reaction times, was
injected into GC to measure TCE and other possible byproducts of the reaction.
For our GC temperature profile and gas velocity set up, peak of TCE showed up at
around 8 minute. Figure 4.5 shows GC results of head space gas of TCE – nZVI
reaction samples. There is an unknown peak found at around 1.7 minute on 1 day
and 3 days reaction samples and then TCE peak appears at 8 minute. The peak at
the 1.7 minute showed increase of area from the 1st day to the 3rd day. There was
no peak in any nZVI control samples at 1.7 min from both the 1st and the 3rd day

74

samples. Moreover, the areas of TCE peak in TCE-nZVI samples decrease by 23.4% from 1st day sample to 3rd day samples. The increase in unknown peak in this case can be expected as a product of TCE-nZVI reaction. Head space gas product was identified by GC, which consisted of two components: ethane (peak at 1.8 – 1.9 min.) and ethylene (peak at 2.1 – 2.2 min).

There are several reports about the products of TCE dechlorination by zero valent iron (ZVI). The reaction between TCE and zero valent iron is due to reduction-oxidation reaction in which TCE is reduced and releases chloride ions, while iron is oxidized and supplies electrons (Gillham and Ohannesin 1994, Matheson and Tratnyek 1994, Roberts et al. 1996, Orth and Gillham 1996, Arnold and Roberts 2000, Vogel et al. 1987). Ethane and ethylene are found as the main products with minor amounts of chlorinated intermediates formed via hydrogenolysis pathway and acetylene formed via β-elimination pathway (Roberts et al. 1996, Orth and Gillham 1996, Arnold and Roberts 2000, Su and Puls 1999). Liu et al. reported that 70 – 80 % of byproduct from TCE dechlorination by nZVI was ethane, 20 – 30 % of byproducts was C3-C6 intermediate products, and no acetylene was detected (Liu et al. 2005). Additionally, bimetallic nanoparticles of Ni/Fe and Pd/Fe have been reported that they have much more effectiveness in dechlorination than normal nZVI and no less-chlorinated intermediates are observed from the reactions of bimetallic nanoparticles (Lien and Zhang 2007, Tee et al. 2005, Lien and Zhang 2005).
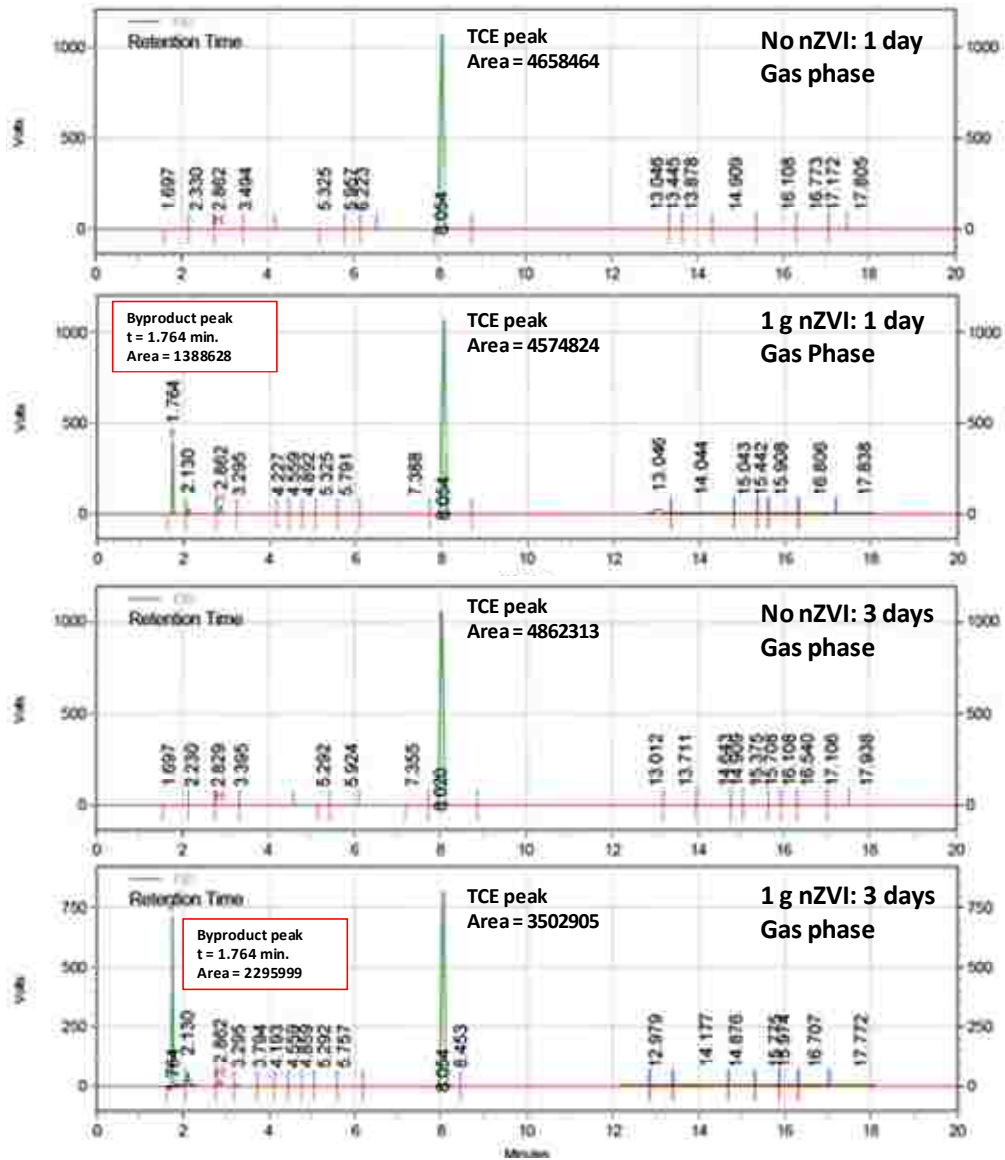
Figure 4.5. GC results of head space gas analysis of closed-batch experiments of 0.2 mL TCE mixed with 1 g nZVI at various reaction times.

Therefore, the reaction products in head space gas, the reductive condition in all batch experiments (Fig 4.3.), and the concentration of TCE in aqueous solution (Fig.4.4) are the evidence to confirm the occurrence of the TCE dechlorination by nZVI in this work.

76

According to the reaction products found in head space gas of the experiments, the reaction between TCE and nZVI was expected to be occurred in these experimental systems. However, when mixing nZVI, TCE, and water, there are several half-reactions happening simultaneously as following:

$$Fe^0 \rightarrow Fe^{2+} + 2e^- \tag{4.2}$$

$$TCE\ (C_2HCl_3) + 8e^- + 5H^+ \rightarrow C_2H_6 + 3Cl^- \tag{4.3}$$

$$2H_2O + 2e^- \rightarrow H_2 + 2OH^- \tag{4.4}$$

$$O_2 + 2H_2O + 4e^- \rightarrow 4OH^- \tag{4.5}$$

Electrons, donated from Fe^0 oxidation, are used to dechlorinate TCE, and they also react with water itself and oxygen dissolved in water. Stoichiometry of TCE dechlorinated by nZVI is calculated by combining Eq. 4.2 with Eq. 4.3:

$$C_2HCl_3 + 5H^+ + 4Fe^0 \rightarrow 4Fe^{2+} + C_2H_6 + 3Cl^- \tag{4.6}$$
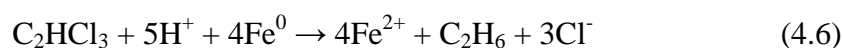
Based on Eq. 4.6, 4 mole of zero-valent iron are used to reduce 1 mole of TCE. Molecular weight (MW) of Fe = 55.95 and MW of TCE = 131.6. So, 1 g of zero-valent iron can reduce 0.59 g of TCE and specific weight (SW) of TCE = 1.46 g/mL. Based on the calculation, 0.4 mL of pure phase TCE can be dechlorinated to ethane by 1 g of nZVI. The results in Fig. 4.2c and 4.2d show that TCE was removed to 0.4 and 0.5 mL by 1 g dried of nZVI in open and closed batches, respectively. TCE removal results are nearly to or higher than TCE stoichiometry calculation at 0.4 mL/g nZVI. However, there is not only TCE dechlorination in equation 4.3 occurred in the system, but also other reactions in equation 4.4 and

77

4.5 happened simultaneously. Therefore, TCE decholination by nZVI alone cannot reach to stoichiometry. TCE removal results of batch experiment suggest that not only TCE dechlorination by nZVI is occurred, but also, there are other mechanisms occurred in this TCE pure phase removal by nZVI.

Figure 4.6 shows the relationship of TCE volume removal with various amounts of dried nZVI mass added into open (Fig. 4.6a and 4.6b) and closed (Fig. 4.6c) reactors. As shown in Figure 6a, increasing amount of nZVI removes more volumes of TCE and the linear relations with around 0.9 R^2 can be performed in both 1 day and 3 days open-batch experiments. After subtracting the volume reduction of pure TCE occurred by open-system leaking, the net volume removal of TCE by nZVI is shown in Figure 4.6b. Both 1 day and 3 day reaction show almost the same linear relation indicating that the activity between nZVI and TCE almost stops after 1 day and then the rest of volume reduction is due to TCE evaporating from liquids to gas phase. The results suggest that increasing amounts of nZVI increase the reaction and remove more volumes of TCE. Nevertheless, the effectiveness of the open-batch experimental reactions is around 60% compared to stoichiometry of TCE-nZVI reaction (calculated by ration of experimental slope to theoretical reaction slope). Figure 4.6c shows TCE volume removal with various amounts of dried nZVI mass added into closed reactors. As similar to open-reactors, increasing amount of nZVI in closed-system removes more volumes of TCE; however the increase of TCE volume removal in closed-system cannot be predicted by linear relationship. However, TCE removal in closed-batch reactors shows slightly higher than that in open-system experiments as expected because in closed-system, there is no outside air going into the system reactors, so nZVI only

78

reacts with all substances in the system without losing its reaction power due to the extra oxygen coming from the outside environment.

TCE concentration in aqueous phase for various amounts of nZVI in open-batch experiments is shown in Figure 4.7. Interestingly, at 3 day reaction, TCE concentration of all samples is around 600 mg/L. Higher amount of nZVI samples were expected to have lower concentration of TCE. TCE concentration of high amount of nZVI can be explained by the correspondence of the lower reaction rate in high amount of nZVI with the low removal effectiveness resulted from volume reduction above. The decrease of TCE volume reduction effectiveness and the increase of concentration of TCE in high amount nZVI experiments can be explained by the surface chemistry of nZVI. Increasing mass of nZVI in the very limited space such as the small vials in these experiments decreases the surface area of nZVI because of the high density of particles. The reaction rate of nZVI is governed by its high specific area (Zhang et al. 1998). Therefore, decreasing the surface of nZVI reduces the reaction rate of nZVI. As described previously, TCE concentration in aqueous phase is related to the reaction rate on the surface of nZVI. Therefore, the slower reaction rates are found at high amount of nZVI in batch experiments indicating the absence of the available surface of nZVI.
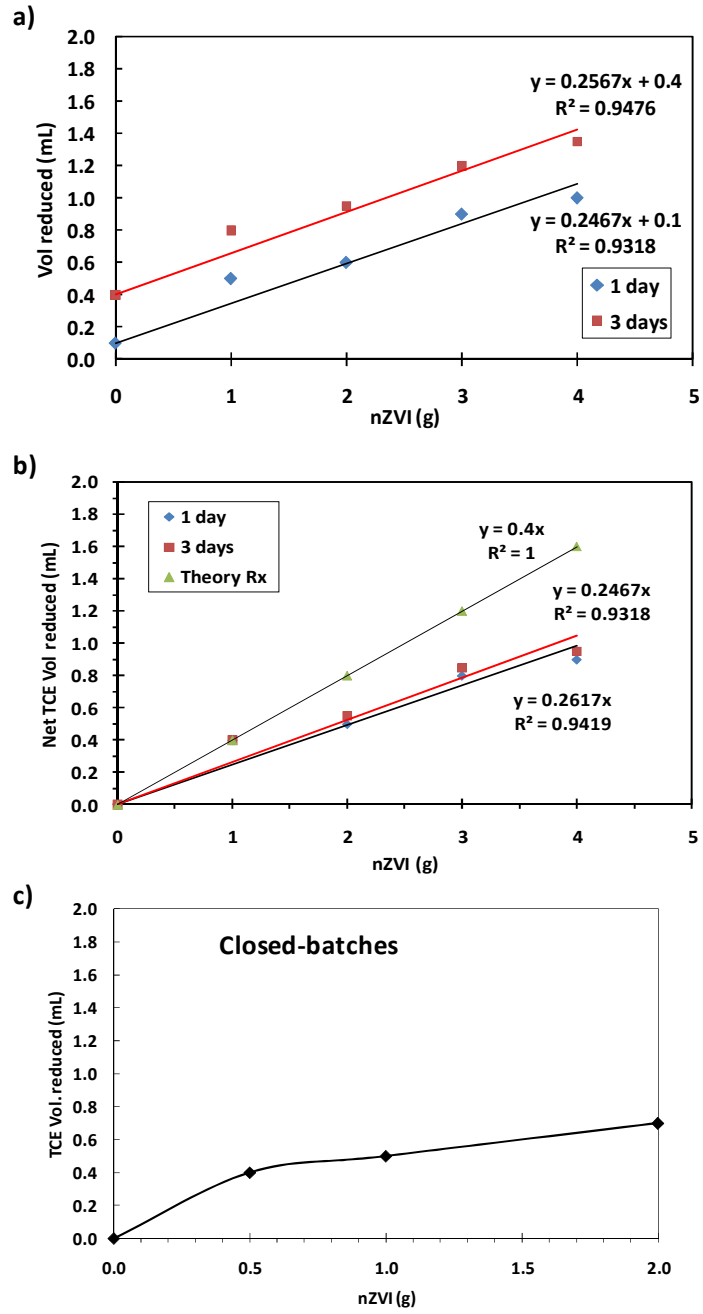
Figure 4.6. The relationship of TCE volume removal with various amounts of dried nZVI mass: a) TCE volume reductions in open-batch experiments, b) Net TCE volume reductions in open-batch experiments, and c) TCE volume reductions in closed-batch experiments.
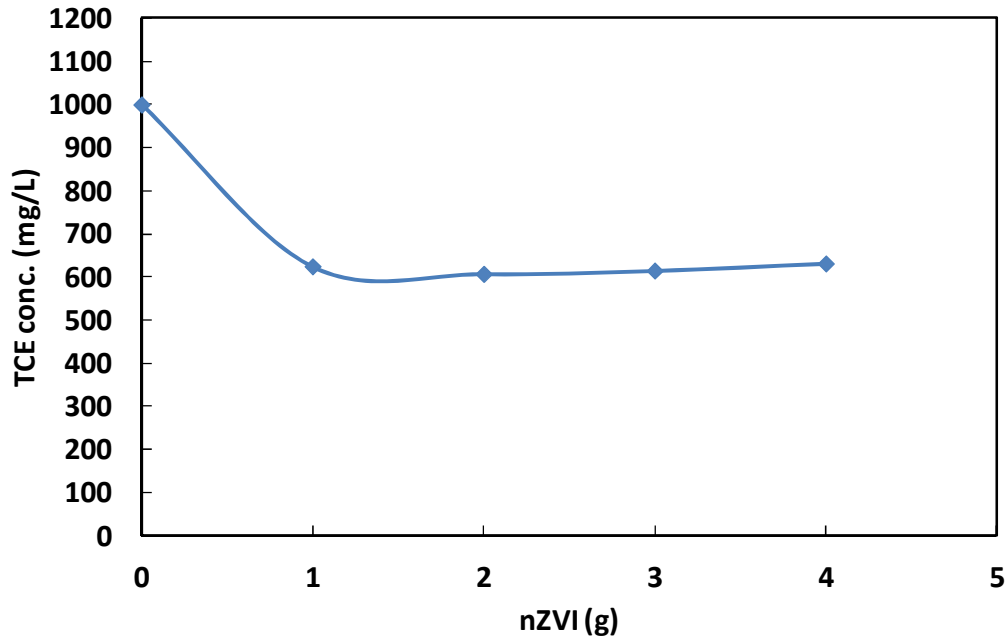
Figure 4.7. TCE concentration in aqueous phase for various amounts of nZVI experiments.

0.2 mL liquid TCE mixed with nZVI batch experiments were set up to determine the mass balance and the partitioning of TCE in each phase. Mass balance of each experiment was calculated by the following equation (Eq. 4.7):

$$M_{TCE\text{-}total} = M_G + M_S + M_Z + M_{lost} + M_P \qquad (4.7)$$

Where $M_{TCE\text{-}total}$ is total mass of TCE input to exp. (mg), M_G is mass of TCE in gas phase (mg), M_S is mass of TCE in aqueous phase (mg), M_Z is mass of TCE absorbed in nZVI sludge (mg), M_{lost} represents the absence of TCE mass from the experimental system, and M_P is mass of pure phase TCE in system (equal to 0 in all cases). Total mass of TCE was measured for accuracy in calculation even

81

though exact volume of TCE was fixed in each experiment. Head space gas sample in each batch was taken by using a 25 µL gastight syringe after 1 day reaction and TCE concentration in gas phase was detected by GC. Mass of TCE in gas phase was calculated by multiplying TCE concentration in gas phase with the volume of head space in each batch. The mixing samples after reaction were centrifuged at 6,000 rpm for 30 minutes to separate the solid sludge from the aqueous solution. TCE in aqueous solution was measured by pentane extraction method and GC. Mass of TCE in aqueous phase was calculated by multiplying TCE concentration in aqueous phase with the volume of water in each batch. The weight of the separated solid nZVI sludge was measured and small amount of the sludge (measured weight) was put into 5 mL vial and 2 mL of water and 2 mL of pentane was added into the vial. The vial was horizontally shaken at 250 rpm for 45 minutes. The upper pentane sample was taken by a 10 µL gastight syringe for TCE mass detected by GC. Mass of TCE absorbed in nZVI sludge was calculated by multiplying TCE concentration in nZVI sludge with the mass of nZVI sludge in each batch. Mass of TCE that is disappeared from the system is calculated by the mass balance equation (Eq. 4.7). The distributions of TCE in each phase for non nZVI, 1 and 3 g nZVI experiments are presented in Figure 4.8.
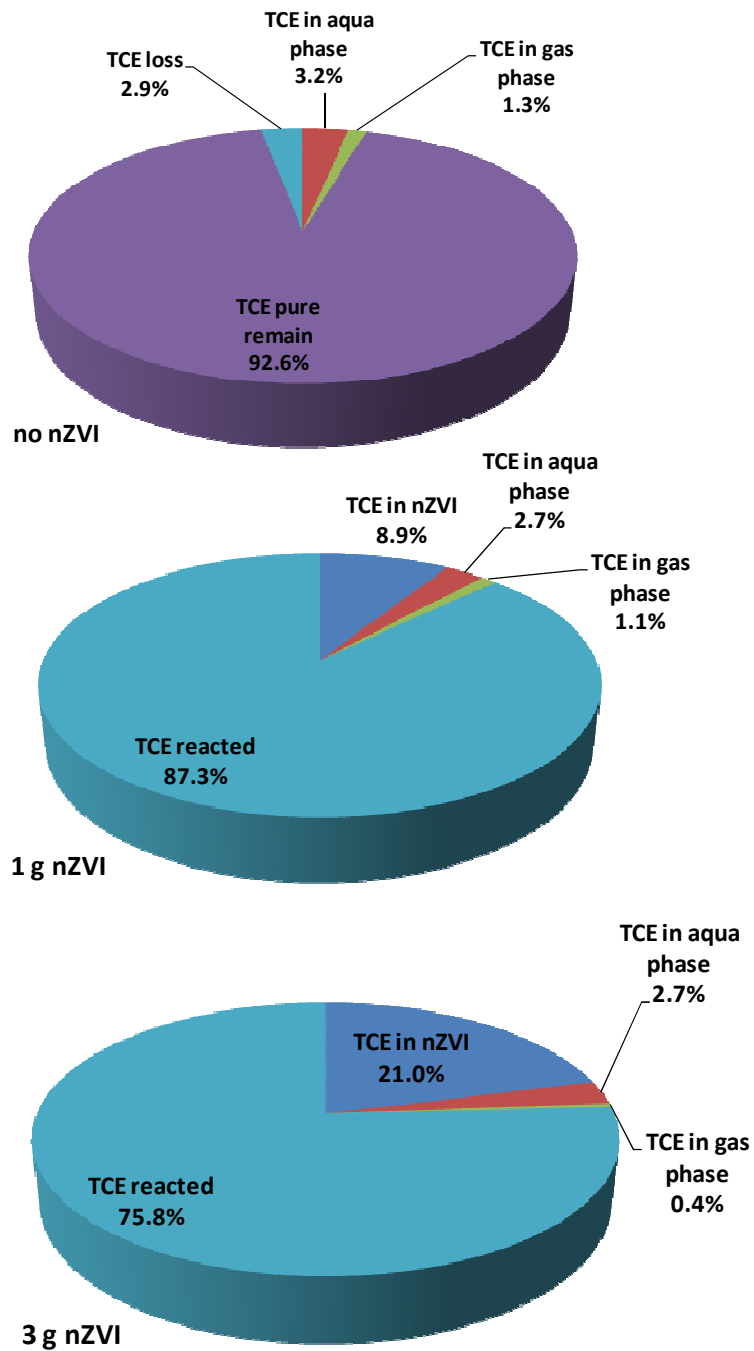
Figure 4.8. The distributions of TCE in each phase for non nZVI, 1 and 3 g nZVI experiments.

The distribution of TCE for non nZVI experiment shows that only 2.9% of TCE mass has lost from the system and 92.6% remains in TCE liquid phase

(Figure 4.8). Only 4.5 % of TCE transfers to water and air. For 1 g nZVI sample, 87.3 % of TCE mass has lost from the system, no TCE liquid remains. 3.8 % of TCE transfers to water and air. There is 8.9 % of TCE absorbed in nZVI sludge. For 3 g nZVI sample, 75.8 % of TCE mass has lost from the system, no TCE liquid remains. 3.1 % of TCE transfers to water and air. However, there is 21 % of TCE absorbed in nZVI sludge. After subtracting TCE mass lost in both 1 g and 3 g nZVI samples with TCE mass lost in non nZVI sample, 84.4 % and 72.9% TCE mass are expected to be reacted by nZVI in 1 g and 3 g nZVI, respectively. This reaction percentages show the lower reaction rate in high amount of nZVI samples as similar to the results mentioned previously. High amount of nZVI in limiting space decreases its specific surface areas resulting in lower reaction rate. Moreover, mass balance results show that there is some TCE mass absorbed in nZVI sludge. These indicate that absorption is one activity in TCE removal by nZVI. Higher TCE mass absorption in 3 g nZVI experiment reveals that more TCE mass is trapped in nZVI mass and not reacted. However, based upon the results, specific percentages of TCE mass absorbed in nZVI sludge are 8.9 % and 7 % of TCE mass per g of nZVI in 1 g and 3 g nZVI samples, respectively. Low specific absorption at high amount of nZVI might due to the low volume space of the system because of high density of nZVI. These low reaction rate and absorption in high amount of nZVI suggest that volume space may be a major factor influencing the TCE removal process by nZVI and this situation is usually found in underground contaminated sites.

Figure 4.9 presents TCE volume reduction by adding 1 g nZVI every 24 hours. The results show that 1.5 mL of TCE removed after adding 1 g nZVI every 24 hours for 3 days is higher than 1 mL TCE removed by the same 3 g of nZVI

added at the beginning of the experiment. 0.4 mL of TCE was found lost from non nZVI experiment. 0.8, 0.95, and 1.3 mL of TCE were removed by 1, 2 and 4 g nZVI, respectively. Pure TCE removed by adding 1 g nZVI every 24 hours is even higher than that of 4 g nZVI adding at the beginning. The linear relationship was found in the results with around 0.51 in slope and 0.99 in R-square. The slope of this relationship is higher than the slope of the ideal stoichiometrc reaction indicating that absorption is involved in this removal process. Adding nZVI every 24 hours can solve the problem of high density of nZVI in limited space and keep maintaining high surface areas of nZVI.

Based upon the results, nZVI shows the capability to treat pure phase TCE and byproducts of the reaction were detected indicating the removal processes composed of the reduction reaction of nZVI with TCE. The high specific TCE removal suggests that there are not only chemical reactions occurred in this TCE pure phase removal by nZVI, but also other mechanisms associated to the removal process. Adsorption found by mass balances is one of mechanisms responding to TCE pure phase removal process. However, the high density of nZVI decreases the absorption of TCE pure phase. The results of TCE concentration in aqueous phase indicate that concentration of TCE in aqueous does not reach to its saturation concentration due to the existence of nZVI in the system and TCE concentration is depended on the rate of TCE dechlorination. High density of nZVI reducing the available surface and lowering the rate of the reaction; consequently, increases the TCE concentration. However, nZVI can prevent TCE concentration in aqueous phase to reach its saturation concentration. Continuously adding small amount of nZVI gives the better results in improving TCE removal efficiency than adding high amount of nZVI at the beginning does.
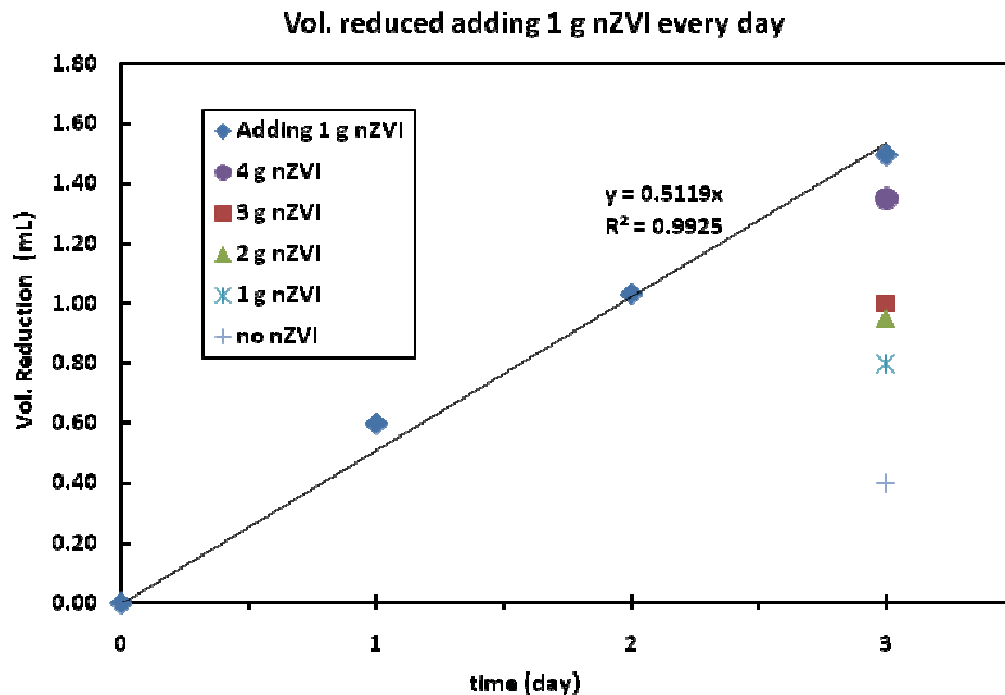
Figure 4.9. TCE volume reductions by adding 1 g nZVI every 24 hours.

4.4 Conclusions

In this study, nZVI has shown the good capability to remove TCE pure phase and the byproduct peak in GC head space result confirms the TCE dechlorination by nZVI. Not only TCE dechlorination reaction is conducted by nZVI, but TCE liquids also are absorbed into nZVI sludge. Mass balance results show that 7 – 9 % of TCE mass was trapped inside the nZVI sludge. These absorption of TCE in nZVI helps enhance the TCE removal efficiency. However, the accessibility to nZVI surface may be the important factor in the TCE removal process. The removal efficiency was dropped to 60% compared with stoichiometric reaction of TCE and nZVI when increasing amount of nZVI to higher than 1 g. High amount of nZVI in very limited space such as in subsurface environment,

86

decreases the available surface areas of nZVI corresponding to lower removal efficiency. The experimental results indicate that continuously injecting small amount on nZVI has better removal efficiency than that of high amount of nZVI injected initially.

CHAPTER 5

Enhanced Transport of Polyelectrolyte Stabilized Nanoscale Zero-Valent Iron (nZVI) in Porous Media

5.0 Abstract

Laboratory experiments including column and batch sedimentation studies were conducted to investigate the transport of nanoscale zero-valent iron (nZVI) particles stabilized by three polyelectrolytes: polyvinyl alcohol-co-vinyl acetate-co-itaconic acid (PV3A), poly(acrylic acid) (PAA) and soy proteins. Results of the continuous packed column study suggest that both PV3A and PAA can increase nZVI mobility by reducing particle size and generating negatively charged surfaces of nZVI. PV3A stabilized nZVI has the best transport performance among the three materials. It was found that approximately 100% of nZVI flowed through the column. Retardation of nZVI is observed in all tests. Due to the large surface area of nZVI, large amounts of polyelectrolytes are often needed. For example, soy proteins exhibited an excellent stabilization capability only at doses over 30% of nZVI mass. Approximately 57% of nZVI remained in the column when nZVI was stabilized with PAA at the dosage of 50%. Results suggest that nZVI may be prepared with tunable travel distance to form an iron reactive zone for the in situ remediation.

5.1 Introduction

Nanoscale zero-valent iron particles (nZVI) has been studied since mid-1990s and has increasingly been applied for environmental remediation and hazardous waste treatment have been studied since 2000 (Wang and Zhang 1997, Zhang 2003, Li et al. 2006a). The colloidal iron nanoparticles have large surface areas for rapid uptake and transformation of a large number of environmental contaminants. Reactions of nZVI with chlorinated aliphatic compounds containing either one or two carbon atoms have quickly become classical research literature. Numerous studies have found that nZVI can effectively degrade chlorinated solvents, organochlorine pesticides, PCBs, organic dyes, and inorganic pollutants such as perchlorate, nitrate, and heavy metal ions (Elliott et al. 2009, Xiong et al. 2007, Lien and Zhang 2007, Song and Carraway 2005, Kanel et al. 2005, Ponder et al. 2000, Li and Zhang 2006, Lowry and Johnson 2004, Su and Puls 2004).

In addition to its large surface area that provides abundant sites for surface reactions, a proved advantage of nZVI is the simple implementation for subsurface injection and potential for subsurface transport, which enables nZVI to clean up large area of contamination. In this manner, the time, cost and engineering problems associated with constructing conventional iron walls (permeable reactive barriers) can be minimized. Dozens of in situ applications have been reported so far (Elliott and Zhang 2001, Wei et al. 2010, He et al. 2010, Henn and Waddill 2006, Quinn et al. 2005). For successful subsurface injection, a stable suspension of nZVI in water is needed. That is, aggregation and sedimentation should be controlled so that transport of nZVI in groundwater can be maintained by Brownian diffusion and advection. Unfortunately, owing to the relatively high ionic strength of groundwater favorable for colloidal aggregation and the high

89

density of iron, bare nZVI without proper surface modification has very limited mobility in the subsurface. Laboratory studies have shown that nZVI typically exists as micron sized aggregates in water (Sun et al. 2006, Sun et al. 2007, Phenrat et al. 2007).

Dispersion of nZVI is more a skill of art than science at present time. It is likely that some of the most important factors affecting the aggregation and transport of nZVI are still to be identified. For example, the effects of magnetic forces and high solution pH on nZVI aggregation and filtration have not been examined. Based upon theories of colloidal aggregation in water, it has been generally assumed that nZVI suspension in water depends on the net effect of attractive and repulsive forces among nZVI particles. According to DLVO theory (named after Derjaguin and Landau, Verwey and Overbeek), the overall stability of a colloidal system is determined by the sum of van der Waals attraction and electrostatic double layer repulsion (Stumm and Morgan 1996). The DLVO theory predicts that an energy barrier exists, which prevents the aggregation of some colloidal particles. Compared to micro sized colloids, evidence suggests that nanoparticles have stronger tendency to aggregation/coagulation. This has been attributed to smaller particle size and reduced surface potential.

To create and maintain stable suspension of nZVI particles, a common strategy is to increase the repulsive electrostatic forces. Several studies have reported that the certain polymeric materials are able to stabilize nZVI in water. A wide array of polymers has been investigated including poly acrylic acid (PAA), polyvinyl alcohol-co-vinyl acetate-co-itaconic acid (PV3A), polyaspartate (PAP), Tween 20 and biopolymer such as soy proteins, starch, and carboxymethyl cellulose (CMC) (Schrick et al. 2004, He and Zhao 2005, Phenrat et al. 2008,

Tiraferri et al. 2008, Kim et al. 2009, Saleh et al. 2007, Saleh et al. 2008). Among them, PAA is the first polymer used to disperse nZVI for the field remediation while CMC has recently been tested in the field (He et al. 2010). In general, the polymers consists of polar anchoring groups (e.g., -COOH, -OH, -C=O) and a stabilizing hydrocarbon chains. The anchoring groups can chemically or physically attach onto the surface of nZVI while the stabilizing chains in water can waggle around and take up varied configurations. Overlap of these flexible chains associated with the neighboring particles produces electrostatic and steric repulsions between particles and can thus stabilize the particles under certain conditions (Everett 1989). Our previous work has demonstrated that PV3A provides great electro-steric stabilization for nZVI (Sun et al. 2006, Sun et al. 2007). As illustrated in Figure 5.1, in the absence of PV3A, bare nZVI, has a particle size of about 100 nm that is apparently a loose aggregate of numerous primary ZVI nanoparticles with the size less than 10 nm (Sun et al. 2007). Bare nZVI aggregates and precipitates in a few min. With the addition of PV3A, nZVI with the size of about 15 nm can exist in water for months (Li et al. 2006b). Not surprisingly, the PV3A stabilized nZVI moves swiftly in laboratory soil columns.

91
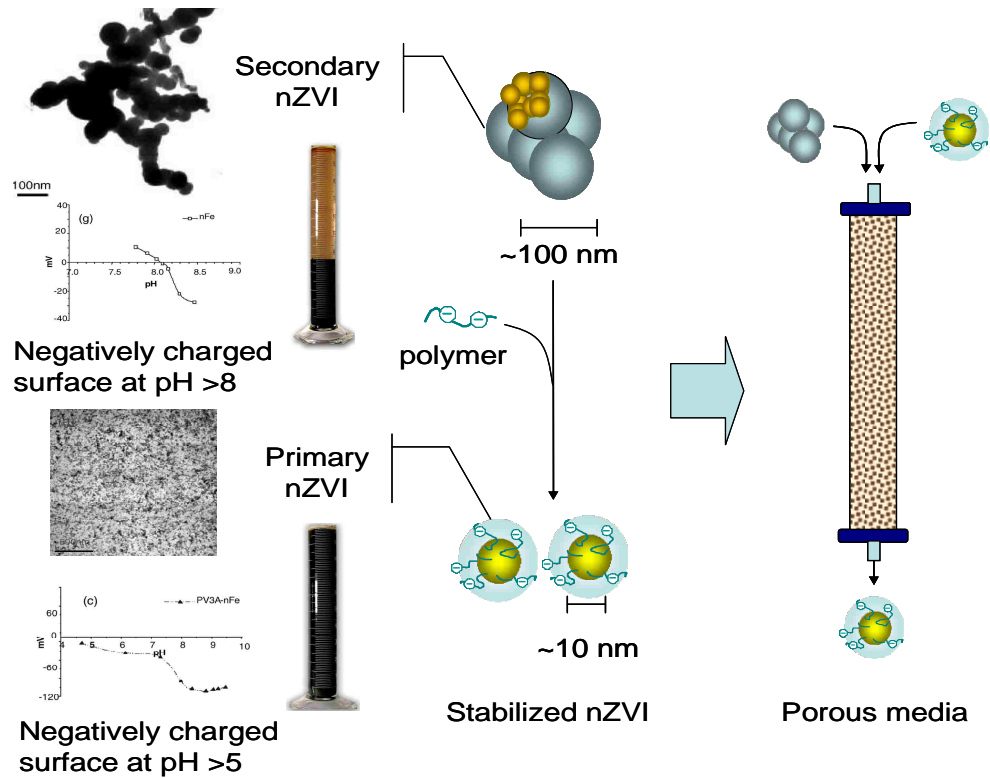
Figure 5.1. Concepts of nZVI stability and transportability.

The electro-steric stabilization is a common method that has been used to improve the mobilization of particles in solution by adding ionic polymeric molecules such as polyelectrolytes (Morrison and Ross 2002). The polyelectrolytes containing a net negative or positive charge at near neutral pH not only sterically stabilize particles but also increase surface charges of particles that prevent particles from the aggregation and reduce size of particle clusters. As illustrated in Figure 5.1, the surface zeta potential of PV3A stabilized nZVI is negative within a wide range of pH (>5) while the surface of bare nZVI is negatively charged only when pH is greater than 8. Thus, during the particle transport, the electrostatic repulsive force induced by the polyelectrolyte not only stabilizes nanoparticles

www.manaraa.com

themselves but also prevents nanoparticles from precipitation at the surface of porous media, which is negatively charged.

Though extensive studies have been conducted to investigate the nZVI stabilization and transport in porous media, the particle concentrations were relatively low (0.1-6 g/L) (Yang et al. 2007, Kanel et al. 2007, Phenrat et al. 2010, Raychoudhury et al. 2010). The use of low particle concentrations is because nZVI tends to agglomerate at high particle concentrations even in the presence of polymers (Phenrat et al. 2010). However, our field experience suggests that the injection concentration of nZVI should be greater than 8-10 g/L in order to establish an effective remediation in the aquifer. Thus, the objective of this chapter is to develop a polymer stabilized nZVI that can be used at high injection concentration (10 g/L). Nearly 20 polymers have been screened for the stabilization of nZVI in aqueous solution (Table 5.1). In addition, several biomaterials have also been examined including starch and soy proteins. In this work, results on the effects of PV3A, PAA and soy proteins are presented. Bath sedimentation experiments and continuous packed column studies were conducted to investigate the nZVI stabilization and the transport behavior of the stabilized nZVI particles. To the best of our knowledge, the concentration of polymer stabilized nZVI used in this chapter to simulate the field conditions is the highest dose applied in column studies so far.

Table 5.1. Commonly used polymers for sterically stabilized aqueous dispersions.

Anchoring Groups	Stabilizing Chains
Polystyrene	Polyethylene oxide
Polyvinyl acetate	Polyvinyl alcohol
Polymethyl methacrylate	Polyacrylic acid
Polyacrylonitrile	Polymethacrylic acid
Polydimethylsiloxane	Polyacrylamide
Polyvinyl chloride	Polyvinyl pyrrolidone
Polyethylene	Polyethylene imine
Polypropylene	Polyvinyl methyl ether
Polylauryl methacrylate	Poly(4-vinyl pyridine)
Polypropylene oxide	

5.2 Materials and Methods

5.2.1 Materials

ACS grade ferric chloride ($FeCl_3$) was purchased from Alfa Aesar. Sodium borohydride ($NaBH_4$) with 98% purity was obtained from Finnish chemicals (Finland). Polyvinyl alcohol-co-vinyl acetate-co-itaconic acid (PV3A) and sodium bromide (NaBr) were from Aldrich. Polyacrylic acid (PAA), sodium salt with molecular weight ranging from 4,300 to 4,400 g/mol and 40 wt% solution was purchased from Polysciences, Inc. Standard Ottawa sand, designated as ASTM 20/30 was from U.S. Silica Company. Hydrochloric acid (12.1 N) and nitric acid (15.8 N) were purchased from EMD Chemicals and Fisher Chemicals,

94

respectively. Soy proteins (Gold 300 soy powder, 300 mesh) with 40% protein and 20% fat were obtained from SoyLink[TM], Iowa.

5.2.2 Synthesis of nZVI

nZVI used in this work was prepared with the reduction of ferric chloride by sodium borohydride. Equal volumes of 0.94 M $NaBH_4$ and 0.18 M $FeCl_3$ were quickly mixed in a batch reactor. The borohydride was slowly metered into the ferric chloride solution stirred at ~400 rpm. The redox reaction can be formulated as follows:

$$4Fe^{3+}_{(aq)} + 3BH_4^-_{(aq)} + 9H_2O \rightarrow 4Fe^0_{(s)} + 3H_2BO_3^-_{(aq)} + 12H^+_{(aq)} + 6H_{2(g)} \quad (5.1)$$
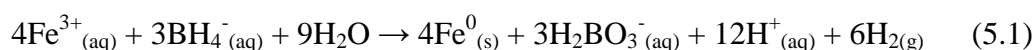
Additional 10 min were given to complete the reaction after the titration was completed. The formed iron nanoparticles were harvested by vacuum filtration through 0.2 µm filter papers. The iron particles were then washed several times with DI water and ethanol before use. The average particle diameter of nZVI was around 60-70 nm, as determined by scanning electron microscopy and a combined acoustic/electroacoustic spectrometer (Sun et al. 2007). Detailed procedures on the nZVI synthesis and characterization have been previously published (Sun et al. 2006, Sun et al. 2007). The finished nanoparticles were washed with ethanol, purged with nitrogen, and refrigerated in a sealed polyethylene container under ethanol (<5%) until use. The residual water content of the nanoparticles as used typically varied between 60-70%.

5.2.3 Synthesis of polymer stabilized nZVI

PV3A, PAA and soy powder were used in this work to prepare aqueous suspensions of nZVI. Figure 5.2 illustrates the molecular structure of PV3A, PAA and soy proteins. PV3A, with molecular weights in the range of 4300-4400 is a food grade material, biodegradable and nontoxic, likely due to the presence of highly biodegradable –OH, –CO–, and –COOH groups in the molecules (Sun et al. 2007). PAA with molecular formula $[CH_2CH(CO_2Na)]_n$ contains carboxylic acid (-COOH) groups for stabilizing nZVI. In an alkaline solution, carboxylate is assumed to be the anchors coordinating onto the iron surface (Harris et al. 2003, Wu et al. 2004) and thus provide iron particles with additional charges. Monomers of natural soy proteins have amino acid residues linked by amide bonds to form polypeptide chains (Fig. 5.2) (Wool and Sun 2005). The polypeptide chains can interact with each other and entangle into complicated three-dimensional structures by disulfide and hydrogen bonds with a molecular weight ranging from 300,000 to 600,000 Da. Soy proteins can be divided into water-soluble albumins and salt solution-soluble globulins. Most soy proteins are globulins, containing about 25% acidic amino acids, 20% basic amino acids, and 20% hydrophobic amino acids (Wool and Sun 2005).

96
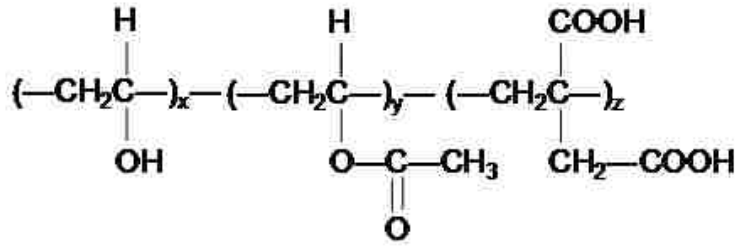
a) Polyvinyl alcohol-co-vinyl acetate-co-itaconic acid (PV3A)
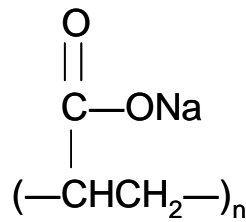
b) Poly acrylic acid (PAA)
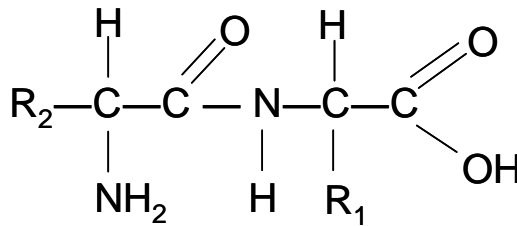
c) Soy proteins: An example of representative molecular structure

Figure 5.2. Molecular structures of (a) polyvinyl alcohol-co-vinyl acetate-co-itaconic acid (PV3A), (b) poly acrylic acid (PAA), and (c) soy proteins.

PV3A stabilized nZVI was prepared in a 500 mL flask reactor with three open necks. The center neck hosted a mechanical stirrer with a speed set at 60 rpm. 2 g/L of nZVI particles was added with PV3A with the mass ratio of PV3A to nZVI from 0.05 to 0.1. In other words, the dose of PV3A accounted for 5-10% of

97

nZVI mass. The solution was mixed for 2 h at pH 9.5-10 under ambient temperature conditions (23 ± 0.5 ºC). Similar procedures were also conducted for synthesizing the PAA and soy proteins stabilized nZVI. During each experiment, suspended solids, suspended iron, solution pH and Eh were measured while nZVI was characterized using transmission electron microscopy (TEM).

5.2.4   Stability test of nZVI

Batch sedimentation experiments were conducted to assess stability of nZVI dispersion. A 200 mL suspension of 10 g/L nZVI and polyelectrolytes were mixed for 2 h. To investigate the polyelectrolyte dose effect, the mass ratio of polyelectrolyte to iron was set in the range of 0 to 1. The suspension was mixed at a speed of 500 rpm at room temperature. Afterward, the solutions were transferred into 100 mL cylinders to observe the sedimentation of nZVI for 180 min. Before the experiment, iron samples were taken to measure the total iron concentration and pH of each solution. Total solids and iron concentration in solutions after settling were also measured.

5.2.5   nZVI transport experiment

Figure 5.3 illustrates the setup of column experiments. Glass columns with 30 cm in length and 2.5 cm in diameter were packed with sand for the nZVI transport experiments. Standard Ottawa sand, designated as ASTM 20/30 (American Society for Testing and Materials) was used as the column media. The ASTM 20/30 sand is composed of mineral quartz (>99.8%, silicon dioxide, SiO_2).

98

Its color is white, the specific density is 2.65 g/cm^3, and the grain shape is closely rounded. The particle size is in the range of 0.60-0.85 mm. Main parameters of the column experiments are summarized in Table 5.2. A few glass beads of 3 mm diameter were placed at both ends of the column to prevent the loss of the sand and facilitate the flow distribution. The column was set up vertically and sealed with screw caps at both ends.
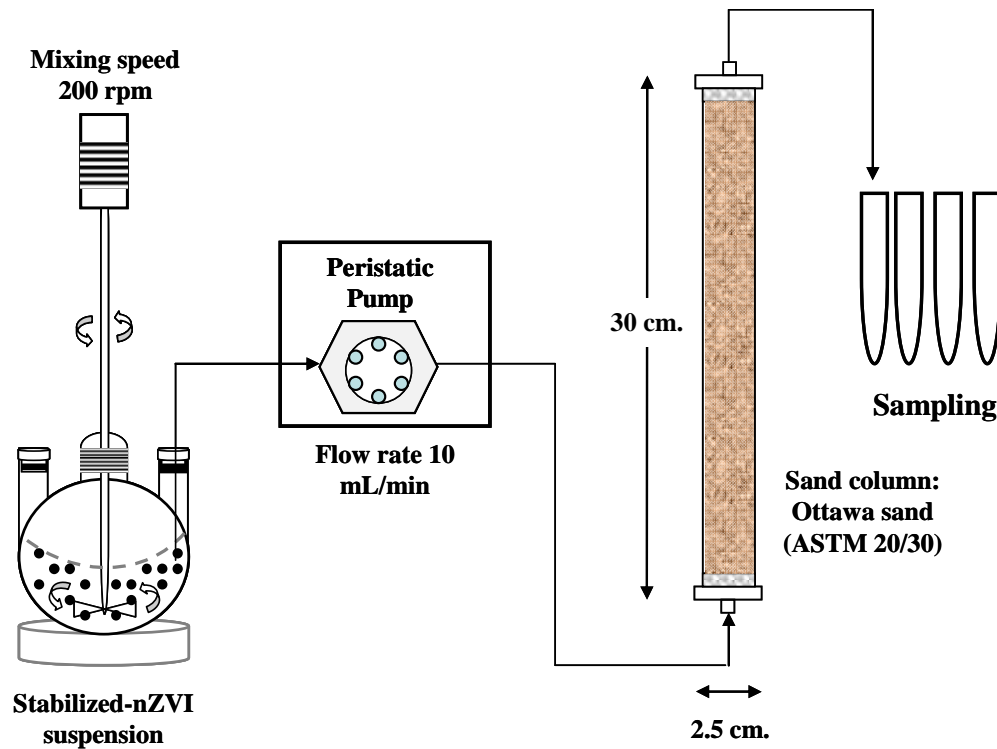
Figure 5.3. Schematic of column experiments.

Table 5.2. Parameters of sand columns for nZVI transport experiments.

	Bare-nZVI	PV3A-nZVI	PAA-nZVI
Flow rate (mL/min), Q	10.0	3.0	10.0
Bed volume (mL), BV	58.9	58.9	58.9
Porosity (θ)	0.4	0.4	0.4
Grain size (mm)	0.6-0.85	0.6-0.85	0.6-0.85
Column Length (cm), L	30	30	30
Column inner diameter (cm), D_i	2.5	2.5	2.5
Darcy velocity (cm/s), V_d	0.034	0.01	0.034

For the transport of PAA stabilized nZVI, a 200 mL solution containing PAA stabilized nZVI was pumped upward through the column as illustrated in Fig. 5.3. The flow rate was approximately 10 mL/min measured at the effluent port of the column. After completing the injection at 3.4 pore volumes (PV), 700 mL DI water was introduced into the column to flush the remaining particles inside the column. To prevent the nZVI from the sedimentation, the suspension was mixed at 50 rpm. The iron concentration measured in the influent was about 10 g/L. For the transport of PV3A stabilized nZVI, a concentration of 2 g/L of PV3A stabilized nZVI was tested in the experiments. It should be pointed out that the injection concentration of PV3A-stabilized nZVI used in this work follows the concentration of nZVI used in the field work (Zhang 2003). As shown in Fig. 5.3, the inflow was connected to the flask reactor where the nZVI was mixed at 50 rpm to maintain the

suspension. The flow rate (~3 mL/min) was determined at the effluent port of the column. The effluent stream was collected by a fraction collector at selected time intervals. The solid content and iron concentration of effluent samples were determined. The transport of bare nZVI was also conducted as control tests. The operating conditions are listed in Table 5.2.

Bromide (Br^-) is commonly used as the non-adsorbing and non-retarded tracer in column experiments (Bedient et al. 1999). In this work, bromide in the form of sodium bromide (NaBr) was dissolved in DI water with a concentration of 0.5 mM. The tracer was continuously pumped into the column till the effluent concentration is equal to the influent. The effluent bromide was collected at a selected time interval and the concentration was determined by an Ion Chromatography (IC) (ICS-90, Dionex), which was equipped with an analytical column (IonPac®AS4A-SC 4×250 mm, Dionex) and a detector (Model DS5 Detection Stabilizer, Dionex) for anion analysis. The results were used to determine porosity of the sand column and retardation of nZVI transport.

5.2.6   Analytical methods

Transmission electron microscopy (TEM): Images of nZVI were recorded with a Philips EM 400T TEM (Philips Electronics Co., Eindhoven, Netherlands) operated at 100 kV. The TEM samples were prepared by depositing two to three droplets of the sample suspension onto a holey carbon film (Ernest Fullam, Inc., Latham, NY), which was completely dried in a fume hood prior to the TEM analysis.

101

Total solid concentration: Evaporation method was used to measure the solids content of a solution. 5 mL of nZVI sample was poured into 100 mm diameter-weighing pan and dried at 105°C for 24 h. Afterward, the weight of the sample pan was measured and the solid concentration was determined.

Total iron concentration: Atomic absorption (AA) method was used to measure the iron concentration in solution samples. 1 mL nZVI suspension was first transferred into a 100 mL volumetric flask and mixed with 50 mL of 2.4 N of HCl and 0.27 N of HNO_3. The solution was mixed for 1 h. DI water was then added to make up the solution to 100 mL. The solution was then diluted for AA analysis. A Perkin Elmer AAnalyst 200 Atomic Absorption Spectrometer was used in this work.

pH/Standard Potential (E_h) measurement: A combination pH electrode (Orion) was used in conjunction with a Sension1 (Hach) meter to track solution pH. It was calibrated prior to each test. A combination Ag/AgCl reference electrode (Cole-Parmer) was used with a Model 420A pH/ORP meter (Orion) to monitor redox potential and was calibrated with fresh ZoBell solution before each test. Measured redox potential readings (mV) were converted to E_h, the potential relative to the standard hydrogen electrode, as a function of solution temperature by adding +199 mV at 25°C.

5.3 Results and Discussion

Figure 5.4 contains main characteristics of the polyelectrolyte stabilized nZVI in the sand column. Photographs of the columns after the injection of bare nZVI

102

are presented for comparison. For the bare nZVI in the absence of the electrolytes (Fig 5.4a), most of nZVI deposited at the bottom section (the entrance end) of the column. No visible black iron can be seen in the effluent end. Fig. 5.4(b) and (c) are photos of the PV3A stabilized nZVI. Black nZVI quickly moved up in the column, and quickly filled up the entire column. The black color nZVI was clearly visible in the effluent with gradually increasing concentration during the period of 3 pore volumes (PV) injection (Fig. 5.4(d)). After the influent was switched to pure water, the PV3A stabilized nZVI can be completely flushed out of the column with about three pore volumes of DI water, suggesting a low sticking probability of the PV3A stabilized nZVI (Fig. 5.4(c)).

103
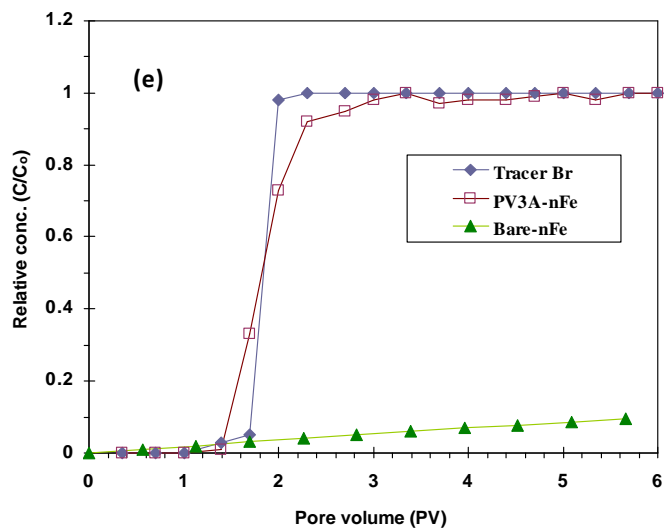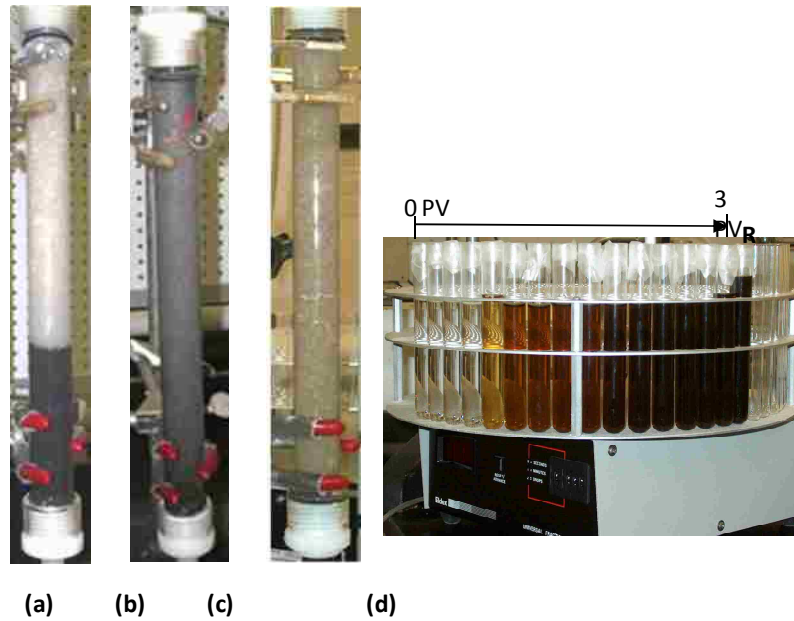
Figure 5.4. Main characteristics of the polyelectrolyte stabilized nZVI in the sand column. (a) Photograph of the column after bare nZVI injected. (b) Photograph of the column after the complete injection of PV3A stabilized nZVI and (c) flushed by DI water. (d) The collection of the effluent containing PV3A stabilized nZVI (the tube labeled R is the initial stabilized nZVI slurry for comparison). (e) Breakthrough curves of the column experiment for PV3A stabilized nZVI and bare-nZVI.

104

Figure 5.4(e) presents the breakthrough curves of column experiments for PV3A stabilized nZVI and bare nZVI. A tracer (bromide) was used for control and baseline measurements. For the PV3A stabilized nZVI, iron concentration in the effluent reached the same level as that in the influent ($C/C_0 = 1$), suggesting completely breakthrough. The break point at $C/C_0 = 0.95$ is around 2 PV, compared to 1.5 PV of the tracer. This shows that the retardation effect is small for the transport of PV3A stabilized nZVI in the column. In contrast, the relative concentration (C/C_0) in the effluent for the bare-nZVI is no more than 0.15 over 6 PV, suggesting most of the bare nZVI was retained in the column. As confirmed in our previous work, PV3A reduces the size of nZVI and moreover, creates highly negative-charged surfaces (Sun et al. 2007). Both the steric repulsion caused by the large PV3A molecules and electrostatic repulsion created by the dissociation of the carboxylic acid groups on the PV3A molecules are likely in play and favor nZVI particles move through the sand column.

The data presented in Fig. 5.4(e) can be further used to calculate the dimensionless attachment efficiency factor (α) for nZVI transport (Tufenkji and Elimelech 2004):

$$\alpha = -\frac{2}{3}\frac{d_c}{(1-\theta)L\eta_o}\ln\left(\frac{C}{C_0}\right) \tag{5.2}$$

where d_c is the diameter of single spherical collector, θ is the porosity of the medium, L is the filter medium packed length, (C/C_0) is the normalized particle concentration obtained from the breakthrough curve, and η_0 is the predicted clean

bed single-collector efficiency. Values of various parameters are summarized in Table 5.2 and η_0 is estimated according to the work of Tufenkji and Elimelech (Tufenkji and Elimelech 2004). Hence, the PV3A stabilized nZVI has the attachment efficiency factor of about 4.7×10^{-4} at $C/C_0 = 0.99$. The attachment efficiency factor of 4.7×10^{-4} may match the low-end value of natural colloids (with α typically less than 0.05). In other words, the stabilized nZVI is indeed stable in water compared to naturally occurring colloidal particles.

The transport of PAA stabilized nZVI was also examined with the same column experiments (Fig. 5.5). Preliminary tests showed that PAA is less effective than PV3A so the PAA to iron ratio was increased to 0.5. Total iron passing through the column was measured as a function of pore volume as shown in Fig. 5.5. nZVI gradually moved from the bottom to the top of the column. The column color changed from brown to black (Fig. 5.5(a), (b), (c) and (d)). The highest iron content in the effluent was determined to be 45% of the influent iron level at 2.8 PV. After completing the injection of nZVI at 3.4 PV, DI water was pumped into the column to flush the nZVI deposited in the column. As the particles were washed out, the column gradually turned to brown (Fig. 5.5(e), (f) and (g)). There was a small peak appearing at 4.5 PV. The split peak may be attributed to some large nZVI that migrated slowly in the column and was flushed out by DI water. In other words, the particles have a range of sizes.
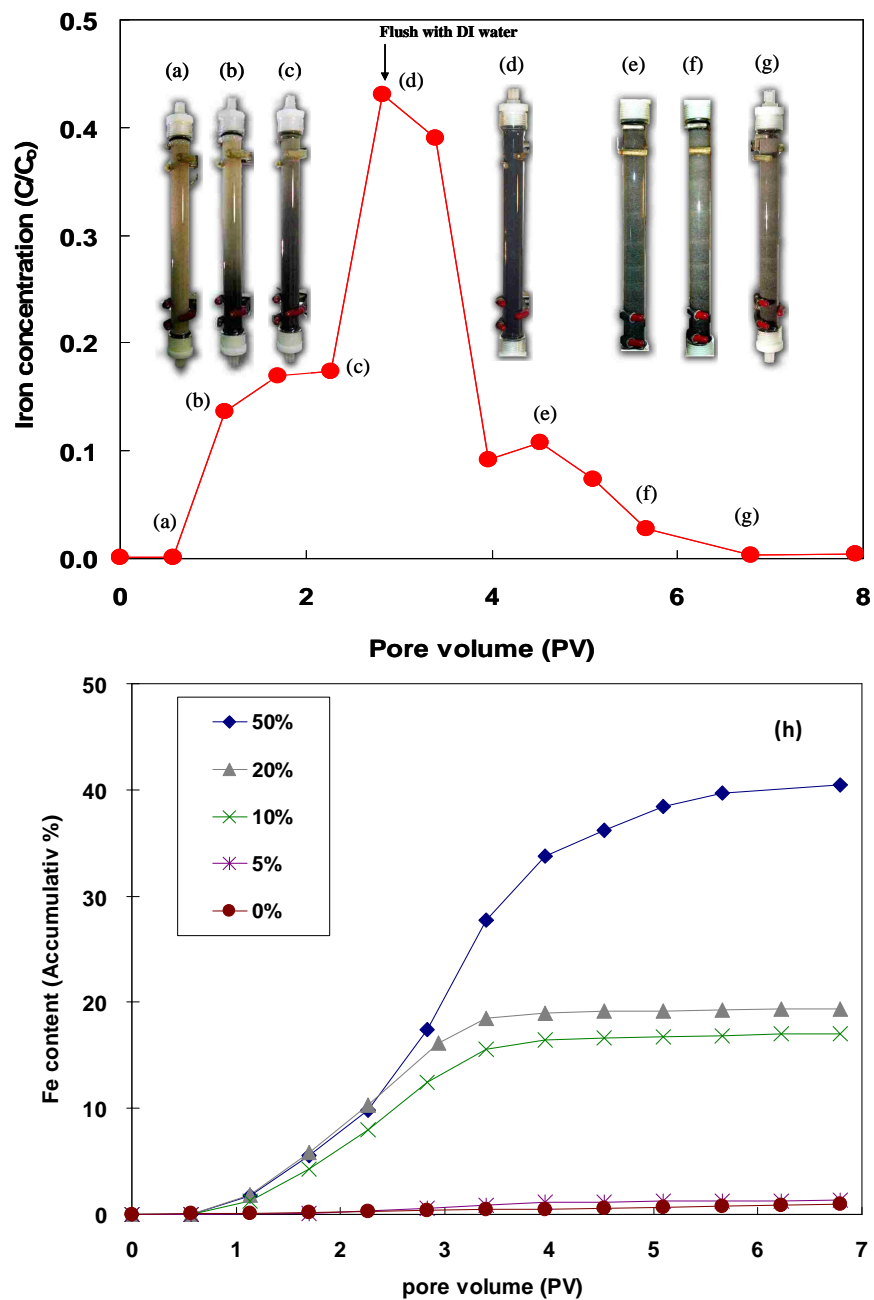
Figure 5.5. The breakthrough curve of the column experiment for PAA stabilized nZVI at the PAA dosage of 50%. Photographs of the column labeled from (a) to (g) were taken during the nZVI transport corresponding to the specific sampling time shown in the breakthrough curve. (h) The accumulative curve of iron in the effluent during the course of PAA stabilized nZVI transport in the column. The PAA dosage varies from 0 to 50%.

Unlike the PV3A stabilized nZVI, PAA stabilized nZVI exhibited significant retardation effect. Fig. 5.5(h) depicts the accumulative iron mass in the effluent as a function of influent PV. For the test of bare nZVI, the results show that less than 1% of iron came out from the column over the experiment duration. Similarly, at the low PAA dosage (5%), only a small amount of iron was ever detected in the effluent. Increase in the PAA dosage did increase in the iron transport out of the column. For example, about 18% of the total iron was obtained in the effluent when the PAA dosage increased to 10%. The total iron mass recovered in the effluent accounted for nearly 43% of the initial iron mass when the PAA dosage was increased to 50%. Though Kanel et al. reported PAA-stabilized nZVI (4 g/L) can be transported like a tracer without significant retardation in a two dimensional sand box (Kanel et al. 2008), the retardation was still observed in one dimensional packed sand column at the particle concentration greater than 0.5 g/L (Raychoudhury et al. 2010). Obviously, PAA and PV3A have different molecular size and charge density, which in turn affect the overall stability of nZVI in water.

Transportability of nanoparticles in the porous media is mainly dependent on the particle size, stability of the suspension and particle charge. Earlier studies on turbidity penetration in the aquifer have indicated that natural colloidal particles particularly those about 0.1 – 1 μm in diameter can penetrate in the porous media for an appreciable distance (Kanti Sen and Khilar 2006). As shown in Fig. 5.6, bare nZVI without stabilizers aggregates and forms chain-like clusters, though the primary iron nanoparticles may have the size of 1-10 nm in diameter. With the addition of polyelectrolyte stabilizers, a more stable suspension of nZVI can be attained. Figure 5.6 also shows the TEM images of nZVI particles stabilized with

various dosage of PAA. For the PAA dosage of 20 and 50%, the TEM images show that PAA serves an agent preventing nZVI from the aggregation (Fig. 5.6(b) and (c)). However, with the PAA dosage at 100%, the chain-like clusters of nZVI were reemerged. The clusters formed at high PAA dose show looser structure than bare nZVI cluster structures. The chain-like clusters that are a consequence of weak attractive forces have been reported in extensive studies of bare nZVI (e.g.,(Lien et al. 2007)). The gel-like network of PAA bridges nZVI particles when excessive amount of PAA is used (Lin et al. 2010).
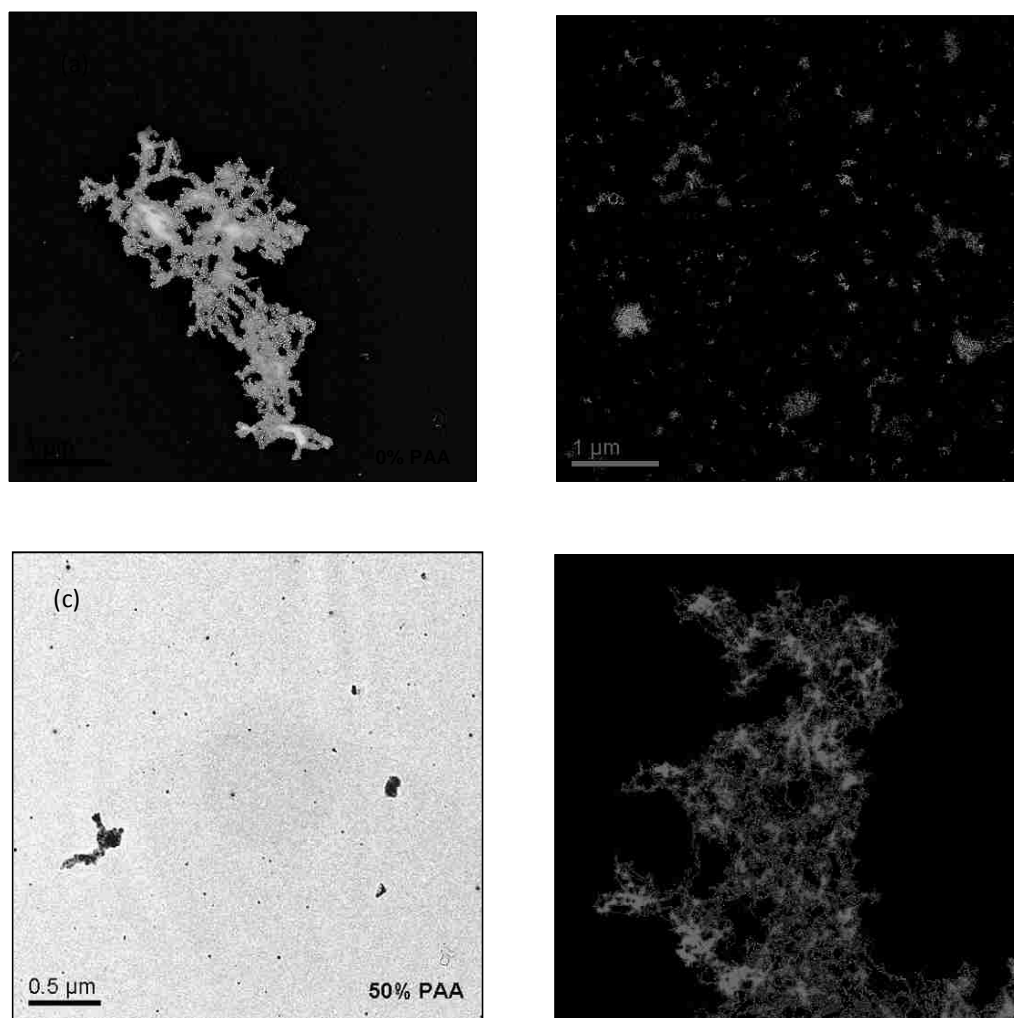
Figure 5.6. TEM images of nZVI stabilized with various PAA dosage: (a) 0%, (b) 20% (c) 50% and (d) 100%.

Stability of nZVI suspensions was further tested by sedimentation experiments. Without polyelectrolytes, bare nZVI settled in a few min. Figure 5.7 shows the total solid concentration of stabilized nZVI solution after settling for 180 min. At the low PAA dosage (<5%), the solutions have low solid content and the upper liquid is clear because most of nZVI was aggregated and settled. The solid content accounted for less than 5% of the total iron mass. The total solid concentration and the total iron concentration analyzed by AA are well correlated because the nZVI is the only solid in the system. The solid concentration in solution rapidly increased to 22% at PAA dosage of 10% and continuously increased to 43% at PAA dosage of 50%. A slow increase in the solid content to 45% was observed at the PAA dosage of 100%. It is apparent that the nZVI stability is a function of the PAA dosage. Increase in the PAA dosage resulted in the enhancement of the nZVI stability. However, an excessive amount of PAA was not beneficial to the suspension of nZVI. This is consistent with the TEM analysis shown in Fig. 6. Similar to the PAA, the soy proteins are also capable of stabilizing nZVI in the solution. As depicted in Fig. 5.7, nearly 100% of nZVI was suspended in the solution at the soy protein dosage at 30%. However, the stability decreased when the soy protein dosage exceeded 30% of the total iron mass, suggesting the overdose undermined nZVI stabilization.

110
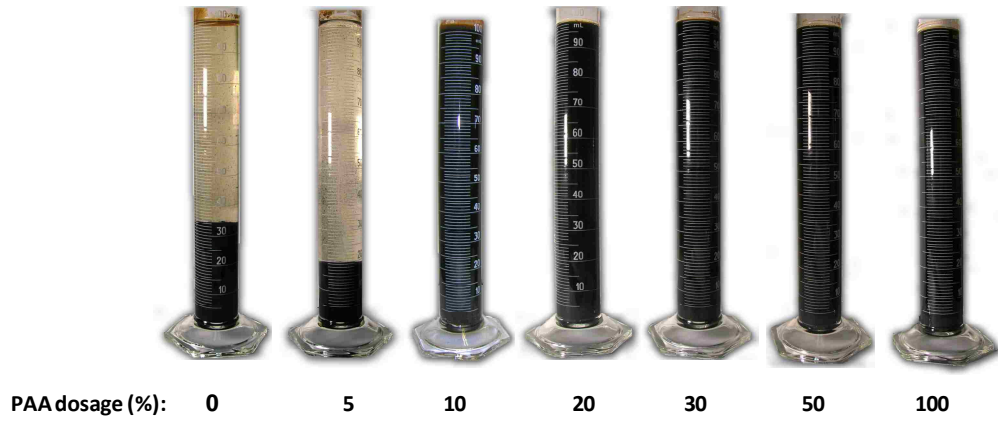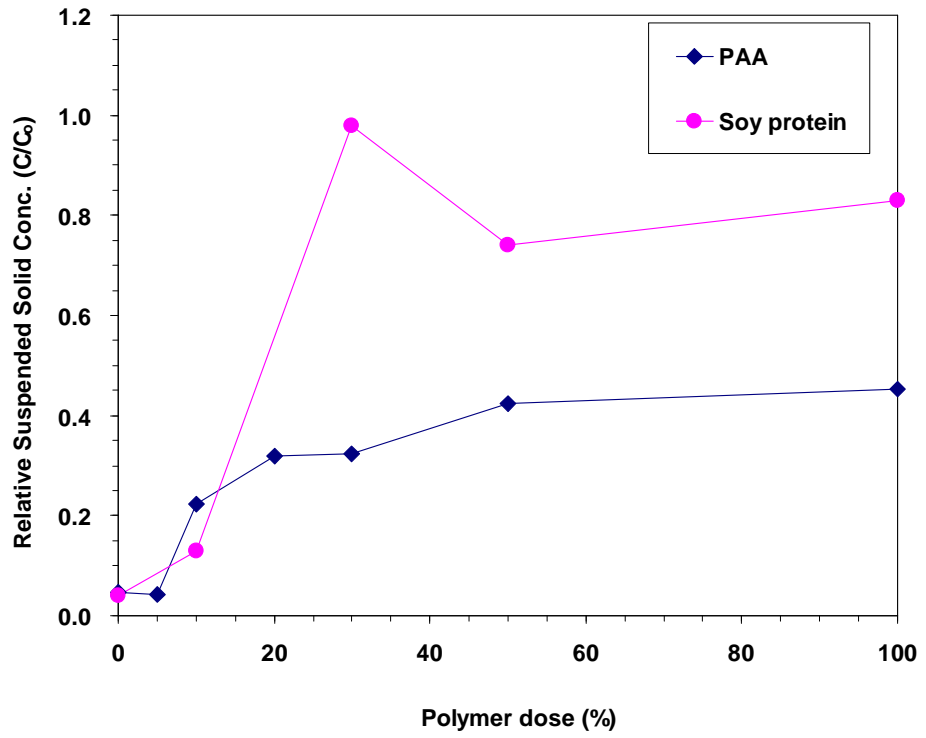
Figure 5.7. Effect of the dosage of PAA and soy protein on the dispersion of nZVI after settling for 180 min.

In general, aquifer materials are negatively charged; thus, a negatively charged surface of particles would be favorable for particle transport. The zero-point of charge (pH_{zpc}) has been determined to be 8.1 for bare nZVI (Sun et al. 2006, Sun et al. 2007). In other words, the nZVI surface is negatively charged at pH greater than 8.1. At near neutral pH, bare nZVI has positive charges, which are detrimental to nZVI transport due to the rapid attachment to aquifer materials. On the other hand, both PAA and PV3A stabilized nZVI showed a relatively low value of pH_{zpc}. For example, the addition of PV3A significantly converted nZVI to a negatively charge over a wide pH range. The pH_{zpc} of PV3A stabilized nZVI was measured to be about 4.7. Consequently, the polyelectrolyte stabilized nZVI possesses strong electrostatic repulsion against the attachment to aquifer materials under neutral pH conditions.

In this chapter, polyelectrolytes such as PV3A and PAA were demonstrated to enhance nZVI mobility and dispersion. PV3A has been used as a dispersant generating nZVI with substantially better subsurface mobility potential (Sun et al. 2007). Previous work by Mallouk and coworkers has confirmed that PAA binding to nZVI creating highly negative surfaces effectively reduces the filtration removal by aquifer materials (Schrick et al. 2004). Based upon this work, the results confirmed that the transport efficiency of nZVI in porous media can be enhanced by the increase of the PAA dosage. Figure 5.8 shows the ratio of iron remained within the column to that in the effluent as a function of the PAA dose for the PAA stabilized nZVI. Even though adding small amounts of PAA (<5%) was not enough to produce sufficient repulsive forces for effective transport nZVI through the sand media, the increase in the PAA dosage (>20%) improved the mobility of the particles. Accordingly, more iron content was determined in the effluent as

increasing in the PAA dosage. Nonetheless there was still 57% of iron trapped in the column even at the PAA dosage of 50%. The nZVI stabilized with PAA may has lower transport efficiency than that with PV3A, the results shown here imply that a travel-distance-tunable nZVI may be designed to form an iron reactive barrier for the field remediation based upon the use of the PAA as the stabilizer.
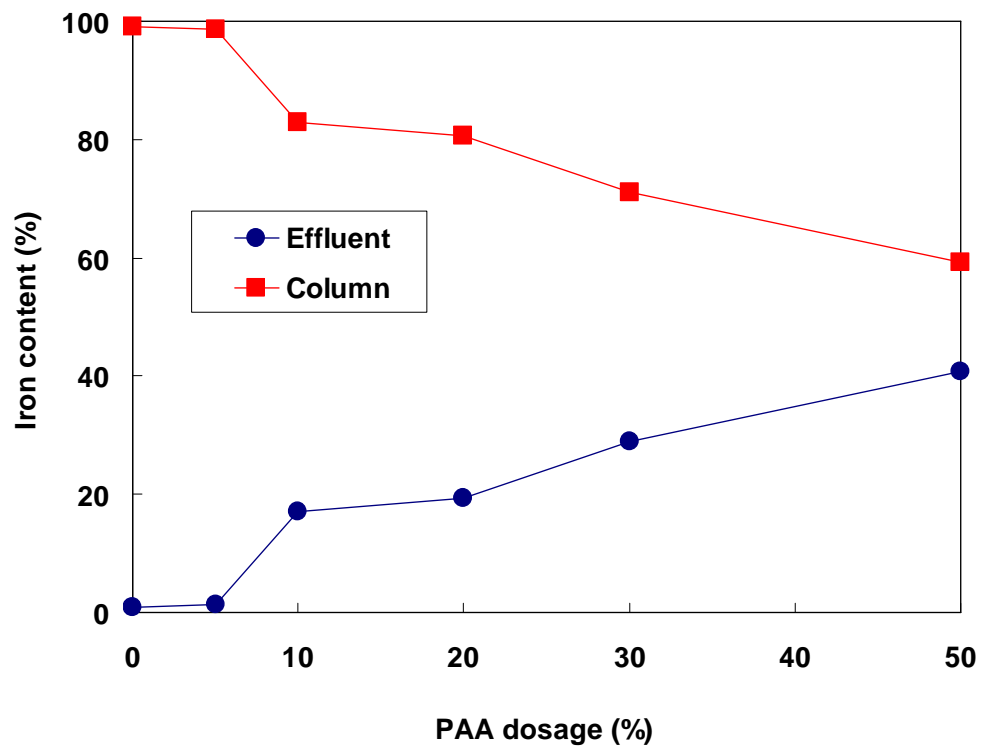
Figure 5.8. Iron content distribution between the column and the effluent from the column test with PAA stabilized nZVI at the various PAA dosage.

5.4 Conclusions

Because of the large specific surface area and potent reducing power, nZVI has found increasing environmental applications. However, both laboratory and field data show that mobility of nZVI under the natural groundwater flow conditions is very limited. We have examined PV3A and PAA as stabilizers for

113

enhanced transport of nZVI in continuous packed columns. Effects of nZVI stabilization by soy proteins were also tested using batch sedimentation experiments. Because it is an essential for field applications to use high injection concentrations of nZVI, to the best of our knowledge, this study is the first one to investigate nZVI stabilization and transport at high concentrations (10 g/L). Based upon our experimental results, the following conclusions can be drawn:

- PV3A and PAA promote dispersion and improve the transport efficiency of nZVI in the sand column experiments. PV3A has the best performance. PV3A stabilized nZVI readily passes through the sandy column without noteworthy retardation.

- Experiments with PAA stabilized nZVI demonstrate the concentration effect of PAA. Increasing the PAA dosage leads to higher mobility of nZVI; however, there is no additional benefit to the nZVI stability when the PAA dosage is higher than 50%.

- The column experiments show that the PAA stabilized nZVI can transport through the column; however, a retardation effect was observed. At the PAA dose of 50%, approximately 57% of nZVI still remained in the column.

- Soy proteins, which are less expensive, work well at the dosage of 30%. Column tests are still needed in order to better understand the transport behavior of the soy protein stabilized nZVI.

114

Nanoscale Calcium Peroxide Particles (Nano-peroxide) for Rapid Oxidation of Hydrocarbon

6.0 Abstract

The new nano size particles of calcium peroxide (nano-peroxide) were systhesized by the mechanical milling method in this paper. The particle size diameter (d_{50}) is around 120 nm with the large specific surface area at 30 m^2/g. The dissolution and reaction rate of nano-peroxide is faster than typical micro powder calcium peroxide by about 1.5 times. With metal catalyses (Fe^{2+}), nano-peroxide promotes modified Fenton's chemistry (MF) and shows the excellent performance for oxidizing hydrocarbon. Benzene solutions are completely oxidized as high as 800 mg/L of benzene and gasoline in contaminated solution is significantly decreased within 24 hours. pH is a major factor to increase the oxidizing effect of nano-peroxide. This chapter also reports the synthesis method, images and composition of nano-peroxide.

6.1 Introduction

Unintended release of petroleum products is a serious and widespread environmental problem. Each year, over 1.3 trillion gallons of petroleum is consumed globally. An inevitable issue arising from handling such a huge volume of petroleum and its derivative products is accidental oil spillage or leakage during transportation and storage processes. According to recent statistics from US EPA, there are over 500,000 Leaking Underground Storage Tanks (LUSTs) in the U.S. (EPA 2009). The costs of complete remediation of these sites may add up to over $250 billion dollars. Contamination of groundwater by Nonaqueous-phase liquids (NAPLs) leaking from USTs is a serious issue because some of NAPLs have been found to be toxic to both human beings and animals (Lough 1996).

Several remediation processes such as pump-and-treat, containment, in situ biodegradation, phytoremediation, soil washing, surfactant and cosolvent flushing, air stripping, and thermal processes have been applied for the remediation of NAPL-contaminated sites (Udell 1995, Reible 2002, Khaitan et al. 2006, Saba et al. 2001). These methods often require prolonged and intensive operations and are highly costly. For example, in-situ bioremediation utilizes locally stimulated or augmented microorganisms to decompose hydrocarbon contaminants to harmless substances, such as water and carbon dioxide. A bioremediation operation typically takes years to meet the clean-up goals due to lengthy periods necessary to establish optimal remediation conditions and for the microbes to adapt to the foreign contaminants. Repeated injections of oxygen and nutrients are typically needed. Chemical oxidation method requires high concentrations of strong oxidants (e.g., permanganate, or hydrogen peroxide as Fenton's reagent), which can cause severe damages to the local geochemistry and microbiology. The water-soluble oxidants

116

readily dissipate in soil and water and therefore have relatively short life-times in the subsurface.

A novel method using solid peroxide nanoparticles for hydrocarbon oxidation and remediation has been investigated at Lehigh University. The peroxide nanoparticles (nano-peroxide), solid or porous particles of calcium peroxide or magnesium peroxide with average size in the range of 10 to 100 nm, are formulated for optimal subsurface transport and for enhanced reactivity to achieve accelerated oxidation of hydrocarbon compounds.

Calcium peroxide (CaO_2) is well-known solid peroxide and has been traditionally used as an oxygen release compound (ORC) as following reaction:

$$2CaO_2 + 2H_2O \rightarrow 2Ca(OH)_2 + O_2 \tag{6.1}$$
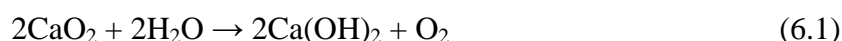
Oxygen released is dispersed with the flow of water and provides electron acceptor (O_2) for aerobic biodegradation of petroleum hydrocarbons (Schmidtke et al. 1999). Due to its small surface area, commercial calcium peroxide particles have limited oxidation power and are hardly exploited for chemical oxidation purpose. Therefore, the major use of calcium peroxide was for the enhanced biodegradation of pollutants in soil and groundwater such as petrochemical spills and other aerobically biodegradable compounds. Recent studies suggest that calcium peroxide (CaO_2) is a more effective source of H_2O_2 than liquid H_2O_2 (Ndjou'ou and Cassidy 2006, Bogan et al. 2003). CaO_2 dissolves to form H_2O_2 and $Ca(OH)_2$ via reaction 2, liberating a maximum of 0.47 g H_2O_2/g CaO_2 and heat ($\Delta G^\circ = -20.7$ kJ/mol) (Northup and Cassidy 2007, Northup and Cassidy 2008, Konigstein and Catlow 1998).

117

$$CaO_{2(S)} + 2H_2O \rightarrow H_2O_2 + Ca(OH)_{2(S)} \qquad (6.2)$$

The reaction of CaO_2 in water to create H_2O_2 depends on the rate of CaO_2 dissolution and the stability of H_2O_2 increases with decreasing pH (Northup and Cassidy 2007, Northup and Cassidy 2008). In the presence of ferrous ion (Fe^{2+}) and other promoters, reactive oxygen species (ROS) including hydroxide (OH•) radicals are readily formed due to Fenton chemistry (Walling 1975).

$$Fe^{2+} + H_2O_2 \rightarrow Fe^{3+} + OH^- + OH\bullet \qquad (6.3)$$

Fenton reaction is a powerful chemical oxidation for the destruction of many contaminants (Parsons 2004). The OH· (hydroxyl radical) is a strong oxidant, reacting with most contaminants at near diffusion-limited rate ($>10^9$ M^{-1} s^{-1}) (Northup and Cassidy 2007). Conventional Fenton chemistry actually maintains a pH below 3, which is unrealistic for the field work. Many remediation applications use a Fenton-like or modified Fenton's (MF) treatment which produces hydroxyl radicals at a pH near neutral. Liquid H_2O_2 and Fe^{2+} in reaction 3 are used as MF. However, liquid H_2O_2 is instability and its half-life is only minutes to hours (Northup and Cassidy 2008, ESTCP 1999). Excess H_2O_2 produces oxygen as shown in reaction (6.4):

$$2H_2O_2 \rightarrow H_2O + O_2 \qquad (6.4)$$

Without or disproportionation metal catalysts, the reaction (6.4) is considered to be the major loss of H_2O_2 at neutral pH (Buda et al. 2003, Watts et al. 1999, Watts and Stanton 1999). A lot of oxygen released from reaction (6.4) clogs pores around injection wells and promotes contaminant volatilization (Xu et al. 2006, Chen et al. 2001). On the other hands, calcium peroxide (CaO_2) is suggested to be more

118

effective source of H_2O_2 than liquid H_2O_2 (Ndjou'ou and Cassidy 2006, Northup and Cassidy 2007, Northup and Cassidy 2008).

Even though hydroxyl radical is a very strong oxidizing agent, there are some reports that show sometimes, the rate of contaminant oxidation in real treatment systems, soils, and groundwater, is effective as high as the oxidation rate in the controlled experiments in laboratory. The oxidation reaction in real situations is affected by scavengers that deactivate hydroxyl radical. Scavenging of hydroxyl radical can be the result of: 1) the chemicals added as part of Fenton's reagent and 2) naturally occurring species in the system (e.g., anions and organic matter) (Watts and Teel 2005). For example, carbonates (CO_3^{2-}) are most likely to scavenge hydroxyl radical and lower the effectiveness hydroxyl radical. Carbonates can react with hydroxyl radical and from $HCO_3\cdot$ that is a low oxidation reactivity agent (Hoigne and Bader 1978). Moreover, the natural organic matters in contaminated environment may act like competitors with the oxidative treatment of contaminants and lower the oxidation rate of hydroxyl radical (Watts and Teel 2005).

Most soils, groundwater, and treatment systems contain high concentration of carbonates, so high concentration hydroxyl radical is needed in the real applications. However, bicarbonate (HCO_3^-) has much lower reaction rate constant than the rate of carbonate and it is not considered to be a competitor in hydroxyl radical reaction (Hoigne and Bader 1978, Watts and Teel 2005). Therefore, to maintain high efficiency of hydroxyl radical reaction, controlling pH at neutral (below 9) can reduce the effect of carbonate in treatment systems. Calcium peroxide has been reported about its working condition at neutral pH around 7-8

119

(Northup and Cassidy 2008), so it is an effective hydrogen peroxide producing agent to be used in contaminant treatment.

The first discovery of nano-scale particles of calcium peroxide (nano-peroxide) is reported in this chapter. The mechanical grounding method, used to systhesize the nano particles, is explained. The physical and chemical properties of nano-peroxide were observed and compared with conventional calcium peroxide powder. Finally, the performance of nano-peroxide on oxidizing some petroleum hydrocarbons including gasoline contaminated wastewater is presented.

6.2 Materials and Methods

6.2.1 Chemical reagents

Hydrochloric acid (12.1 N) was purchased from EMD Chemicals and Fisher Chemicals, respectively. Pentane $\geq$ 99%, spectrophotometric grade and benzene were obtained from Sigma-Aldrich. 87 octane gasoline was purchased from gas station. Hydrogen peroxide liquid (H_2O_2) % used to producing nano-peroxide was provided by Sigma-Aldrich. 75% calcium peroxide powder was obtained from Sigma-Aldrich. Calcium hydroxide ($Ca(OH)_2$) was purchased from Fisher Chemicals. Ferrous Sulfate ($FeSO_4$) was obtained from Fisher Chemicals.

120

6.2.2 Scanning electron microscope (SEM), surface area, and x-ray diffraction (XRD)

SEM imaging was performed using a field-emission SEM (Hitachi S-4300) operating at 5.0 kV. Specific surface area of the nano-peroxide particles was measured using a Micrometrics Flowsorb 2305 following the classic Brunauer-Emmett-Teller (BET) method. Dried samples were first degassed at 170 ºC for 40 minutes. Adsorption of pure nitrogen by nano-peroxide sample was done in a sample tube at prescribed conditions followed by desorption of nitrogen as the temperature ramps us to room conditions. The amounts of nitrogen adsorbed and desorbed by the particles were measured and were used to calculate the total surface area and the mass-normalized specific surface area. The nano-peroxide particle samples were analyzed by x-ray diffraction (XRD) to determine their surface chemistry and crystal phase compositions. A Rigaku diffractometer (Rigaku, Japan) with Cu Kα radiation generated at 40 kV and 30 mA was used to perform XRD analysis.

6.2.3 Water chemistry

Water chemistry of nano-peroxide particles was conducted by the titration method. 400 mL samples of various amounts of Nano-peroxide and micro powder calcium peroxide solutions were mixed by magnetic stirrer at 300 rpm and the temperature was controlled to be at room temperature (22 ± 1 ºC). The solution samples were titrated by HCl 12.1 N. pH and ORP of the samples were monitored.

6.2.4 Batch experiments

Benzene: Saturated benzene solution concentration was measured by GC as described in analytical methods section. Various benzene concentration samples were prepared by diluting the saturated benzene solution. Reaction batch experiments were conducted in 100 mL glass bottle with sealed aluminum cap. The samples were shaken at 250 rpm. Various times of reaction experiments were tested with 100 mg/L benzene mixing with 1.6 g/L nano-peroxide samples. Oxidation reaction of nano-peroxide was examined by controlling various pH of the samples. pH of each sample was controlled by adding 12.1 N HCl.

Gasoline: Gasoline (87 octane) contaminated samples were prepared by mixing of pure 20 mL of pure gasoline with 1 L of water for 24 hr. The oxidation of gasoline contaminated samples was conducted in 100 mL glass bottle with sealed aluminum cap. The samples were shaken at 250 rpm for 24 hours and pH of each sample was controlled at 7 by adding 12.1 N HCl.

6.2.5 Analytical methods

Gas chromatograph (GC): Aqueous benzene and gasoline contaminated samples from batch experiments were measured by using n-Pentane extraction. Aqueous benzene samples were analyzed by a gas chromatograph (Shimadzu GC-17A) equipped with a flame ionization detector (FID) and Supelco SPB-624 capillary column (30m $\times$ 0.53mm). Temperature conditions are programmed as follows: oven temperature at 40 °C for 5 minute and temperature is increased at

122

rate of 10°C/min until oven temperature reaches to 200 °C for 5 minute with a split ratio of 10; injection port temperature at 250 °C; and detector temperature at 300 °C. The carrier gas was ultra-pure helium at a flow rate of 30 cm.min^{-1}.

Gas chromatograph mass spectrometer (GC/MS): Gasoline contaminated sample compositions were monitored by suing GC/MS and the samples were sent to outside laboratory.

pH/ORP measurement: A combination pH electrode (Orion) was used in conjunction with a Sension1 (Hach) meter to track solution pH. It was calibrated prior to each test. A combination Ag/AgCl reference electrode (Cole-Parmer) was used with a Model 420A pH/ORP meter (Orion) to monitor redox potential and was calibrated with fresh ZoBell solution before each test. Measured redox potential readings (mV) were converted to E_h, the potential relative to the standard hydrogen electrode, as a function of solution temperature by adding +199 mV at 25°C.

6.3 Synthesis of nano-peroxide

A Laboratory-use ball mill (Labstar$^®$) from Netzsch (Exton, PA, USA) was used to produce nano particles of calcium peroxide. The machine contains 2 sub-systems: (1) the milling system consisting of a motor, a grinding chamber, an agitator and beads, and (2) a particle circulation and cooling system containing a pump and a holding tank to control the temperature of the particle suspension in the tank and inside the mill as described in (Li et al. 2009). In a typical milling cycle, 1-2 kg of particles can be processed per batch. The setting used and the

results achieved (e.g. power input, milling time, and product yeild) on this mill are linearly scalable for large-scale production-sized mills which can process over 1000 kg of particles each batch (Li et al. 2009).

The steel beads (dia. 250 µm) were loaed into the milling chamber as the milling medium. The milling speed was 2000-2500 rpm to stir up the milling medium (beads). Calcium hydroxide ($Ca(OH)_2$) powder was added and smashed by the moving beads, and the impact energy fractures the micro scale powder into smaller particles. Liqiud H_2O_2 (30%) was added and the temperature of the milling chamber was controlled less than 35 ℃. The nano scale calcium peroxide particles were produced via the reaction of $Ca(OH)_2$ and H_2O_2. A stainless steel cylinder screen with laser-cut slots fits in at the open end of the agitator, which functions as a filter to retain the milling beads but allows the processed material to pass through and go into the holding tank. From the holding tank, the particles were recycled back to the milling system by circulation pump. The milling procedure used here begins with mixing 1000 grams of the feed particles in the holding tank for 30 minutes before the circulation pump and the motor were turned on. The particle samples can be collected at the outlet of the grinding chamber to assess the size reduction.

6.4 Results and Discussions

6.4.1 Characterization

Figure 6.1 shows scanning electron microscopy (SEM) images of nanoscale calcium peroxide. Individual particles remain dispersed or form loosely attached aggregates. The nano-peroxide particles have average size d_{50} at 120 nm. Close up

124

view of the image on the right reveals many cubic and rhombohedra structures. X-ray diffraction analysis (XRD) is present in Figure 6.2, confirming that nano-peroxide particles contain CaO_2 as the predominant phase, with small amounts of $Ca(OH)_2$ and $CaCO_3$ and trace levels of Ca and CaH_2 present as well (Fig 6.2. (a)), but calcium peroxide powder contains $CaCO_3$ as major component.
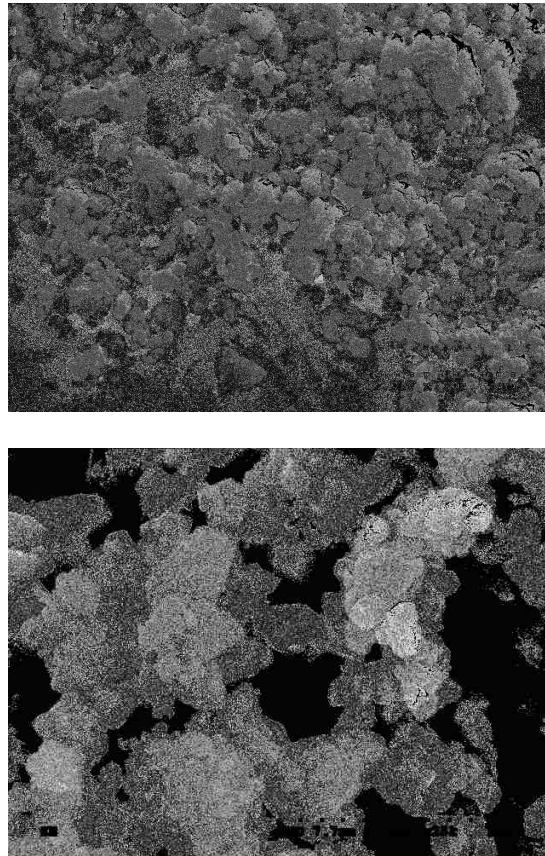
Figure 6.1. Scanning electron microscopic (SEM) images of nanoscale calcium peroxide (nano-peroxide) particles.

125
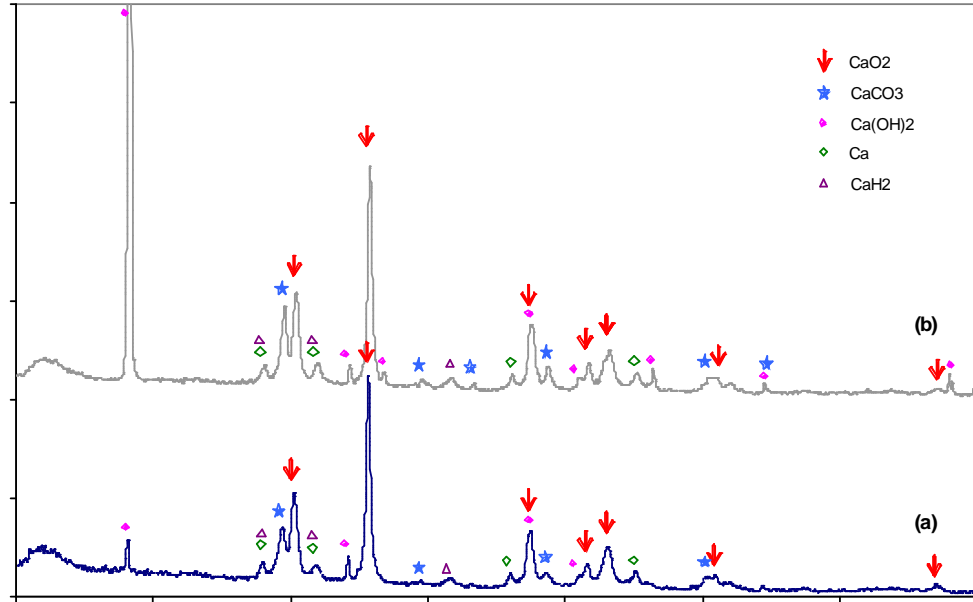
Figure 6.2. X-ray diffraction analysis (XRD) of nanoscale calcium peroxide (nano-peroxide) particles. a) nano-peroxide particles contain CaO₂ as the predominant phase, with small amounts of Ca(OH)₂ and CaCO₃ and trace levels of Ca and CaH₂. b) Calcium peroxide powder has CaCO₃ as major component.

Nano-peroxide is 1,000 times smaller than the commercial micro powder calcium peroxide products (e.g., PermeOx and ORC). As reaction rate scales proportionally with particle surface area, nano-peroxide has a much higher oxidant release rate. In addition to oxygen, hydrogen peroxide (H_2O_2) is formed on the surface of calcium peroxide. Table 6.1 shows specifications of nano-peroxide. The peroxide nanoparticles feature specific surface area over 30 m^2/g. The extremely large surface leads to rapid reaction rate including oxygen release, H_2O_2 forming reaction, modified Fenton reaction (MF), and hydrocarbon oxidation, due to the higher rate of dissolution (Northup and Cassidy 2008) and consequently low dose requirement for site remediation, rendering it as an effective oxidant for rapid oxidation of hydrocarbons.

Table 6.1. Specifications of nanoscale ZVI and CaO2 particles.

	NANO-Ox
Molecular Formula	$CaO_2(H_2O)_n$
Appearance	White to yellow slurry
Solid Content	33%
Apparent Density	0.85-1.05 kg/L
True Density	2.9 kg/L
Size (d_{50})	120 nm
Specific Surface Area	30 – 100 m^2/g
Target pollutant compounds	Gasoline Diesel BTEX Naphthalene PAHs MTBE

127

A common problem arising from using conventional micro powder peroxides in soil and groundwater treatment is the difficulty in handling, dispersing and subsurface injection of peroxide materials. Dry powders of solid peroxides have limited solubility in water, tend to clog in the equipment and piping system, and do not disperse well beyond the injection point. Nano-peroxides, on the other hand, are produced in the form of liquid slurry (10-50% solids) ready to be injected into contaminant sites. The nanoscale size minimizes the problem of gravity-induced sedimentation and allows better dispersion and mobility in the subsurface environment.

Another unique advantage of nano-peroxide is having an apparent density close to that of water. Tiny oxygen bubbles released continuously by nano-peroxide form a gas film adhering to the nanoparticle surface. As a result, nano-peroxide has an apparent density of 0.85 – 1.05 kg/L, allowing the particles to remain suspended or float on the surface of groundwater - the latter presents a promising solution to the remediation of lighter-than-water hydrocarbon phases (LNAPLS).

6.4.2   Water chemistry

6.4.2.1 Chemical properties

Nano-peroxide with various amounts at 0.4, 0.8, and 1.2 g in 400 mL water was titrated with HCl acid. pH and ORP of nanosclae calcium peroxide were measured and illustrated in Figure 6.3. Typical titration curves were expected to show the effect of HCl acid on nano-peroxide. pH of all mixtures started around 12

128

and continuously decreased to around 9 – 10; then immediately dropped to around 2- 3 after adding little amount of acid, and finally ended at pH around 1 - 2 (Fig. 6.3a). The inverse increasing curves were observed for ORP (Fig. 6.3b). Average alkalinity of nano-peroxide was calculated at 4,724 mg/L as $CaCO_3$ / g $nCaO_2$ and the amount of HCl acid needed to adjust pH of the mixture to 7 was 36.6 mmole $HCl/gnCaO_2$. There was no change in titration result when preparing the mixture of nano-peroxide with ferrous ion, catalyze for MF (data not shown).
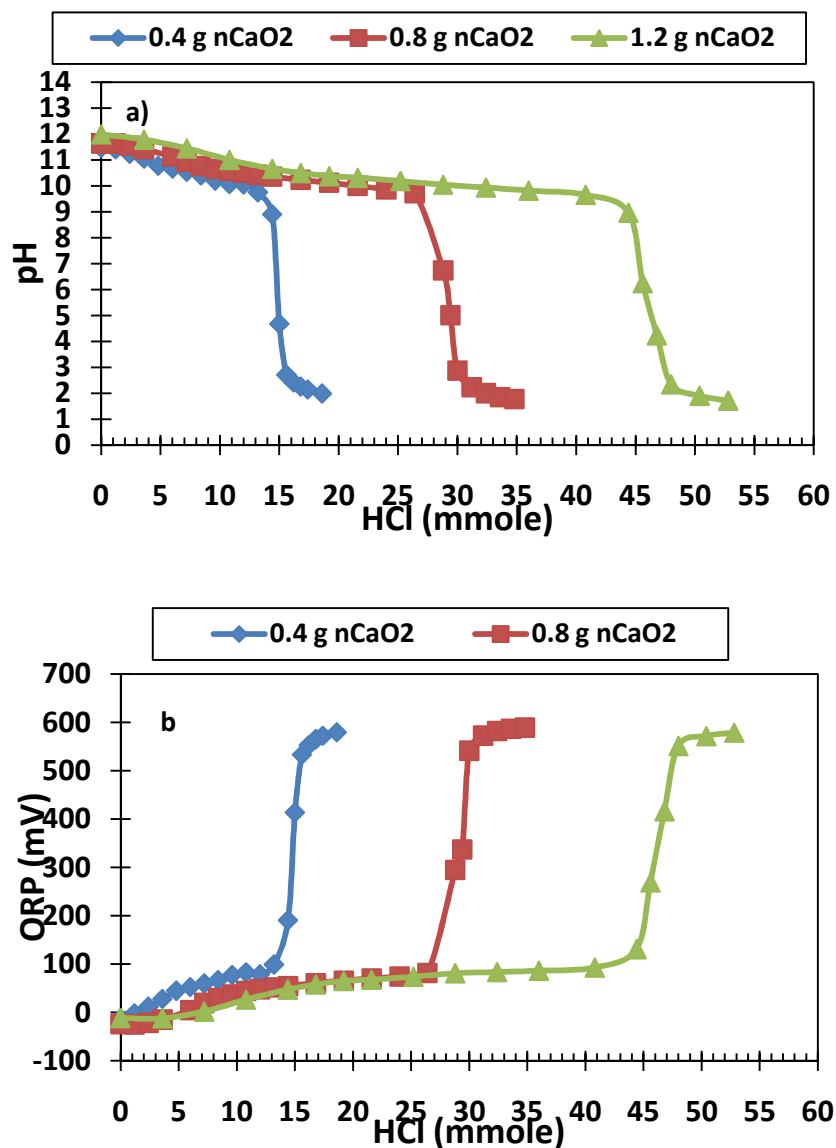
Figure 6.3. Titration properties of nano-peroxide a) pH and b) ORP.

0.8 g nano-peroxide and 0.8 g micro powder calcium peroxide (1.07 g of 75% CaO_2 powder) in 400 mL samples were titrated with HCl acid and the titration results were shown in Figure 6.4. The very identical titration graphs in pH and ORP were presented in both nano-peroxide and micro powder calcium peroxide suggesting that nanoscale particles have similar chemical properties to those of micro powder calcium peroxide. However, the titration time between nanoscale and micro powder calcium peroxide mixtures was different as shown in Figure 6.5. The time of titration was measured when steady point of both pH and ORP meters shows up after adding acid. Nano-peroxide reaction with acid took 54 minutes but micro powder calcium peroxide used 74 minutes to reach to pH 9.2, which was the last point before pH of both nanoscale and micro powder calcium peroxide was immediately dropped. At the end of both reactions at pH below 2, micro powder calcium peroxide took longer time around 1.5 times than nano-peroxide did (Fig. 6.5a). Moreover, during titration ORP of nano-peroxide mixture was slightly higher than ORP of micro powder mixture at the same time as shown Figure 6.5b, indicating the high oxidation power of nano-peroxide. Without catalysts, the oxidation power of calcium peroxide only comes from H_2O_2 production as reaction 6.2. The rate of H_2O_2 forming was depended on the rate of CaO_2 dissolution, (Ndjou'ou and Cassidy 2006, Bogan et al. 2003). The rate of CaO_2 dissolution was increased when pH was decreased (Northup and Cassidy 2008). The concentration of H_2O_2 in a 0.2% slurry of CaO_2 increased from 380 mg/L to 1,200 mg/L as the pH was decreased from 11 to 3 (Arienzo 2000). The small size of particles increased the surface areas and resulted in increasing dissolution of CaO_2. In consequence, the H_2O_2 production was increased.

130
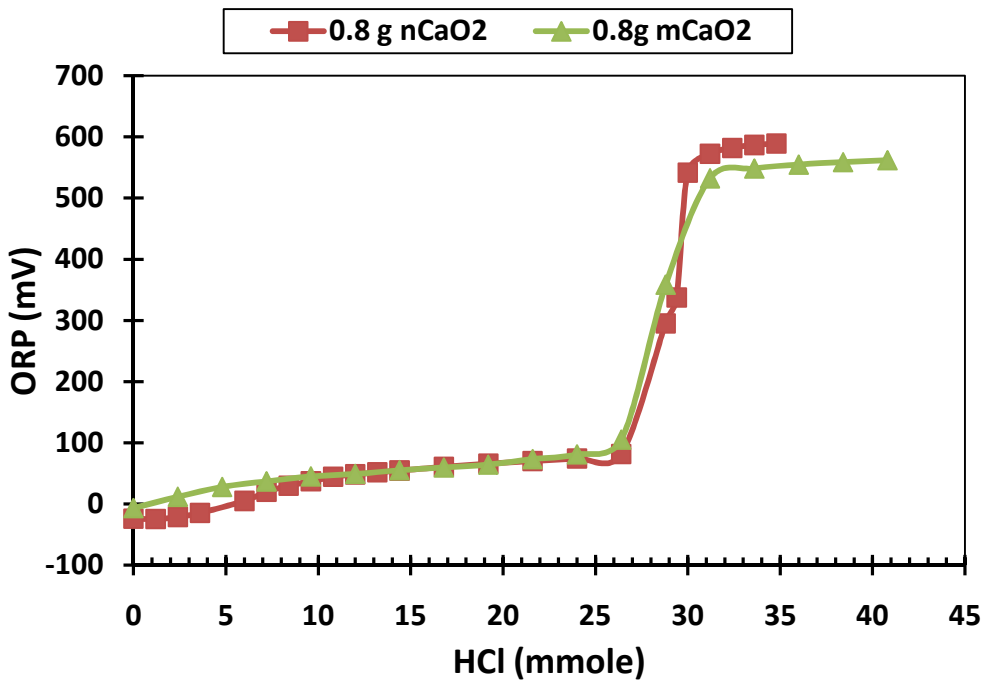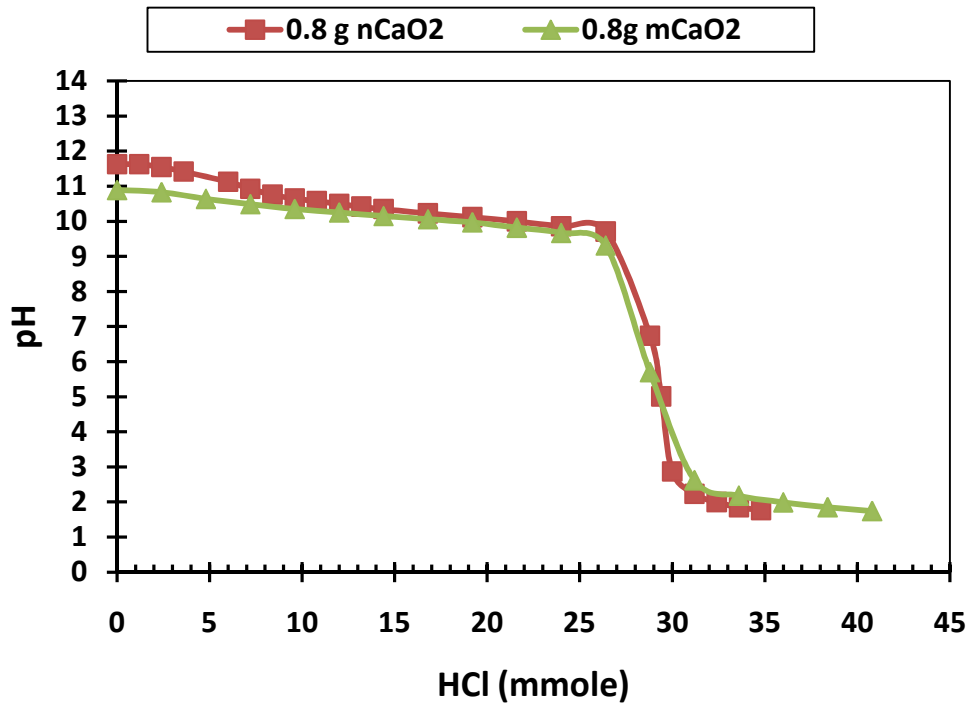
Figure 6.4. Comparison of propertis between nano-peroxide and micro powder calcium peroxide: a) ph and b) ORP.
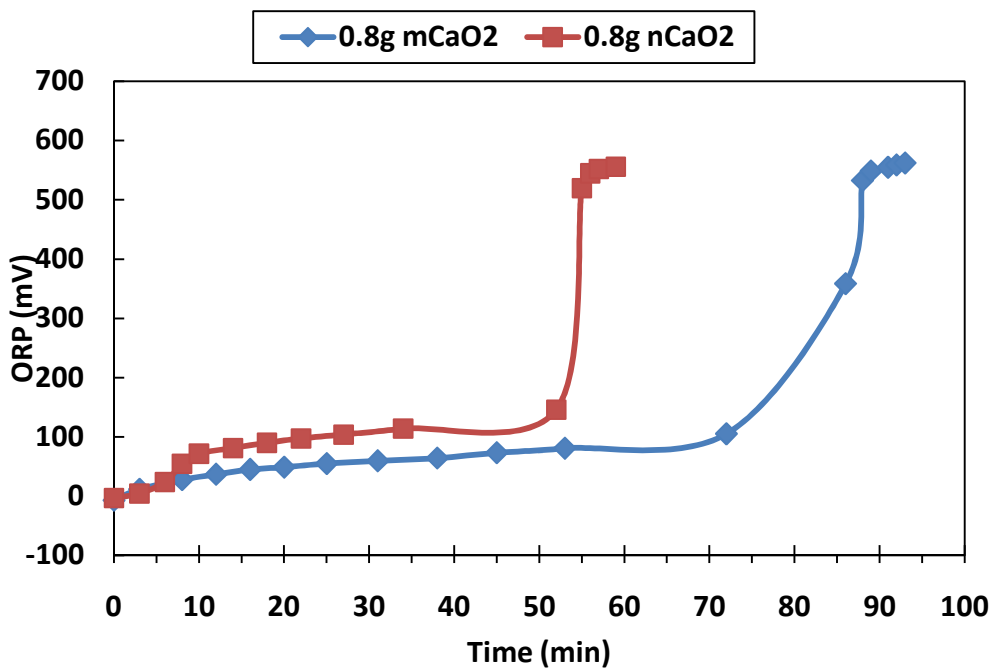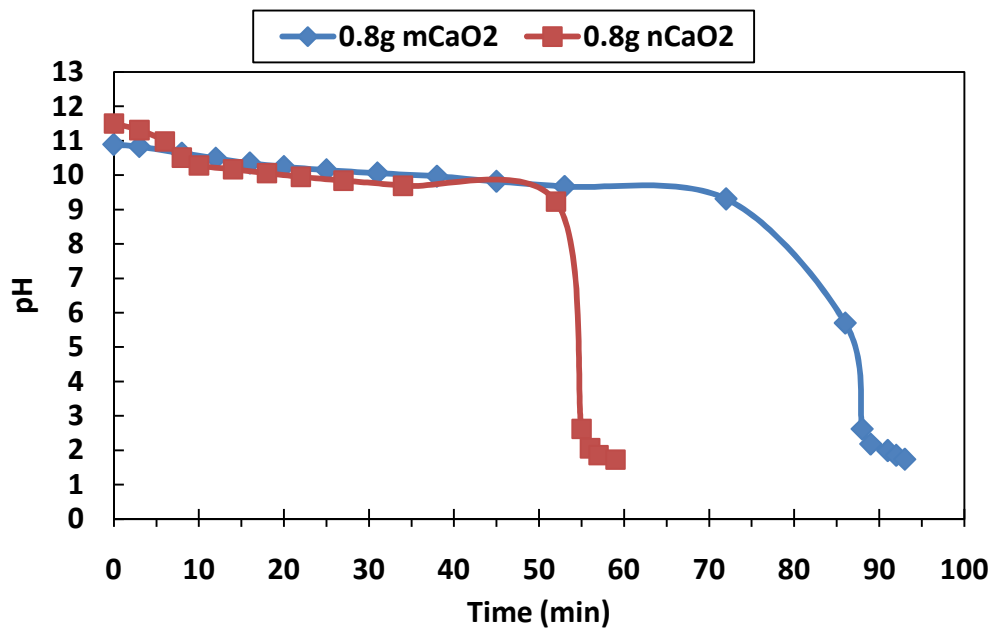
Figure 6.5. Titration time comparing between nano-peroxide and micro powder calcium peroxide: a) pH and b) ORP.

6.4.2.2 Oxygen release

Dissolved oxygen (DO) of 0.4 g of nanoscale and micro powder calcium peroxide in 400 mL samples was measured and presented in Figure 6.6. At pH above 10 (10 – 12), DO of micro powder calcium peroxide was slightly higher, but after pH is below 10, the DO of nano-peroxide was higher the average around 3 mg/L than DO of micro powder (18 mg/L for nanoscale and 15 mg/L for micro powder). Calcium peroxide (CaO_2) has been traditionally used for oxygen releasing compound (ORC). At high pH (above 10), CaO_2 forms O_2 through reaction 1. Decreasing pH of the solution increases dissolution of CaO_2, so it produces H_2O_2 through reaction 6.2. Without heavy metal catalysts such as Fe, H_2O_2 forms oxygen as following reaction 6.4. At pH lower than 9, H_2O_2 is the major source for producing oxygen in the solution (Buda et al. 2003, Watts et al. 1999). The production rate of H_2O_2 is depended upon the dissolution rate of CaO_2; therefore, dissolved oxygen results show higher dissolution rate of nano-peroxide than that of micro powder calcium peroxide in all pH below 10.

133
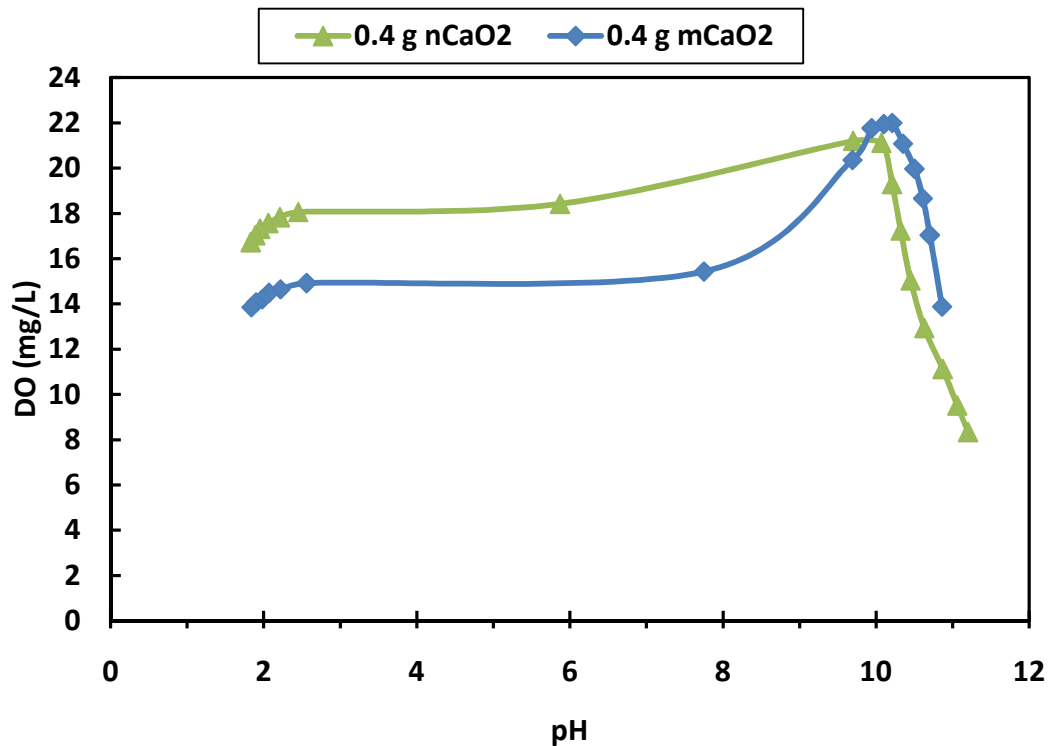
Figure 6.6. Dissolved oxygen concentration with pH of nano-peroxide and micro powder calcium peroxide.

6.4.3 Hydrocarbon oxidation

6.4.3.1 Benzene degradation

Figure 6.7 shows the reaction of 1.6 g/L nanoscale calcium peroxide with 20% /w of $FeSO_4$ mixed with 100 mg/L benzene with variation of pH from its original pH around 12 to 2, at 24 hr reaction time. Benzene was oxidized around 20% (C/Co = 0.8) after 24 hours reaction time at pH = 12. The oxidizing power of CaO_2 is created by H_2O_2 production to from modified Fenton (MF) in reactions 6.2, 6.3, and 6.4, and CaO_2 starts to form H_2O_2 when pH is decreased (Northup and Cassidy 2008, Ndjou'ou and Cassidy 2006, Bogan et al. 2003). The concentration

content of benzene (C/Co) was decreased when the pH of the samples were decreased. After pH lower than 8.5, the concentration content was dropped to zero (or below detection limit) indicating that complete reaction was occurred. Figure 6.8 shows the oxidation of 800 mg/L benzene (almost half of benzene solubility) with 1.6 g/L nano-peroxide and 20% /w of $FeSO_4$ and pH of the sample was controlled at 7. Complete removal of benzene was still performed in 24 hours reaction time.
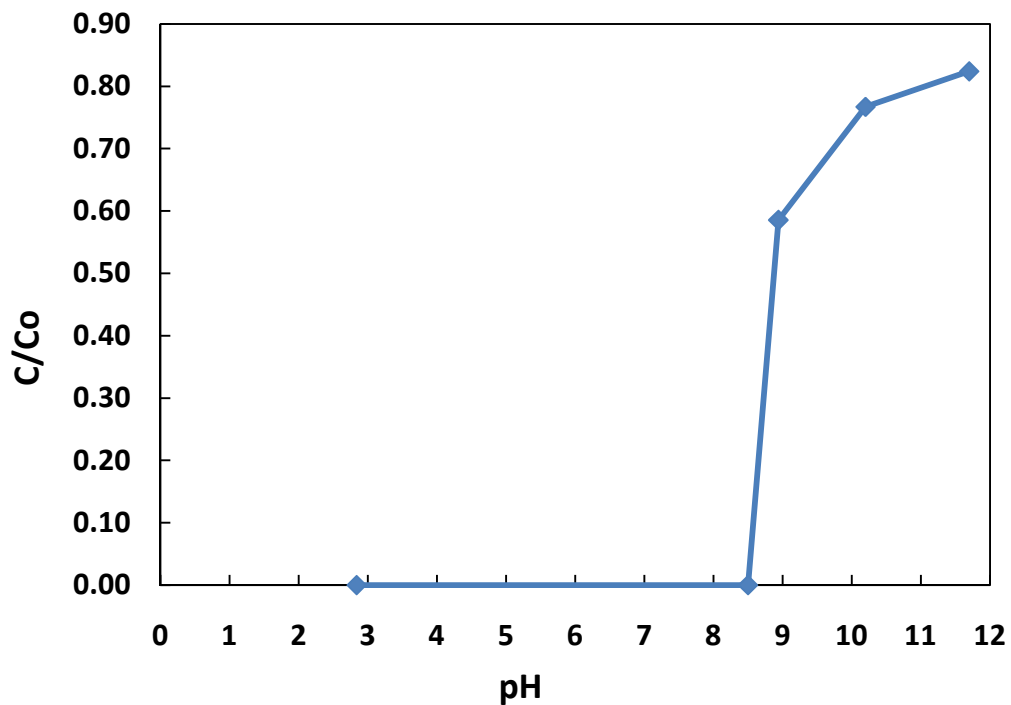
Figure 6. 7. The oxidation of 100 mg/L benzene with nano-peroxide and 20% /w of $FeSO_4$ in various pH at 24 hours reaction time.
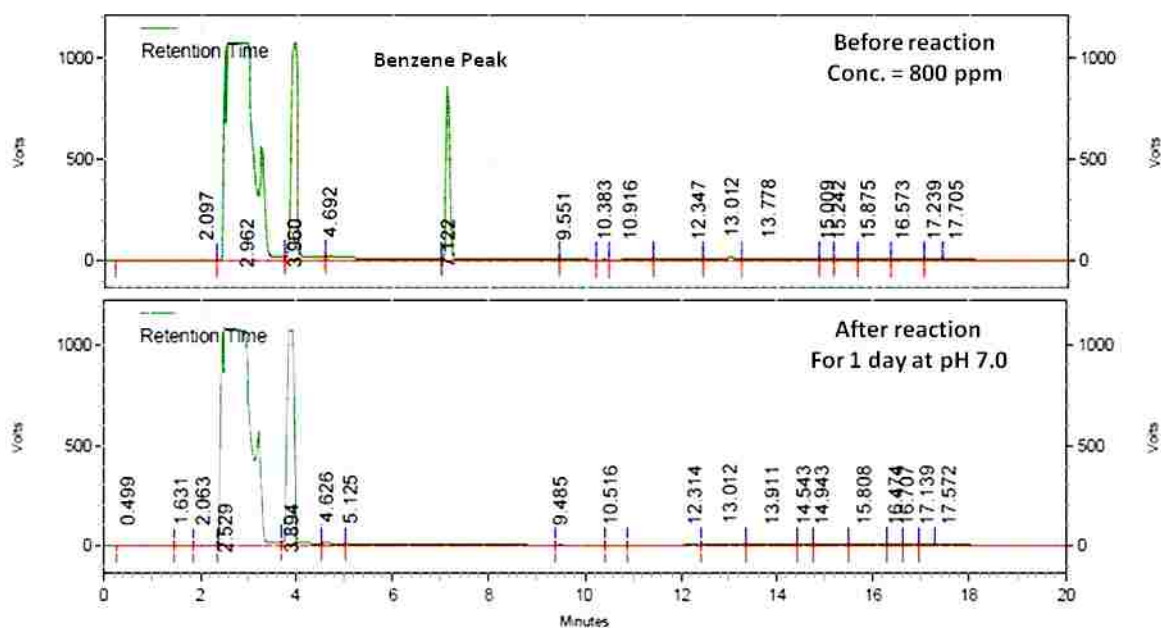
Figure 6.8. the oxidation of 800 mg/L benzene (almost half of benzene solubility) with 1.6 g/L nano-peroxide and 20% /w of FeSO$_4$ and pH = 7.

The oxidation power of calcium peroxide comes from MF chemistry by conversion of H$_2$O$_2$ to OH·. At pH=12, typical micro calcium peroxide does not form H$_2$O$_2$ and does not show any oxidation reaction (Northup and Cassidy 2008). Instead of creating H$_2$O$_2$, calcium peroxide tries to form oxygen at high pH (reaction 6.1). H$_2$O$_2$ formed by calcium peroxide starts when decreasing pH and is depended on dissolution rate of CaO$_2$. With Fe^{2+} catalyst, OH·, very high oxidizing agent (reaction 6.2, 6.3), is formed and hydrocarbon is oxidized. Interestingly, our results showed that there was benzene removal even at high pH like 12 (Fig. 6.7), suggesting that the benzene oxidation reaction was occurred and nano-peroxide can form H$_2$O$_2$ at high pH. These results confirm that there is dissolution of nano-peroxide even at pH 12, though the dissolution rate is slow. Benzene oxidation reaction was increased by decreasing pH of the solution. This result is consistent

136

with Northup and Cassiday (2008) report. Moreover, the result in Fig. 6.8 also shows high oxidation power of our nano-peroxide that can remove 800 mg/L benzene in one day.

6.4.3.2 Gasoline degradation

Gasoline contaminated water sample was mixed with 1.6 g/L nano-peroxide and 20% /w of $FeSO_4$ at pH 7 and the GC result is shown in Figure 6.9. Significant decrease of all peaks was observed in one day reaction. Figure 6.10 presents the GC-MS result of a gasoline sample reacted with nano-peroxide with $FeSO_4$. All peaks were identified and are shown in Fig. 10b. After 24 hours reaction, the significant decrease of all peaks was found in both GC and GC-MS results.

Calcium peroxide has been reported to be an excellent chemical oxidants for treating petroleum hydrocarbons (Gryzenia et al. 2009). More than 90% removal of contaminated PAH and hydrocarbon up to C_{34} structure waste and > 80% removal of contaminated hydrocarbon > C_{34} structure were reported (Gryzenia et al. 2009, Northup and Cassidy 2007). The beneficial effect of using calcium peroxide MF reaction has been reported as surfactant production during the PAH degradation process (Gryzenia et al. 2009, Northup and Cassidy 2007). Very high concentration (higher than persulfate did) of surfactant helps emulsify high MW PAH and gain availability to be chemically oxidized and/or biodegraded (Gryzenia et al. 2009). However, the degradation process by typical calcium proxide takes several days to removal the hydrocarbon. Therefore, the higher dissolution rate of nano-peroxide in this report can be expected to create better MF

137

compared to typical micro particle calcium peroxide and shorten the reaction time

for hydrocarbon remediation.
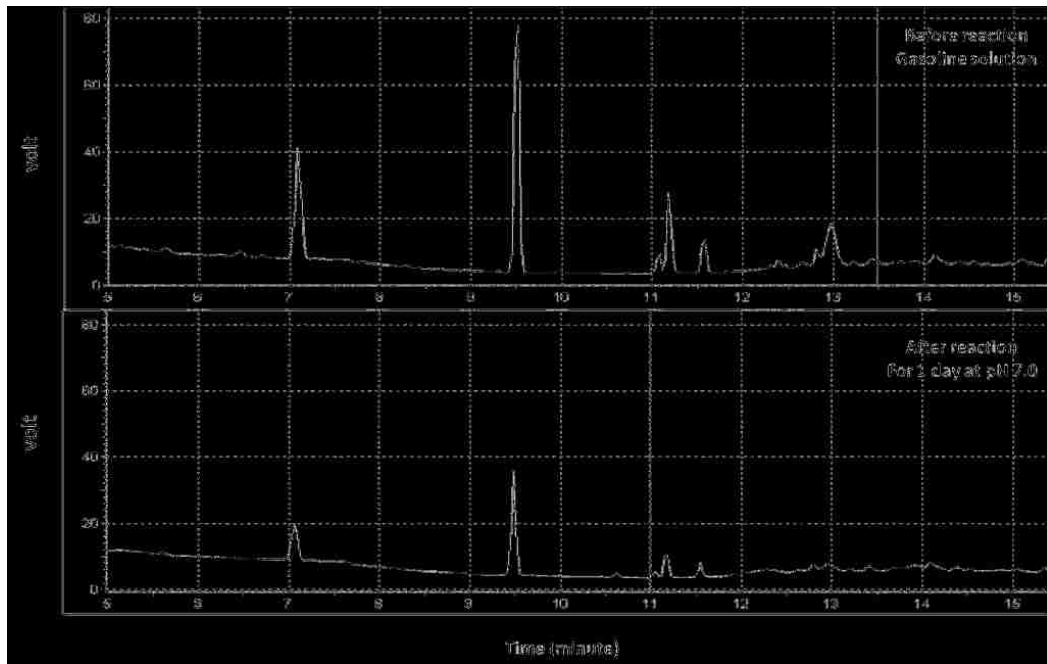
Figure 6.9. GC analysis of Gasoline contaminated water sample mixed with 1.6 g/L nano-peroxide and 20% /w of FeSO₄ at pH = 7.

138
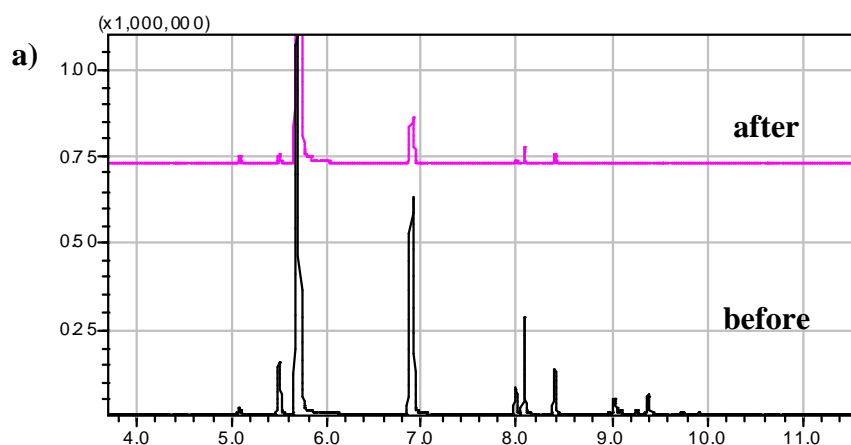
ID#	Name	Conc	Area	Ret.Time	Type	m/z	Height
1	benzene	12.130492	26226	5.510	Target	78.00	9571
2	Fluorobenzen	1.000000	304058	5.701	ISTD	70.00	112502
3	Toluene	17.566283	117018	6.893	Target	91.00	48379
4	Ethylbenzene	13.698874	10216	7.998	Target	91.00	4544
5	xylene-1	12.873778	29285	8.079	Target	91.00	12832
6	xylene-2	13.102511	14634	8.391	Target	91.00	6431
7	propylbenzen	9.430242	1096	8.969	Target	91.00	475
8	3-1	10.584393	5957	9.031	Target	105.00	1633
9	3-2	38.655900	5957	9.031	Target	105.00	1633
10	3-3	9.065467	1536	9.265	Target	105.00	633
11	3-4	6.326833	3146	9.393	Target	105.00	1357
12	3-5	6.350706	691	9.733	Target	105.00	297

Figure 6.10. GC-MS analysis of Gasoline contaminated water sample mixed with nano-peroxide and 20% /w of FeSO$_2$: a) GC-MS analysis and b) peaks identification.

6.5 Conclusions

The nano particles of calcium peroxide (nano-peroxide) were synthesized and firstly presented in this report. Specifications of solid peroxide nanoparticles are summarized in Table 6.1. The dissolution rate of nano-peroxide was higher than that of typical micro powder calcium peroxide, helping to create better MF and better releasing oxygen. The oxidation reaction of benzene and gasoline

139

contaminated wastewater by nano-peroxide was fast (within 24 hours). Figure 6.11 summarizes the expected major reaction mechanisms of nano-peroxide. The technology in this report is applicable to the following categories of contaminants:

1) Petroleum products including gasoline, kerosene, diesel, jet fuel and other fuel oils;

2) Petroleum additives (MTBE);

3) Benzene, toluene, ethyl benzene, xylene and other VOC compounds;

4) Poly-aromatic compounds such as naphthalene and PAHs.

Oxygen release:

$$2CaO_2 + 2H_2O \rightarrow 2Ca(OH)_2 + O_2$$

Surface oxidation (Modified Fenton's Reaction: OH·):

$$CaO_{2(S)} + 2H_2O \rightarrow H_2O_2 + Ca(OH)_{2(S)}$$

$$Fe^{2+} + H_2O_2 \rightarrow Fe^{3+} + OH^- + OH\bullet$$
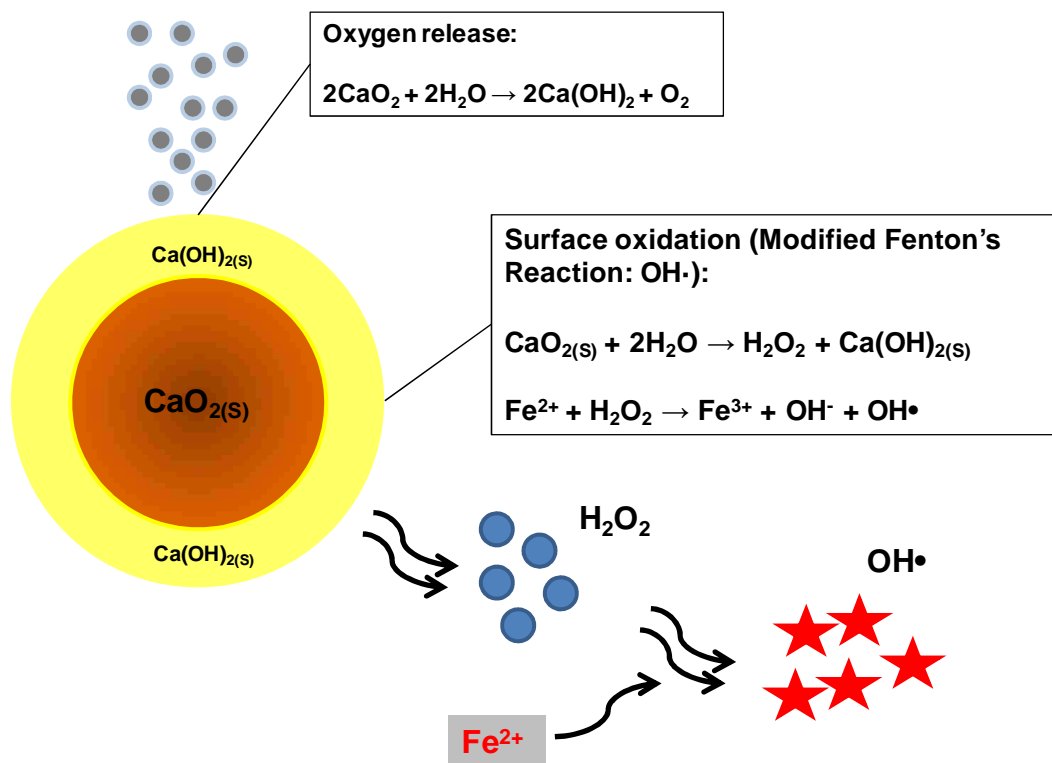
Figure 6.11. Mechanisms of nano-Ox for treatment of hydrocarbon compounds.

CHAPTER 7

CONCLUSIONS

Nano scale particles have been created for more than a decade. Due to their special abilities such as high specific areas and high reactivity, nano particles have been a new promising method to clean up the environmental contamination problems which used to be challenging in the past. Nano ZVI, one class of nano particles, have been studied and applied to remediate many contaminants, especially chlorinated organic compounds. Even though there are extensive studies conducted on nZVI abilities to reduce chlorinated hydrocarbon, especially trichloroethylene (TCE), few reports have mentioned about pure dense nonaqueous-phase liquids (DNAPLs). To improve the remediation of TCE in underground environment, nZVI was tested to directly attack the pure source of TCE in this work. One of the major problems of using nZVI in groundwater remediation is its mobility in subsurface environment. In this report, several biodegradable polymers and natural products were applied to enhance the transport of nZVI through the porous media.

New type of nano scale particles was synthesized in this work. Nano particles of solid peroxide such as calcium peroxide with high oxidizing power were preliminarily characterized and tested. Experiments were set up to test their abilities to oxidize hydrocarbon such as petroleum hydrocarbon.

141

The summary of experimental results and implication of both nano particles types, nZVI and nano-peroxide, are as following:

1. nZVI has good capability to remove TCE pure phase, and the reaction product (ethane) in head space gas confirms the TCE chlorination by nZVI. Not only TCE dechlorination reaction is conducted by nZVI, but also TCE liquids are absorbed in nZVI sludge. These absorption of TCE in nZVI helps enhance the TCE removal efficiency.

2. nZVI surface may be the important factor in the TCE removal process. High amount of nZVI in very limited space such as in subsurface environment, decreases the available exposed surface area of nZVI, resulting in lower removal efficiency. The experimental results indicate that continuously injecting small amount of nZVI has better removal efficiency than that of introducing high amount of nZVI at the beginning of the process.

3. PV3A and PAA promote dispersion and improve the transport efficiency of nZVI in the sand column experiments. PV3A has the best performance; it stabilized nZVI to readily pass through the sandy column without noticeable retardation.

4. Experiments with PAA stabilized nZVI demonstrated that increasing PAA dosage leads to higher mobility of nZVI. However, there was no additional benefit to nZVI stability when the PAA dosage was raised to higher than

142

50% by weight of nZVI. The column experiments show that the PAA stabilized nZVI can transport through the column; however, a retardation effect was observed. At the PAA dose of 50% by weight of nZVI, approximately 57% of nZVI still remained in the column.

5. Soy protein, which is less expensive, work well at the dosage of 30% by weight of nZVI. Column tests are still needed in order to better understand the transport behavior of the soy protein stabilized nZVI.

6. The nano particles of calcium peroxide (nano-peroxide) were synthesized and presented in this report for the first time. The dissolution rate of nano-peroxide was higher than that of typical micro powder calcium peroxide, helping to create better spell out MF and better releasing of oxygen. The oxidation reaction of benzene and gasoline contaminated wastewater by nano-peroxide was fast (within 24 hours). The new nano particles technology in this report is applicable to the following categories of contaminants: 1) petroleum products including gasoline, kerosene, diesel, jet fuel and other fuel oils; 2) petroleum additives (MTBE); 3) benzene, toluene, ethyl benzene, xylene and other VOC compounds; and 4) poly-aromatic compounds such as naphthalene and PAHs.

References

Arienzo, M. (2000) Degradation of 2,4,6-trinitrotoluene in water and soil slurry utilizing a calcium peroxide compound. *Chemosphere,* 40**,** 331-337.

Arnold, W. A. & A. L. Roberts (2000) Pathways and kinetics of chlorinated ethylene and chlorinated acetylene reaction with Fe(O) particles. *Environmental Science & Technology,* 34**,** 1794-1805.

Bedient, P. B., H. S. Rifal & C. J. Newell. 1999. *Ground Water Contamination: Transport and Remediation*. Prentice-Hall.

Bogan, B. W., V. Trbovic & J. R. Paterek (2003) Inclusion of vegetable oils in Fenton's chemistry for remediation of PAH-contaminated soils. *Chemosphere,* 50**,** 15-21.

Brezonik, P. L. 1994. *Chemical Kinetics and Process Dynamics in Aquatic Systems*. Lewis Publishers.

Buda, F., B. Ensing, M. C. M. Gribnau & E. J. Baerends (2003) O-2 evolution in the Fenton reaction. *Chemistry-a European Journal,* 9**,** 3436-3444.

Cao, J. S., P. Clasen & W. X. Zhang (2005a) Nanoporous zero-valent iron. *Journal of Materials Research,* 20**,** 3238-3243.

Cao, J. S., D. Elliott & W. X. Zhang (2005b) Perchlorate reduction by nanoscale iron particles. *Journal of Nanoparticle Research,* 7**,** 499-506.

Chen, G., G. E. Hoag, P. Chedda, F. Nadim, B. A. Woody & G. M. Dobbs (2001) The mechanism and applicability of in situ oxidation of trichloroethylene with Fenton's reagent. *Journal of Hazardous Materials,* 87**,** 171-186.

144

Cheng, R., J. L. Wang & W. X. Zhang (2006) The research progress on degradation of halogenated organic compounds by nano iron. *Progress in Chemistry,* 18**,** 93-99.

Choi, C. J., X. L. Dong & B. K. Kim (2001) Microstructure and magnetic properties of fe nanoparticles synthesized by chemical vapor condensation. *Materials Transactions,* 42**,** 2046-2049.

Cumbal, L. & A. K. Sengupta (2005) Arsenic removal using polymer-supported hydrated iron(III) oxide nanoparticles: Role of Donnan membrane effect. *Environmental Science & Technology,* 39**,** 6508-6515.

Deppert, K., M. N. A. Karlsson, B. A. Wacaser, L. S. Karlsson & J. O. Malm (2005) Size-controlled nanoparticles by thermal cracking of iron pentacarbonyl. *Applied Physics a-Materials Science & Processing,* 80**,** 1579-1583.

DOE. 2002. http://www.science.doe.gov/grants/Fr02-03.html.

Elihn, K., F. Otten, M. Boman, F. E. Kruis, H. Fissan & J. O. Carlsson (1999) Nanoparticle formation by laser-assisted photolysis of ferrocene. *Nanostructured Materials,* 12**,** 79-82.

Elliott, D. W., H. L. Lien & W. X. Zhang (2009) Degradation of Lindane by Zero-Valent Iron Nanoparticles. *Journal of Environmental Engineering-Asce,* 135**,** 317-324.

Elliott, D. W. & W. X. Zhang (2001) Field assessment of nanoscale biometallic particles for groundwater treatment. *Environmental Science & Technology,* 35**,** 4922-4926.

EPA. 2009. Underground Storage Tanks. http://www.epa.gov/swerust1/index.htm.

ESTCP. 1999. Technology status review: in situ oxidation. Arlington, Virginia, USA.

Everett, D. H. 1989. *Basic Principles of Colloid Science*. London: Royal Society of Chemistry.

Gillham, R. W. & S. F. Ohannesin (1994) ENHANCED DEGRADATION OF HALOGENATED ALIPHATICS BY ZERO-VALENT IRON. *Ground Water,* 32**,** 958-967.

Glazier, R., R. Venkatakrishnan, F. Gheorghiu, L. Walata, R. Nash & W. X. Zhang (2003) Nanotechnology takes root. *Civil Engineering,* 73**,** 64-69.

Goldstein, J. 2003. *Scanning electron microscopy and x-ray microanalysis*. New York: Kluwer Academic/Plenum Publishers.

Grittini, C., M. Malcomson, Q. Fernando & N. Korte (1995) RAPID DECHLORINATION OF POLYCHLORINATED-BIPHENYLS ON THE SURFACE OF A PD/FE BIMETALLIC SYSTEM. *Environmental Science & Technology,* 29**,** 2898-2900.

Gryzenia, J., D. Cassidy & D. Hampton (2009) Production and accumulation of surfactants during the chemical oxidation of PAH in soil. *Chemosphere,* 77**,** 540-545.

Gu, B., T. J. Phelps, L. Liang, M. J. Dickey, Y. Roh, B. L. Kinsall, A. V. Palumbo & G. K. Jacobs (1999) Biogeochemical dynamics in zero-valent iron columns: Implications for permeable reactive barriers. *Environmental Science & Technology,* 33**,** 2170-2177.

Harris, L. A., J. D. Goff, A. Y. Carmichael, J. S. Riffle, J. J. Harburn, T. G. St Pierre & M. Saunders (2003) Magnetite nanoparticle dispersions stabilized with triblock copolymers. *Chemistry of Materials,* 15**,** 1367-1377.

146

He, F. & D. Y. Zhao (2005) Preparation and characterization of a new class of starch-stabilized bimetallic nanoparticles for degradation of chlorinated hydrocarbons in water. *Environmental Science & Technology,* 39**,** 3314-3320.

He, F., D. Y. Zhao & C. Paul (2010) Field assessment of carboxymethyl cellulose stabilized iron nanoparticles for in situ destruction of chlorinated solvents in source zones. *Water Research,* 44**,** 2360-2370.

Henn, K. W. & D. W. Waddill (2006) Utilization of nanoscale zero-valent iron for source remediation—A case study. *Remediation Journal,* 16**,** 57-77.

Hoigne, J. & H. Bader (1978) Ozonation of Water - Kinetics of Oxidation of Ammonia by Ozone and Hydroxyl Radicals. *Environmental Science & Technology,* 12**,** 79-84.

http://chemed.chem.purdue.edu/. The Chemistry of Hemoglobin and Myoglobin. College of Science, Purdue University.

Jang, M., W. F. Chen & F. S. Cannon (2008) Preloading hydrous ferric oxide into granular activated carbon for arsenic removal. *Environmental Science & Technology,* 42**,** 3369-3374.

JCPDs. 1998. *International Centre for Diffraction Data.*

Jia, Y. F. & G. P. Demopoulos (2005) Adsorption of arsenate onto ferrihydrite from aqueous solution: Influence of media (sulfate vs nitrate), added gypsum, and pH alteration. *Environmental Science & Technology,* 39**,** 9523-9527.

Johnson, T. L., M. M. Scherer & P. G. Tratnyek (1996) Kinetics of halogenated organic compound degradation by iron metal. *Environmental Science & Technology,* 30**,** 2634-2640.

Kanel, S. R., R. R. Goswami, T. P. Clement, M. O. Barnett & D. Zhao (2008) Two dimensional transport characteristics of surface stabilized zero-valent iron nanoparticles in porous media. *Environmental Science & Technology,* 42**,** 896-900.

Kanel, S. R., B. Manning, L. Charlet & H. Choi (2005) Removal of arsenic(III) from groundwater by nanoscale zero-valent iron. *Environmental Science & Technology,* 39**,** 1291-1298.

Kanel, S. R., D. Nepal, B. Manning & H. Choi (2007) Transport of surface-modified iron nanoparticle in porous media and application to arsenic(III) remediation. *Journal of Nanoparticle Research,* 9**,** 725-735.

Kang, S. K., K. H. Choo & K. H. Lim (2003) Use of iron oxide particles as adsorbents to enhance phosphorus removal from secondary wastewater effluent. *Separation Science and Technology,* 38**,** 3853-3874.

Kanti Sen, T. & K. C. Khilar (2006) Review on subsurface colloids and colloid-associated contaminant transport in saturated porous media. *Adv Colloid Interface Sci,* 119**,** 71-96.

Khaitan, S., S. Kalainesan, L. E. Erickson, P. Kulakow, S. Martin, R. Karthikeyan, S. L. L. Hutchinson, L. C. Davis, T. H. Illangasekare & C. Ng'oma (2006) Remediation of sites contaminated by oil refinery operations. *Environmental Progress,* 25**,** 20-31.

Kim, H. J., T. Phenrat, R. D. Tilton & G. V. Lowry (2009) Fe-0 Nanoparticles Remain Mobile in Porous Media after Aging Due to Slow Desorption of Polymeric Surface Modifiers. *Environmental Science & Technology,* 43**,** 3824-3830.

Konigstein, M. & C. R. A. Catlow (1998) Ab initio quantum mechanical study of the structure and stability of the alkaline earth metal oxides and peroxides. *Journal of Solid State Chemistry,* 140**,** 103-115.

Korte, N., R. Muftikian, C. Grittini, Q. Fernando, J. Clausen & L. Y. Liang (1995) ORNL MMES RESEARCH INTO REMEDIAL APPLICATIONS OF ZERO-VALENCE METALS .2. BIMETALLIC ENHANCEMENTS. *Abstracts of Papers of the American Chemical Society,* 209**,** 228-ENVR.

Li, L., M. H. Fan, R. C. Brown, J. H. Van Leeuwen, J. J. Wang, W. H. Wang, Y. H. Song & P. Y. Zhang (2006a) Synthesis, properties, and environmental applications of nanoscale iron-based materials: A review. *Critical Reviews in Environmental Science and Technology,* 36**,** 405-431.

Li, S. L., W. L. Yan & W. X. Zhang (2009) Solvent-free production of nanoscale zero-valent iron (nZVI) with precision milling. *Green Chemistry,* 11**,** 1618-1626.

Li, X. Q., D. W. Elliott & W. X. Zhang (2006b) Zero-valent iron nanoparticles for abatement of environmental pollutants: Materials and engineering aspects. *Critical Reviews in Solid State and Materials Sciences,* 31**,** 111-122.

Li, X. Q. & W. X. Zhang (2006) Iron nanoparticles: the core-shell structure and unique properties for Ni(II) sequestration. *Langmuir,* 22**,** 4638-4642.

Liang, C. J., Z. S. Wang & C. J. Bruell (2007) Influence of pH on persulfate oxidation of TCE at ambient temperatures. *Chemosphere,* 66**,** 106-113.

Liang, L. Y., N. Korte, J. D. Goodlaxson, J. Clausen, Q. Fernando & R. Muftikian (1997) Byproduct formation during the reduction of TCE by zero-valence iron and palladized iron. *Ground Water Monitoring and Remediation,* 17**,** 122-127.

149

Lien, H. L., Y. S. Jhuo & L. H. Chen (2007) Effect of heavy metals on dechlorination of carbon tetrachloride by iron nanoparticles. *Environmental Engineering Science,* 24**,** 21-30.

Lien, H. L. & W. X. Zhang (1999) Transformation of chlorinated methanes by nanoscale iron particles. *Journal of Environmental Engineering-Asce,* 125**,** 1042-1047.

Lien, H. L. & W. X. Zhang. 2001. Nanoscale iron particles for complete reduction of chlorinated ethenes. 97-105.

Lien, H. L. & W. X. Zhang (2005) Hydrodechlorination of chlorinated ethanes by nanoscale Pd/Fe bimetallic particles. *Journal of Environmental Engineering-Asce,* 131**,** 4-10.

Lien, H. L. & W. X. Zhang (2007) Nanoscale Pd/Fe bimetallic particles: Catalytic effects of palladium on hydrodechlorination. *Applied Catalysis B-Environmental,* 77**,** 110-116.

Lin, Y. H., H. H. Tseng, M. Y. Wey & M. D. Lin (2010) Characteristics of two types of stabilized nano zero-valent iron and transport in porous media. *Science of the Total Environment,* 408**,** 2260-2267.

Liu, Y. Q., S. A. Majetich, R. D. Tilton, D. S. Sholl & G. V. Lowry (2005) TCE dechlorination rates, pathways, and efficiency of nanoscale iron particles with different properties. *Environmental Science & Technology,* 39**,** 1338-1345.

Lough, D. W., & Hathhorn, W.E. (1996) A computerized decision support system applied to NLAPL cleanup. In L.N. Reddi (Ed.), Non-aqueous phase liquids (NAPLs) in subsurface environment: Assessment and remediation. *New York, NY: American Society of Civil Engineers***,** 693.

Lowry, G. V. & K. M. Johnson (2004) Congener-specific dechlorination of dissolved PCBs by microscale and nanoscale zerovalent iron in a water/methanol solution. *Environmental Science & Technology,* 38**,** 5208-5216.

Masciangioli, T. & W. X. Zhang (2003) Environmental technologies at the nanoscale. *Environmental Science & Technology,* 37**,** 102A-108A.

Masel, R. I. 1996. *Principles of Adsorption and Reaction on Solid Surfaces*. John Wiley & Sons Inc.

Matheson, L. J. & P. G. Tratnyek (1994) REDUCTIVE DEHALOGENATION OF CHLORINATED METHANES BY IRON METAL. *Environmental Science & Technology,* 28**,** 2045-2053.

Morrison, I. D. & S. Ross. 2002. *Colloidal Dispersions: Suspensions, Emulsions and Foams*. New York: Wiley–Interscience.

Muftikian, R., Q. Fernando & N. Korte (1995) A METHOD FOR THE RAPID DECHLORINATION OF LOW-MOLECULAR-WEIGHT CHLORINATED HYDROCARBONS IN WATER. *Water Research,* 29**,** 2434-2439.

Ndjou'ou, A. C. & D. Cassidy (2006) Surfactant production accompanying the modified Fenton oxidation of hydrocarbons in soil. *Chemosphere,* 65**,** 1610-1615.

Northup, A. & D. Cassidy (2007) Evidence for the production of surfactants accompanying the chemical oxidation of hydrocarbons in soils. *Journal of Advanced Oxidation Technologies,* 10**,** 137-143.

Northup, A. & D. Cassidy (2008) Calcium peroxide (CaO2)for use in modified Fenton chemistry. *Journal of Hazardous Materials,* 152**,** 1164-1170.

151

Orth, W. S. & R. W. Gillham (1996) Dechlorination of trichloroethene in aqueous solution using Fe-O. *Environmental Science & Technology,* 30**,** 66-71.

Pan, B. J., H. Qiu, B. C. Pan, G. Z. Nie, L. L. Xiao, L. Lv, W. M. Zhang, Q. X. Zhang & S. R. Zheng (2010) Highly efficient removal of heavy metals by polymer-supported nanosized hydrated Fe(III) oxides: Behavior and XPS study. *Water Research,* 44**,** 815-824.

Parsons, S. 2004. *Advanced Oxidation Processes for Water and Wastewater Treatment*. UK: IWA Publishing.

Phenrat, T., N. Saleh, K. Sirk, H. J. Kim, R. D. Tilton & G. V. Lowry (2008) Stabilization of aqueous nanoscale zerovalent iron dispersions by anionic polyelectrolytes: adsorbed anionic polyelectrolyte layer properties and their effect on aggregation and sedimentation. *Journal of Nanoparticle Research,* 10**,** 795-814.

Phenrat, T., N. Saleh, K. Sirk, R. D. Tilton & G. V. Lowry (2007) Aggregation and sedimentation of aqueous nanoscale zerovalent iron dispersions. *Environmental Science & Technology,* 41**,** 284-290.

Phenrat, T., J. E. Song, C. M. Cisneros, D. P. Schoenfelder, R. D. Tilton & G. V. Lowry (2010) Estimating Attachment of Nano- and Submicrometer-particles Coated with Organic Macromolecules in Porous Media: Development of an Empirical Model. *Environmental Science & Technology,* 44**,** 4531-4538.

Ponder, S. M., J. G. Darab, J. Bucher, D. Caulder, I. Craig, L. Davis, N. Edelstein, W. Lukens, H. Nitsche, L. F. Rao, D. K. Shuh & T. E. Mallouk (2001) Surface chemistry and electrochemistry of supported zerovalent iron

nanoparticles in the remediation of aqueous metal contaminants. *Chemistry of Materials,* 13**,** 479-486.

Ponder, S. M., J. G. Darab & T. E. Mallouk (2000) Remediation of Cr(VI) and Pb(II) aqueous solutions using supported, nanoscale zero-valent iron. *Environmental Science & Technology,* 34**,** 2564-2569.

Puls, R. W., D. W. Blowes & R. W. Gillham (1999) Long-term performance monitoring for a permeable reactive barrier at the US Coast Guard Support Center, Elizabeth City, North Carolina. *Journal of Hazardous Materials,* 68**,** 109-124.

Quinn, J., C. Geiger, C. Clausen, K. Brooks, C. Coon, S. O'Hara, T. Krug, D. Major, W. S. Yoon, A. Gavaskar & T. Holdsworth (2005) Field demonstration of DNAPL dehalogenation using emulsified zero-valent iron. *Environmental Science & Technology,* 39**,** 1309-1318.

Raychoudhury, T., G. Naja & S. Ghoshal (2010) Assessment of transport of two polyelectrolyte-stabilized zero-valent iron nanoparticles in porous media. *J Contam Hydrol,* 118**,** 143-51.

Reible, D., & Demnerova, K. 2002. *Innovative approaches to the on-site assessment and remediation of contaminated sites, Boston, MA*. Kluwer Academic Publishers.

Reynolds, G. W., J. T. Hoff & R. W. Gillham (1990) Sampling Bias Caused by Materials Used to Monitor Halocarbons in Groundwater. *Environmental Science & Technology,* 24**,** 135-142.

Richmond, W. R., M. Loan, J. Morton & G. M. Parkinson (2004) Arsenic removal from aqueous solution via ferrihydrite crystallization control. *Environmental Science & Technology,* 38**,** 2368-2372.

Roberts, A. L., L. A. Totten, W. A. Arnold, D. R. Burris & T. J. Campbell (1996) Reductive elimination of chlorinated ethylenes by zero valent metals. *Environmental Science & Technology,* 30**,** 2654-2659.

Saba, T., T. H. Illangasekare & J. Ewing (2001) Investigation of surfactant-enhanced dissolution of entrapped nonaqueous phase liquid chemicals in a two-dimensional groundwater flow field. *Journal of Contaminant Hydrology,* 51**,** 63-82.

Saleh, N., H. J. Kim, T. Phenrat, K. Matyjaszewski, R. D. Tilton & G. V. Lowry (2008) Ionic strength and composition affect the mobility of surface-modified Fe-0 nanoparticles in water-saturated sand columns. *Environmental Science & Technology,* 42**,** 3349-3355.

Saleh, N., K. Sirk, Y. Q. Liu, T. Phenrat, B. Dufour, K. Matyjaszewski, R. D. Tilton & G. V. Lowry (2007) Surface modifications enhance nanoiron transport and NAPL targeting in saturated porous media. *Environmental Engineering Science,* 24**,** 45-57.

Scherer, M. M., J. C. Westall, M. ZiomekMoroz & P. G. Tratnyek (1997) Kinetics of carbon tetrachloride reduction at an oxide-free iron electrode. *Environmental Science & Technology,* 31**,** 2385-2391.

Schmidtke, T., D. White & C. Woolard (1999) Oxygen release kinetics from solid phase oxygen in Arctic Alaska. *Journal of Hazardous Materials,* 64**,** 157-165.

Schrick, B., J. L. Blough, A. D. Jones & T. E. Mallouk (2002) Hydrodechlorination of trichloroethylene to hydrocarbons using bimetallic nickel-iron nanoparticles. *Chemistry of Materials,* 14**,** 5140-5147.

Schrick, B., B. W. Hydutsky, J. L. Blough & T. E. Mallouk (2004) Delivery vehicles for zerovalent metal nanoparticles in soil and groundwater. *Chemistry of Materials,* 16**,** 2187-2193.

Snoeyink, V. L. & D. Jenkins. 1980. *Water Chemistry*. Wiley.

Song, H. & E. R. Carraway (2005) Reduction of chlorinated ethanes by nanosized zero-valent iron: kinetics, pathways, and effects of reaction conditions. *Environ Sci Technol,* 39**,** 6237-45.

Strongin, D. R., C. P. Grey, J. B. Parise & J. D. Kubicki (2010) Surface science studies of environmentally relevant iron (oxy)hydroxides ranging from the nano to the macro-regime. *Surface Science,* 604**,** 1065-1069.

Stumm, W. & J. J. Morgan. 1996. *Aquatic Chemistry: Chemical Equilibria and Rates in Natural Waters*. New York: John Wiley & Sons, Inc.

Su, C. M. & R. W. Puls (1999) Kinetics of trichloroethene reduction by zerovalent iron and tin: Pretreatment effect, apparent activation energy, and intermediate products. *Environmental Science & Technology,* 33**,** 163-168.

Su, C. M. & R. W. Puls (2004) Nitrate reduction by zerovalent iron: Effects of formate, oxalate, citrate, chloride, sulfate, borate, and phosphate. *Environmental Science & Technology,* 38**,** 2715-2720.

Sun, Y. P., X. Q. Li, J. S. Cao, W. X. Zhang & H. P. Wang (2006) Characterization of zero-valent iron nanoparticles. *Advances in Colloid and Interface Science,* 120**,** 47-56.

Sun, Y. P., X. Q. Li, W. X. Zhang & H. P. Wang (2007) A method for the preparation of stable dispersion of zero-valent iron nanoparticles. *Colloids and Surfaces a-Physicochemical and Engineering Aspects,* 308**,** 60-66.

Sun, Y. P. & W. X. Zhang. 2005. Dispersion of zero-valent iron nanoparticles. 090-IEC.

Tee, Y. H., L. Bachas & D. Bhattacharyya (2009) Degradation of Trichloroethylene by Iron-Based Bimetallic Nanoparticles (vol 113, pg 9454, 2009). *Journal of Physical Chemistry C,* 113**,** 12616-12616.

Tee, Y. H., E. Grulke & D. Bhattacharyya (2005) Role of Ni/Fe nanoparticle composition on the degradation of trichloroethylene from water. *Industrial & Engineering Chemistry Research,* 44**,** 7062-7070.

Tiraferri, A., K. L. Chen, R. Sethi & M. Elimelech (2008) Reduced aggregation and sedimentation of zero-valent iron nanoparticles in the presence of guar gum. *Journal of Colloid and Interface Science,* 324**,** 71-79.

Tsai, T. T., C. M. Kao, T. Y. Yeh, S. H. Liang & H. Y. Chien (2009) Remediation of Fuel Oil-Contaminated Soils by a Three-Stage Treatment System. *Environmental Engineering Science,* 26**,** 651-659.

Tufenkji, N. & M. Elimelech (2004) Correlation equation for predicting single-collector efficiency in physicochemical filtration in saturated porous media. *Environmental Science & Technology,* 38**,** 529-536.

Udell, K. S., Grubb, D.G., & Sitar, N (1995) Technologies for in situ cleanup of contaminated sites. *Central European Journal of Public Health,* 3**,** 67-76.

Vogel, T. M., C. S. Criddle & P. L. McCarty (1987) TRANSFORMATIONS OF HALOGENATED ALIPHATIC-COMPOUNDS. *Environmental Science & Technology,* 21**,** 722-736.

Walling, C. (1975) Fenton's reagent revisited. *Acc. Chem. Res.,* 8**,** 125-131.

Wang, C. B. & W. X. Zhang (1997) Synthesizing nanoscale iron particles for rapid and complete dechlorination of TCE and PCBs. *Environmental Science & Technology,* 31**,** 2154-2156.

Watts, R. J., M. K. Foget, S. H. Kong & A. L. Teel (1999) Hydrogen peroxide decomposition in model subsurface systems. *Journal of Hazardous Materials,* 69**,** 229-243.

Watts, R. J. & P. C. Stanton (1999) Mineralization of sorbed and NAPL-phase hexadecane by catalyzed hydrogen peroxide. *Water Research,* 33**,** 1405-1414.

Watts, R. J. & A. L. Teel (2005) Chemistry of modified Fenton's reagent (catalyzed H2O2 propagations-CHP) for in situ soil and groundwater remediation. *Journal of Environmental Engineering-Asce,* 131**,** 612-622.

Wei, Y. T., S. C. Wu, C. M. Chou, C. H. Che, S. M. Tsai & H. L. Lien (2010) Influence of nanoscale zero-valent iron on geochemical properties of groundwater and vinyl chloride degradation: A field case study. *Water Research,* 44**,** 131-140.

Wilkin, R. T., R. W. Puls & G. W. Sewell (2003) Long-term performance of permeable reactive barriers using zero-valent iron: Geochemical and microbiological effects. *Ground Water,* 41**,** 493-503.

Wool, R. P. & X. S. Sun. 2005. Chapter 9: Thermal and Mechanical Properties of Soy Proteins in Bio-Based Polymers and Composites. 292-293. Academic Press.

Wu, N. Q., L. Fu, M. Su, M. Aslam, K. C. Wong & V. P. Dravid (2004) Interaction of fatty acid monolayers with cobalt nanoparticles. *Nano Letters,* 4**,** 383-386.

Xiong, Z., D. Zhao & G. Pan (2007) Rapid and complete destruction of perchlorate in water and ion-exchange brine using stabilized zero-valent iron nanoparticles. *Water Res,* 41**,** 3497-505.

Xu, P., G. Achari, M. Mahmound & R. C. Joshi (2006) Application of Fenton's Reagent to Remediate Diesel Contaminated Soils. *Practice Periodical of Hazardous, Toxic, and Radioactive Waste Management,* 10**,** 19-27.

Yang, G. C. C., H. C. Tu & C. H. Hung (2007) Stability of nanoiron slurries and their transport in the subsurface environment. *Separation and Purification Technology,* 58**,** 166-172.

Zhang, W. X. (2003) Nanoscale iron particles for environmental remediation: An overview. *Journal of Nanoparticle Research,* 5**,** 323-332.

Zhang, W. X., C. B. Wang & H. L. Lien (1998) Treatment of chlorinated organic contaminants with nanoscale bimetallic particles. *Catalysis Today,* 40**,** 387-395.

VITA

Pijit Jiemvarangkul was born in 1977 in Bangkok, Thailand. He received his B.Eng. (1998) and also M.Eng. (2001) in Environmental Engineering from King Mongkut's University of Technology Thonburi (KMUTT) in Bangkok, Thailand. He has been serving as a full time lecturer at Department of Civil Engineering, King Mongkut's University of Technology-North Bangkok (KMUTNB) in Thailand. At KMUTNB, Pijit was responsible for teaching engineering undergraduate courses such as Introduction to Environmental Engineering, Water Supply and Wastewater Treatment, and Engineering Statics (Engineering Mechanics I). In 2004, Pijit was awarded a scholarship by the Royal Thai government to further his advanced studies at Lehigh University. In Fall 2005, Pijit was enrolled into Lehigh University and worked with Dr. Wei-xian Zhang for his master studies. Nanoscale zero-valent iron (nZVI) technology, proposed by Dr. Zhang in 1996, has been a rapidly growing environmental nanotechnology. Pijit's thesis focused on dispersion and transport of nZVI particles. He received his Masters of Science in Environmental Engineering from Lehigh University in 2007.

In Fall 2007, Pijit continued his doctoral study in Environmental engineering with Dr. Wei-xian Zhang's group at Lehigh University. His doctoral work expanded his research on dispersion and transport of nZVI particles, NAPLs removal by nano-particles including nZVI and a new type nano-scale calcium peroxide particles. One of Pijit's works on transport of nZVI particles has been published by Chemical Engineering Journal, volume 170, issue 2 – 3, page 482 – 491, in June 2011.

159